Integrated Modelling and Testing of Engineering Structures: A validation Approach for Multi-physics Simulations

Shirley Nwakaego Eseigbe

Thesis submitted for the Degree of Philosophy

June 2022

School of Engineering

The Quadrangle, The University of Liverpool, Brownlow Hill, Liverpool L69 3GH

Abstract

The aim of this project was to develop an extended approach for the validation of multi-physics models, using quantitative full-field data obtained from a carefully designed validation experiment. This work was performed to meet one of the technological gaps identified for an Integrated Nuclear Digital Environment (INDE), which was the need to develop a multi-scale and multi-physics validation method.

An enhanced multi-physics process flowchart containing three different physics domains, thermal, mechanical, and thermomechanical domains, has been successfully developed, which details the approach for validation of multi-physics models using quantitative experimental data. The new enhanced process flowchart was built from the flowcharts in the ASME and CEN V&V guides, with a focus on the design of validation experiments. As part of this research's objectives, the processes in the new flowchart were successfully tested using an industrial case study and carefully designed experiments that captured each physics component.

Three experiments, thermal expansion, three-point bending, and combined thermal expansion and three-point bending experiments, were successfully designed and tested to explore the processes of the enhanced validation flowchart. The comparison between the results obtained from the simulations and the measurements indicated a good level of agreement. A high degree of linearity was observed for the load versus displacement relationships for the physical experiments and the simulations. The superposition principle was employed to mathematically combine the data from the single physics domains to account for the overall effect of the multi-physics domains. The results obtained from the superposition of different physics data were in good agreement with those obtained from the multi-physics data, indicating that the multi-physics experiment successfully captured the boundary conditions of the individual physics domain. In this research, a system calibration experiment was performed for each experimental setup (thermal, mechanical, and combined thermal-mechanical experiments) to determine the uncertainty associated with each physical measurement. The results determined from the calibration experiment was used to determine the allowable or acceptable scatter in the comparison plots.

Acknowledgements

I am immensely grateful to God for the strength granted to me during the course of my PhD journey and to my family for their love and support.

This journey would not have been possible without the support of my family and supervisors. I am grateful to Professor Eann Patterson, most especially for providing the leadership, motivation, and support needed during my research whilst also allowing me to take full ownership of my project.

My deepest thanks to Professor Richard Taylor (my secondary academic supervisor) for your constructive advice and questions during this journey and to Dr Mark Bankhead for your industrial support.

I would also like to express my sincere gratitude to the University of Liverpool, the School of Engineering Technician Team, Jiji Matthew, Derek Neary, and Daniel Pott. Your support in manufacturing my novel thermomechanical rig (The SEN rig) is extremely appreciated.

Finally, thanks to my mama, Zanelle, my brothers, Precious, and Lucky for all your support and encouragement in the Word.

Date:

28/06/2022 Shirley Eseigbe

Contents

Abstract 2

Acknowledgements 3

Contents 4

Chapter 1 7

Introduction 7

1.1. Research Background 7

1.2. Validation of Solid Mechanics Models 9

1.3. Research Motivation 11

1.4. Aim and Objectives of Research 12

Chapter 2 13

2. Literature Review 13

2.1. Validation of Multiphysics Computational Models 13

2.1.1. The Validation Process of Computational Solid Mechanics Models 15

2.2. Validation Experiments 23

2.2.1. Quality Experimental Data and Documentation 24

2.2.2. Quantitative (Robust) Experimental Data 24

2.2.3. Image Decomposition Method 25

2.3. Uncertainty Quantification 27

2.3.1. Aleatory and Epistemic Uncertainties 28

2.3.2. Uncertainty Quantification of Multiphysics systems 29

2.3.3. Measurement Uncertainty 31

2.4. Validation Metrics 34

2.5. Conclusions 36

2.6. Knowledge Gaps 37

Chapter 3 38

3. Proposed Enhanced Validation Process Flowchart 38

3.1. Methodology of the Enhanced Processes in the New Flowchart 40

3.2. Conclusions 44

Chapter 4 45

4. Physical and Computational Research Methods 45

4.1. Case Study 46

4.2. Digital Image Correlation Measurement Method 48

4.3. Full-field Infrared Thermography 54

4.4. Thermal Component: Experimental Design and Procedures ... 55
4.4.1. Introduction ... 55
4.4.2. Thermal Expansion Experimental Design and Instrumentations ... 57
4.4.3. Heating Element (Quartz lamp) ... 58
4.4.4. Experimental Procedure ... 59
4.5. Mechanical Component: Experimental and Procedure ... 61
4.5.1. Introduction ... 61
4.5.2. Mechanical Design and Instrumentations ... 63
4.5.3. Experimental Procedure ... 73
4.6. The Combined Thermal and Mechanical Components: Experimental Design and Procedure 76
4.6.1. Introduction ... 76
4.6.2. Thermo-mechanical Experimental Design and Instrumentations ... 77
4.6.3. Thermo-mechanical Experimental Procedure ... 80
4.7. Numerical Study: Development of the Finite Element Models ... 81
4.7.1. Introduction ... 81
4.7.2. Development Process of the Finite Element Models ... 82
4.7.3. Thermal Component: Thermally-Induced Deformation of a 316L Stainless Steel Tube 83
4.7.4. Mechanical Component: Three-Point Bending of a Simply Supported 316L Stainless Steel Tube ... 88
4.7.5. Thermo-mechanical Component: Coupled Thermal and Mechanical Deformation of a Stainless-Steel Tube ... 91
4.8. Conclusions ... 92
Chapter 5 ... 93
5. Assessment of Measurement Uncertainty ... 93
5.1. Introduction ... 93
5.2. Reference Material Design and Analytical Description ... 95
5.3. Calibration Experimental Procedure ... 96
5.4. Calibration Results ... 97
5.5. Conclusions ... 99
Chapter 6 ... 100
6. Results and Discussion of the Measurements and Numerical Simulations ... 100
6.1. Introduction ... 100
6.2. Orthogonal Image Decomposition of Full-field Displacement Results ... 101
6.3. Load-deformation relationship of the thermal component ... 105
6.4. Load-deformation relationship of the mechanical component ... 112

6.5. Load-deformation relationship of the thermo-mechanical component 116
6.6. Conclusions 120
Chapter 7 121
7. Quantitative Comparison and Validation of the Simulation Results with the Corresponding Measurement Data 121
7.1. Introduction 121
7.2. Sources of errors and uncertainties in the measurement data 122
7.3. Quantitative comparison of the simulation and measurement results 129
7.3.1. Comparison of the thermal component 130
7.3.2. Comparison of the mechanical component 134
7.3.3. Comparison of the thermo-mechanical component 137
7.4. Impact on current state-of-the-art validation guidelines 146
7.5. Conclusions 147
Chapter 8 148
8. Conclusions 148
8.1. Further work 150
References 151
Appendix A 161

Chapter 1

Introduction

1.1. Research Background

This research was designed and tested to address a technological gap identified by Patterson et al. [1]. They proposed a conceptual framework for an Integrated Nuclear Digital Environment (INDE[1]). INDE addresses all stages of a typical nuclear project lifecycle, i.e. it extends from a prototype design of a nuclear power plant through operations and decommissioning to storage and waste disposal, as illustrated by the schematic diagram in figure 1.

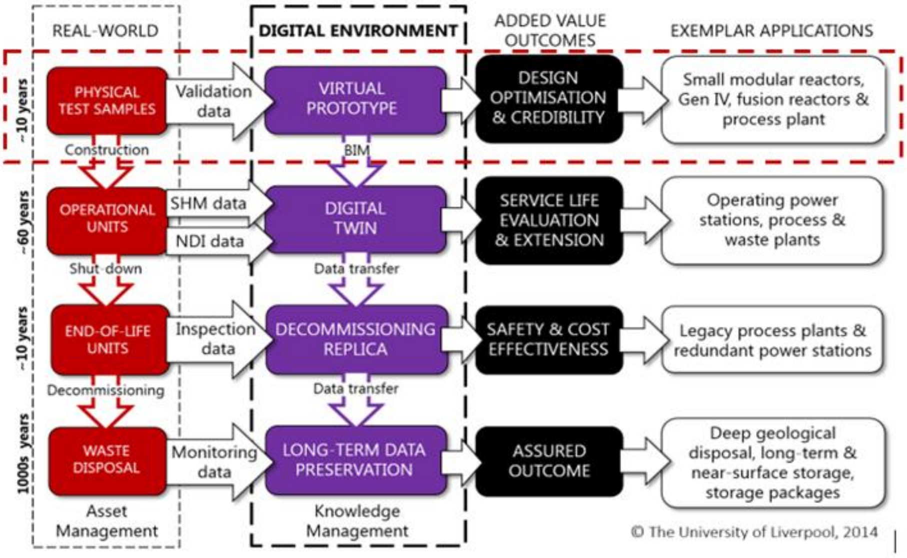

Figure 1: Schematic diagram of the Integrated Nuclear Digital Environment [1]

In this paper, the authors identify that INDE will consist of multi-scale and multi-physics computational models linked to the real-world (physical system) through data acquired during prototype tests (design phase); in-service monitoring and inspection of plants (operational phase); post-shutdown of plants (decommissioning phase); and in-situ monitoring of stored waste (waste storage/management phase) [1].

The implementation of INDE will result in an integrated nuclear digital database with descriptions of the system and components from the design stage to the present state. This environment will promote the digital perseverance and effective management of nuclear energy data to help make informed

[1] Integrated Nuclear Digital Environment (INDE)

decisions regarding the management and control of nuclear energy systems. It is also expected that the implementation of INDE will benefit the nuclear industry by reducing the development time and cost of innovative designs and increase credibility, operability, reliability, and safety. The latter is of much significance to the nuclear industry and how the public perceives nuclear power as a source of green energy.

For INDE to be successfully executed, the following identified technology gaps need to be implemented. They include;

- High-performance computing for data management and model integration
- Nuclear application of Building Information Management (BIM)
- Implementation of in-situ structural health monitoring of nuclear energy systems
- Quantitative procedure for model verification and validation

The primary aim of this research is to address the need for a quantitative procedure for model verification and validation, and it lies in the design phase of the schematic diagram in figure 1, represented by the red dotted box. The work reported in this thesis only addresses the need for a quantitative validation approach, and the verification component is out of scope

The following section introduces the concept of computational validation of solid mechanics models within the science and engineering community.

1.2. Validation of Solid Mechanics Models

Mathematical or numerical model validation is increasing in importance as accurate models of real-life physical systems are desirable to test, improve and optimise the design and management of science and engineering assets. In engineering, these models can be classified as predictive or informative [2]. The growing application of computational models is motivated by the need to replace complex, sophisticated experimentations, which are expensive or performed in a laboratory, with accurate model predictions.

The availability of supercomputers has made it possible to simulate sophisticated processes that involve higher levels of complexity which are inherently multi-scale and multi-physics in nature. Nuclear energy components, such as fuel claddings, are typical examples of components that undergo deformation due to multi-physics phenomena, which include a combination of radiation, temperature, and pressure.

The increasing application of computational models generates the need to assess such models' reliability and credibility if they are to be used for making informed decisions that involve socio-economic and human significance. Establishing the credibility of a computational model is essential, and it is usually the responsibility of a decision-maker who may not have the technical expertise. Patterson [2] and Schruben [3] suggested that credibility can be viewed as the willingness of a decision-maker to base their decisions on the body of evidence supporting a model's reliability. Therefore, it is crucial to provide sufficient quality information and data to support a model's fitness for use for its intended applications.

The body of evidence required for effective decision-making about a model's reliability may include the quality and quantity of the data derived from the physical system. It is usual for modellers to assess their models against experimental data wherever possible. These comparisons can be qualitative or quantitative. A qualitative comparison may include contour plots, x-y or scatter plots of the predictions and measurements, often with no detail on the sources of uncertainties in the data. The questions that arise after plotting the results include: how accurate is the agreement between the measurements and the predictions? What is the allowable scatter in the comparison plot? How is the level of agreement quantified? The process of answering these questions is known as validation.

The term validation is defined as the "process of determining the degree to which a mathematical computer model is an accurate (or reliable) representation of the real world from the perspective of the intended applications." [4],[5], [6]. The history of this definition can be traced back to work by Fishman and Kiviat [7] and Van Horn [8] in economic science. Van Horn noted that a model is commonly developed with specific objectives to reflect the intended uses of the model, and therefore, it is expected that the prediction from the model should be assessed against a pre-defined set of objectives. Sargent [9] also specifically included the term“intended uses of the model" in the definition to consider the model's reliability based on its intended application. Van Hon [8], in the field of economics, describes validation as the act of increasing to an "acceptable level of confidence" that an inference about a simulation process is an accurate representation of the physical system, implying that validation is an ongoing exercise that occurs throughout the service life of a system. Notice the keyword here is "**confidence**." The acceptable level of confidence that is determined from a validation assessment is related to the model's intended use and the quantified associated uncertainties. The appropriateness is dictated by the consequences of the simulation being inaccurate when applied in the real world. A validation assessment can be performed using historical data or data generated from new experiments. It is, however, usually a good practice to use the latter, as suggested in [4 -7], to achieve a robust comparison.

The AIAA[2] [4] and ASME[3] [5] have both developed similar guides detailing the processes to be followed to perform validation assessments. However, little information is provided on the design of such experiments or the method for comparing data from a model and experiment. The work performed in the ADVISE [10] and VANESSA [11] projects extended the processes of the ASME Validation and Verification (V&V) flowchart to provide a validation methodology detailed in the CEN[4] guide [12]. The methodology makes use of full-field images or data obtained with optical measurement techniques. The processes described in the CEN guide recommend the use of image decomposition to reduce the fields of data to feature vectors that facilitate straightforward comparison using statistical methods.

This thesis extends the work done by the ASME and the CEN guides to develop a quantitative validation approach for multi-physics problems with an emphasis on designing validation experiments for multi-physics problems.

[2] American Institute of Aeronautics and Astronautics
[3] The American Society of Mechanical Engineering
[4] European Committee of Standardisation (CEN). Validation of computational solid mechanics models, CEN Workshop Agreement, CWA 16799:2014 E.

1.3. Research Motivation

The primary motivation of this research is to address a technology gap identified in the background section of this thesis, which is to develop a quantitative validation procedure for multi-scale and multi-physics models.

Current validation approaches and methodologies of computational models often deal with single-physics domains. However, most engineering systems such as aerospace, fission and fusion energy systems are complex and involve multiple physics domains. A fuel cladding from a nuclear energy plant is an example of such a component that operates in a multi-physics environment. The fuel cladding of a nuclear energy system is one of the most critical safety barriers in fission reactors. It retains most of the radioactive fission products within its volume and must maintain its structural integrity for safe operations. The development of a fuel cladding computational model involves the interaction of different physics domains, such as heat transfer, fluid dynamics, radiation physics, thermal and mechanical stresses and strains.

The validation of such models requires consideration of the different physics co-occurring during its service life, implying a need to extend the current validation approach or guides in the literature to assess the reliability and accuracy of multi-physics models. The need for a validation approach that accounts for a multi-physics phenomenon is the primary motivation for this research.

At this juncture, it is worth noting that this research addresses multi-physics models only and does not include multi-scale models. However, the validation procedure may be adapted to validate multi-scale models.

1.4. Aim and Objectives of Research

The aim of this project is to develop an extended validation approach for multi-physics simulations through careful design of experiments and uncertainty quantification that builds on the processes in the ASME V&V guide [5] and the CEN guide [12]. The objectives of this project are:

- Develop an extended validation process
- Design validation tests for the different physics domains using a suitable case study to explore the processes of the extended validation approach
- Develop a procedure to merge the uncertainties from the different physics domains to allow a robust and quantitative comparison between the prediction and measurement results.

The layout of this thesis begins with a literature review of current state-of-the-art validation approaches, which include uncertainty quantification and validation metrics in chapter 2. Chapter 3 details the proposed enhanced validation processes and methodology, while chapter 4 describes the experimental and computational research methods. The following chapter, chapter 5, describes the process followed to determine the measurement uncertainty, including the results obtained. Chapter 6 details the results obtained from the experiments and computational models and discusses the result analyses. The final chapter, 8, lists the research's conclusions and recommendations for further work.

Chapter 2

2. Literature Review

This chapter reviews the literature related to the validation of computational models, which includes the current validation process, design of validation experiments, the quantification of uncertainties associated with the simulation and the measurement data and metrics used to assess the accuracy of models. The chapter is split into five main sections, with the first section introducing the validation process for solid mechanics models. The second section focuses on the design of validation experiments, and the third section investigates the methods for quantifying uncertainties in both predictions and measurements. The fourth section concentrates on the application of statistical metrics as part of a validation assessment. The fifth section introduces the concept and philosophical view of multi-physics validation. The final section concludes the literature review and identifies the knowledge gaps.

2.1. Validation of Multiphysics Computational Models

Computational models and simulations of nuclear energy components for design and system optimisation require the combined modelling of several different interrelated physical processes, including fuel behaviour, neutronics, thermal-hydraulics, thermal physics, and structural mechanics. It is essential to define what is meant by **multi-physics** in the context of this thesis before proceeding further. The term **multi-physics** modelling implies coupling between different numerical models or codes with **different governing equations** and **data exchange between the different models**. Fundamentally, it means that there are two or more physical models with distinctive equations: for example, one could be a thermal model that calculates the thermal stresses and thermal expansion, and the other could be a structural model that calculates displacements, stresses, and strains. The modelling effort would involve interactions and data exchange between the models. In this example, the structural model calculates the displacement and sends this information to the thermal model, which calculates the thermal forces and returns the information to the structural model.

Over the past years, verification and validation of single physics models or phenomenon have been the subject of extensive research, such as the recently developed reactor code, MPACT [13]. Recently there have been modelling efforts to develop codes that couple different physics components of a nuclear reactor, which strongly considers the interaction and feedback between different physics domains, behaviour, and processes. The Simulation Consortium for Advanced Simulation of LWRs (CASL) in the USA [14], and the Simulation-based High-efficiency Advanced Reactor Prototyping (SHARP) toolkit, developed in the U.S Department of Energy Nuclear Energy Advanced Modeling and

Simulation (NEAMES) [15], are some examples of multi-physics modelling efforts. These efforts highlighted above deal more with code verification and not model validation. Verification is defined as *the process of determining that a computational model accurately represents the underlying mathematical model and its solution* [5].

For a newly developed computational model of nuclear reactor components to be used commercially, it must first be assessed against the corresponding real-life component using historical data from ***benchmark experiments, new validation experimental data, or other statistical means***. The process of assessing the reliability of a computational model against its physical counterpart is known as ***validation***. By definition, validation is the process of determining the degree to which a model accurately represents reality for the purpose of the intended uses of such a model [5].

Database of Benchmark Experiments has been developed and made publicly available to the nuclear energy community to provide data for code verification and potential validation assessment of multi-physics models. The benchmark experiments are compiled in the Handbook of Evaluated Criticality Safety Reactor Physics Benchmark Experiments, available on the Nuclear Energy Agency webpage (Nuclear Energy Agency (oecd-nea.org)). The majority of the data in this database are more suitable for application to a single physics phenomenon. These data may be described as "separate-effects tests", i.e., representing a specific phenomenon or physical behaviour of a reactor. It is desirable to have data from a carefully designed experiment to validate multi-physics models, and some research has been done on this need [16],[17]. However, it is impracticable to design a prototype of a full-scale nuclear reactor to provide validation data. Therefore, most of the research towards designing multi-physics experiments have been limited to specific physics phenomena or domains of a reactor system. *The questions that arise from this challenge are, how do we validate such models involving multiple physics phenomena with experimental data from separate effect tests, and at the same time build confidence in the process followed to perform the validation assessment*? Attempting to answer this question requires understanding the state-of-the-art approaches or processes of model validation.

2.1.1. The Validation Process of Computational Solid Mechanics Models

A validation process can be described as the modelling and simulation activities, parallel with the experimental activities and the assessment activities involved in a model verification and validation (V&V). The V&V process in figures 2 and 3 can be employed as a baseline to demonstrate confidence that the results obtained from a computational model are sufficiently accurate to solve the intended problem.

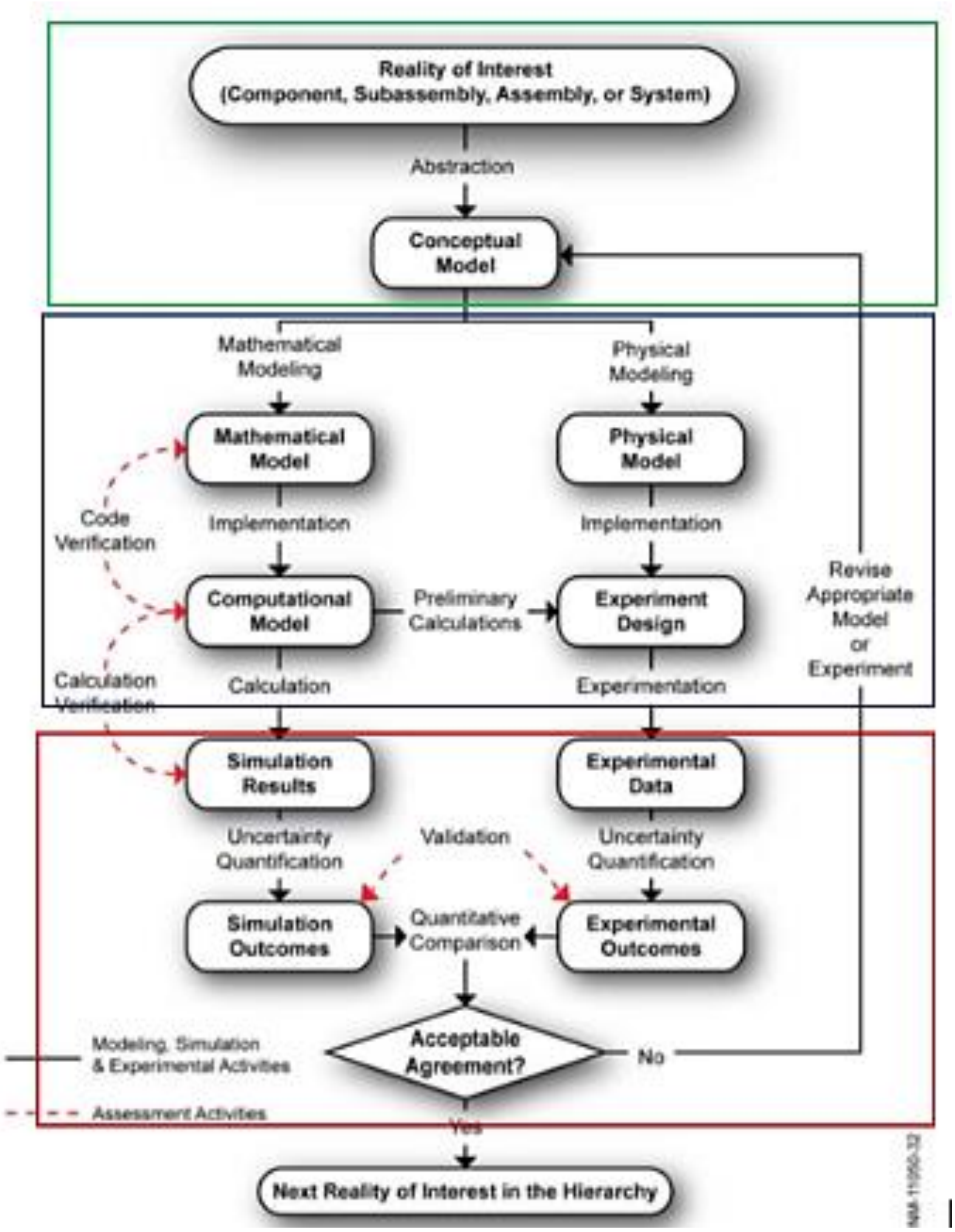

Figure 2: ASME V&V flowchart and processes [5]

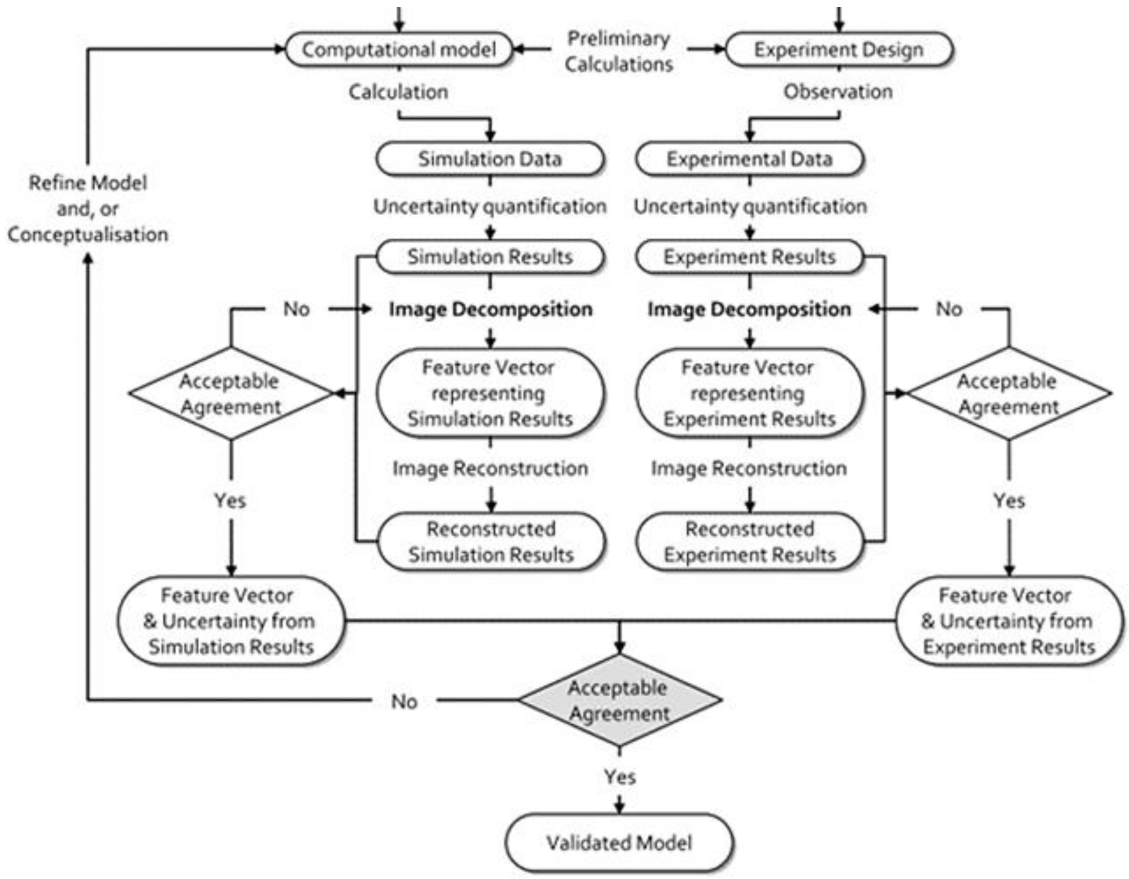

Figure 3: Flowchart from the CEN guide based on full-field data and image decomposition [5]

The AIAA [4] and ASME [5] have both developed similar flowcharts containing processes to be followed for the validation of computational models. The CEN [12] has also recently developed a more detailed process for the validation of models using full-field images or data obtained using optical measurement techniques. The process described in the CEN guide recommends the use of image decomposition to reduce the fields of matrices of predictions and measurements to feature vectors that aid straightforward comparison using statistical methods. The ASME guide, which has recently been revised into a standard, provides principles and broad definitions, while the CEN guide describes a practical approach to achieve a quantitative comparison between data of predictions and measurements using full-field data.

Several authors, such as Sargent [9]; Balci [18]; Marvin [19]; Roache [20]; Trucano et al. [21]; and Oberkampf [22], have also proposed strategies to model validation. Their concept of model validation involves quantitative comparisons of model predictions with measurements from physical tests for the purpose of accuracy assessment of a physics-based model, which Roy and Oberkampf [23] referred to as **scientific validation**. The concept of these strategies is incorporated in the ASME and AIAA guides [4], [5]. *A validation assessment aims to establish a high level of **confidence** in the computational* *simulation used in the design process of engineering systems and inform decisions of socio-economic and safety significance.* The keyword here is "***confidence.***" What level of confidence is acceptable to conclude that the outcome derived from a computational simulation of a physical process is ***credible****?* Schruben [3] described ***credibility as "the willingness of persons to base decisions on information obtained from the model"***. Therefore, the issue becomes a matter of providing sufficient evidence of the model's fitness for purpose to stimulate the willingness of the decision-makers. Balci [18], [24] has also recommended a detailed step-by-step validation approach to build a level of confidence depending on the uses of the model. The approaches from the literature and validation guides mentioned previously assume the availability of data from a carefully planned experiment to validate the corresponding simulation. Patterson and Whelan [25] referred to such models as "**testable and principled models**", as depicted in figure 4, because the knowledge of the physics behaviour is known and can be tested to provide observational data for validation. The approaches stipulated in the validation guides are typically appropriate for this type of simulation because measurement data from the physical system is available to establish the simulation's accuracy and build confidence in its use. However, this is not the case for "**untestable**" [25] models where there is no observational data to demonstrate the predictive capability and accuracy of the simulation, which may be due to the cost and complexity involved in designing a prototype of the physical system, and the challenges of adequately capturing all the physical phenomena occurring in the system, e.g., multi-physics engineering systems used in the aerospace and nuclear energy industries. This reinforces the importance of coupled physical tests that addresses different physics phenomena and also, an approach to merge validation outcome from separate physics domains.

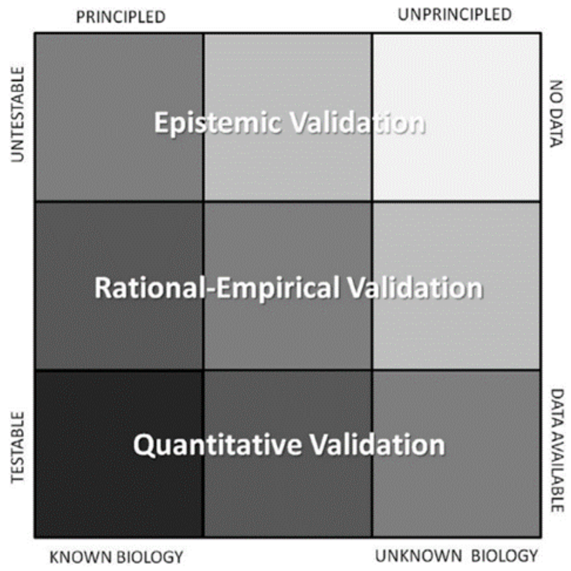

Figure 4: 3x3 schematic diagram illustrating the relationship between testable and untestable models that are either based on known biology (i.e. principled) or unknown biology (i.e. unprincipled) together with approaches to performing validation and the required level of credibility indicated by the greyscale [25]

Recently, Patterson and Whelan [26] proposed a new matrix that is a blend of the previous matrix diagram in [2],[25] and the work by Kleindorfer et al. [27] to demonstrate the probable relevance of the several validation approaches described by their corresponding position in the philosophy of science. A detailed description of each position identified in the schematic diagram in Figure 6 can be found in [25]–[27].

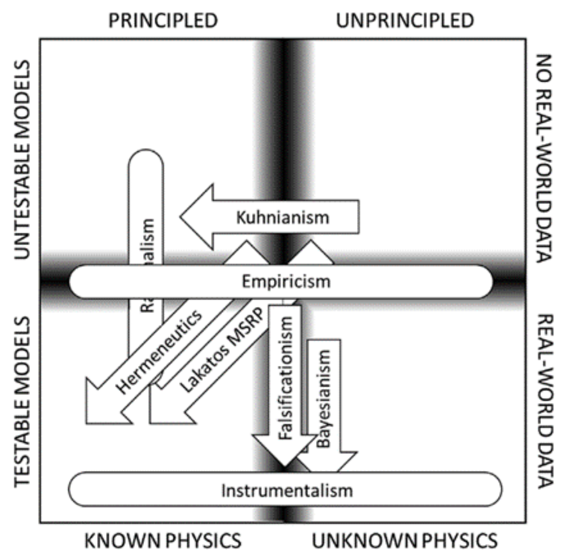

Figure 5: Schematic diagram illustrating the epistemological divisions between principled models based on known physics and unprincipled models based on unknown physics, as well as the testable and untestable models with fuzzy boundaries forming the 2 x 2 matrix; along with the various

positions in the philosophy of science from Kleindorfer et al. showing their potential applicability as strategies to model validation [26]

Table 1: Various validation positions in the philosophy of science with the representative philosophers [27]

Positions in the Philosophy of Science	General Epistemological Focus	Criterion of the Philosophy	Representative Philosophers	Validation Approaches
Rationalism	Logical justification of knowledge claims	Logical reduction	Descartes	Derived from rational foundation
Classical Empiricism		Inductive generalization	J. S. Mill J. N. Keynes	Induced from empirical data
Logical Positivism		Empirical verification	Carnap, Russell Wittgenstein	Derived from empirical foundation
Instrumentalism	Theories as frameworks for prediction and testing	Predictive success, simplicity, or other aesthetic value	Pierce Friedman	Shown by predictive accuracy, simplicity, or other value
Dogmatic Falsificationism		"theory-free" observations to test theories	Popper	Continued testing to eliminate faulty models
Methodological Falsificationism		Survival of testing and criticism	Lakatos' version of Popper	Shown by testing and criticism
Bayesianism	Consistent treatment of probabilistic induction	Increase subjective probability	Howson Urbach	Empirical success increasing belief
Kuhnianism	Progressive historical growth of knowledge	Growth of knowledge through Paradigm shifts	Kuhn, Polyani Bohm Weimer	Accordance with expert opinion, professional acceptance
Lakatos' MSRP		Growth of knowledge through Research Programmes	Popper, Lakatos Bartley, Agassi	Increase empirical and theoretical content without ad hoc adjustment
Hermeneutics	Interpretation and understanding through dialog and practice	Knowledge growth by application with participation	Bernstein Gadamer	Participation by all interested in the outcome

The horizontal axis of the schematic diagram in figure 5 relates to the knowledge base underpinning the model. The models on the left of the diagram are developed from well-understood physics principles, while the models on the right are unprincipled because the physics is unknown. These types of models are commonly developed based on statistical correlations [26]. *The notion of testable and untestable models as related to multi-physics and complex systems may become challenging when it comes to building confidence and credibility that a computational simulation is fit for its purpose. This is because credibility depends on the body of evidence [28] and is usually based on the availability of quantitative measurement data to support a model's fitness for use*.

In general, the current state-of-the-art validation process starts with identifying the reality of interest, a physical representation of the system or problem for which data is being obtained. The problem can be a unit problem (single physics), component problem, sub-assembly or a complete system. Once the reality of interest has been identified, a conceptual model is developed, which involves the specification of the physical system and its operating environment. The conceptual model includes the collections of assumptions, physical relationships, and the response quantity of interest to be measured. The problem statement is defined from the perspective of the intended use, which is then used to develop both the mathematical model and to design the physical system. The implementation of the mathematical model results in the computational model. Similarly, the implementation of the physical model results in the experimental design.

Computational solid mechanics models are more commonly based on finite element methods [29], with some application of boundary element methods [30]. It is usual for the suppliers of these software packages to perform verification of the modelling methods as part of the software package's certification. Therefore, the verification part of the V&V flowchart in figure 2, shown in the blue box, will not be addressed in the scope of this research project. The final part of the validation activity or assessment in figure 2, shown in the red box, aims to assess and quantify the model's accuracy by comparing the experimental data with the simulation outcome.

A validation assessment is performed to decide whether the model has resulted in an acceptable agreement with the experiment based on the intended use of the model. The level of agreement or disagreement can be measured by quantifying the difference (error) between the model output and the experimental output [4], [5], [8], [9], and can be expressed as a statistical statement. For example, the statement can include the expected error with associated confidence limits. The Office of Nuclear Regulation (ONR) stressed that validation statements should ideally quote and substantiate the confidence level for its calculations [31]. Balci [18] and Oberkampf [32] recommended that a validation assessment include the interpolation or extrapolation of the computational model for the conditions corresponding to the intended use in the absence of experimental data.

The validation process of figures 2 and 3 applies to a unit or single physics problem. For a complete system problem, which may involve multiple physics domains, the processes in the flowchart will need to be extended to account for the additional physics domains. The hierarchical approach to model validation, also known as the building-block approach, has been recommended in the AIAA V&V guide [4] and has also been developed by some authors, including Marvin [19], Lin et al. [33], and Cosner [34], to deal with the issue of how to validate complex fluid dynamics systems involving multiple physics domains. They developed a building-block strategy illustrated in figure 6 that decomposes a complete engineering system into an arbitrary number of progressively smaller units [35], supported by Thacker's [36] detailed tutorial on hierarchical validation for complex systems that utilise building-block principles. In the field of reactor safety and fault analysis, a similar concept of validation hierarchy is referenced as "***separate effect testing***". The tiered approach aims to assess how accurate a computational response compares with an experimental response at lower tiers of system complexity or at different levels of physics couplings [31]. ***The advantage of a validation hierarchy approach is that it helps identify a range of lower-level tiers where quality experiments can be designed and tested to support accuracy assessments of complex computational models of simpler systems and physics.***

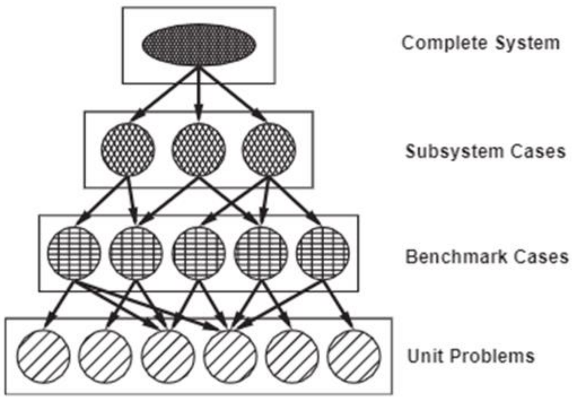

Figure 6: Hierarchical validation approach for complex systems [35]

The philosophy of the tiered approach is relevant and limited to linear systems where the disassembly of the multi-physics system into fewer physics complexity is possible and for which well-characterised experiments can be designed and tested to generate quality and quantitative validation data. This method is not efficient for systems with non-linearity behaviour and with evidence of emergent behaviour: properties that emerge from fundamental interactions which could not have been expected from the relevant fundamental principles of each physics component [2]. In other words, emergence behaviour can arise from the interaction between more than one component in a system or from interacting physics domains. The observation of emergent behaviours does not mean that a model is less useful. DeLanda [37] discussed the significance of emergent properties and how it allows simulations to decompose reality and reproduce phenomena at one scale without the need for high-fidelity representation at all scales. This process is relevant to hierarchical modelling [2] and the hierarchical approach to validation [36]. Johnson [38] highlighted that the analysis of individual, interacting components within a complex system could not fully define the behavioural properties of the system. Other authors [39], [40] have reviewed this topic of emergence behaviour in an attempt to develop approaches to analyse and validate its effect in complex modelling and simulations. The issue of emergent behaviour can significantly impact a validation assessment and its outcome, especially when using measurement data acquired from separate effect tests that were designed following the hierarchical approach to validate coupled simulations. It is, therefore, reasonable to assume that the acceptance criteria for a model's reliability would differ at individual physics domains compared to coupled physics domains and would depend on the interactions occurring between the physics domains.

The work reported in this thesis considered the hierarchical approach to design a coupled thermo-mechanical validation experiment consisting of a thermal expansion test (thermal component) and a three-point bending test (mechanical component). The coupled thermo-mechanical test was treated as a multi-physics system and broken down into individual physics components - thermal and mechanical components to allow the design and control of significant experimental parameters, to allow the measurement of all significant inputs needed to develop the computational models and to build confidence in the measurement system setup and the model.

Three essential elements of a validation process exist, as identified from the validation flowchart in the ASME V&V guide. These elements include:

1. ***Validation Experiment***
2. ***Uncertainty Quantification***
3. ***Validation Metric***

The following will be reviewed in subsequent sections of this thesis.

2.2. Validation Experiments

It is common practice to assess the reliability of computational solid mechanics models using experimental data from physical reality. The data can be historical, from traditional experiments or data from new experiments designed with the specific objective of assessing a model's reliability. The latter is known as validation experiments.

Traditional experiments include data from archived literature and databases, which are usually performed to improve the fundamental understanding of an engineering artefact or a component's physical and mathematical behaviour, estimate model parameter values [36], and serve as proof tests [4]. The data obtained from traditional experiments are often not sufficiently adequate to conduct a ***robust or quantitative*** validation assessment because it often lacks ***quality*** documentation of experimental parameters, environmental conditions, or incomplete system response measurements. Therefore, it is essential to design new experiments that are dedicated to model validation.

An example of historical data can be found in the OECD[5]-NEA[6] experimental database, which contains historical data for nuclear energy components such as fuel cladding. The database was set up by a task force from the Nuclear Science Committee (NSC) to address the scientific issues of fuel behaviour. One of the issues identified was the need to provide experimental data from well-characterised experiments that will help inform the understanding of fuel behaviour in steady-state and transient conditions. The action plan from the discussion by the committee was to set up a database that houses different sources of historical measurement data from well-characterised experiments to aid the development of computational models and subsequently aid a robust validation assessment. Implementation of the action plan by the committee resulted in the development of the International Fuel Performance Experiment (IFPE) database of the OECD-NEA. The database is limited to thermal fuel performance with zircaloy cladding and UO_2 fuel material, for which Turnbull has provided a detailed report of the experimental database in [41]. The majority of the data present in the database were obtained over many decades, and some are in formats that cannot be easily accessed due to formatting issues or regulatory restrictions. Moreover, the complexity of the experiments and lack of clear documentation made them challenging to interpret. This reinforced the need and significance of designing new experiments for the purpose of validation, which was an issue raised in the validation round-robin report from the VANESSA[7] and ADVISE[8] projects. Both projects addressed the need to perform specific experiments to obtain quality and quantitative data to determine the predictive

[5] Organisarion for Economic Co-operation and Development (OECD)
[6] Nuclear Energy Agency
[7] VANESSA: Validation of Numerical Engineering Simulations – Standardisation Action
[8] ADVISE: Advance Dynamic Validation through integration of Simulations and Experimentation

capability of computational models. More recently, a new validation flowchart, the MOTIVATE[9] validation flowchart, has been proposed for the purpose of validating computational simulations that allow the use of historical data [42]. The flowchart is an extension of the ASME flowchart that allow the use of historical data and the design of new experiments providing more options to achieve a validation assessment.

2.2.1. Quality Experimental Data and Documentation

Unlike traditional experiments, validation experiments should be well-characterised, carefully designed and relevant to the intended application of the computational model with great emphasis on "robust" and "precise" data. The characterisation is a crucial goal as it impacts the quality of the experiment and refers to measurements of all the essential characteristics of the experiments needed for the computational model. In other words, validation experiments are carefully designed, executed and analysed to determine how well a mathematical model and its embodiments in a computer code can simulate a well-characterised physical process [43]. For any experiment to be classed as a validation test, it must be designed to capture the physics of interest and include an accurate prescription of the specimen geometry, initial conditions and boundary conditions, and other significant parameters essential for the model development [44].

During such a test, the data collated must be fully documented and include all assumptions made, such as the initial boundary conditions, applied loads or system excitations, the system's measurement responses, and measurement uncertainty to help develop a corresponding model. Quality documentation of an experimental design and execution should have the characteristics of a validation experiment listed in the guideline presented in [44].

2.2.2. Quantitative (Robust) Experimental Data

Over the years, it has become common practice within the solid mechanics community to compare the results output from simulations and measurements using data collected from hot-spots in specific regions of the specimen with instrumentations such as strain gauges, extensometers, or thermocouples, depending on the application. These methods are referred to as point-by-point measurement techniques. The disadvantage of using such point data is that it may result in partial validation because an area on the specimen containing significant strain or deformation data fields may have been neglected. Also, the region of high stress predicted by the simulation may be present elsewhere and could result in component failure. The data generated from hot-spot locations on a specimen are often not comprehensive enough to make a quantitative comparison with data from an equivalent computational simulation. It has been recommended in the literature [12] to use

[9] Matrix Optimization for testing by interaction of Virtual and Test Evironments

comparable data sets from both measurements and simulations to perform a robust validation assessment.

It is possible to obtain more comprehensive data-fields from the use of experimental optical techniques such as photoelasticity, which involves the use of optically sensitive material to construct the model of a structure to be analysed for stress/strain behaviour, and thermoelastic stress analysis (TSA) which exploits the principle of thermoelasticity to determine surface stressed in a dynamically loaded body. Advances in the application of these non-contact optical measurement methods have driven the development of new technologies such as digital image correlation (DIC) [45]. DIC is a non-contact optical method for the measurement of displacement/deformation of a structure subjected to system loading. The principle of DIC has been described by Sutton et al. [46], [47] [48], and has been applied in the field of science and engineering for the measurement of full-field displacement and deformation of structures or engineering artefacts [49] [50] [51] during loading applications. The technique has also been successfully modified for use in high-temperature environments [50], [52] [53], [54] for deformation measurements. This measurement technique provides a straightforward and cheap method for capturing material changes under specific loading conditions and can generate comprehensive data sets of the order 10^6 data points and are similar to the data output from a computational simulation. The data generated from such techniques are rarely in the same coordinate systems or have similar data pitch or orientation and can be classed as big-data, making a point-by-point comparison of such a data-rich field impractical and cumbersome to interpret. Therefore, the data-rich fields need to be represented in a format where direct comparison from which a validation statement on the reliability of the prediction and measurement can be developed. This will allow decision-makers to assess and quantify their confidence in the computational model. The image decomposition method can be employed to represent the data-rich field in a form that allows a direct comparison to be achieved.

2.2.3. Image Decomposition Method

As established in the previous section of this report, using a DIC measurement method provides the opportunity to capture data-rich fields of more than 10^4 data points or colour maps of deformation similar to the output generated by a simulation. However, the quantity of such data can make it cumbersome and render a direct comparison between two strain or displacement fields impractical on a point-by-point basis. This issue has been addressed by a series of European collaborative research projects, including ADVISE [10], VANESSA [11], and, most recently, MOTIVATE [42]. These projects investigated the challenges of using full-field deformation maps, such as strains to implement a validation process relative to an industrial environment. As part of these projects, the research activities have led to the development of efficient tools for post-processing full-field images of strain or displacements using image decomposition [55].

Over the last decade, image decomposition methods have been extensively researched to process measured and predicted displacement and strain maps or fields [55] [56]. The measured strain or displacement fields obtained using optical measurement techniques, such as DIC, and the predicted field obtained from a finite element analysis, are treated as images. Image decomposition uses orthogonal moments to reduce the dimensionality of these images from the order of 10^6 to 10^2 to two sets of feature vectors that represents the measured and predicted data while preserving the vital information regarding the deformation of the entire surface of the component. The feature vectors contain the shape descriptors, which are the coefficients of the orthogonal polynomials used to describe the image. Therefore, for a selected set of appropriate polynomials contains the required information that uniquely describes the essential features of the image. The outcome from the decomposition process produces two unique and equivalent feature vectors that can be directly compared using a validation metrics as part of the validation assessment process.

Patki and Patterson [57] have shown that full-field displacement and strain data obtained from measurements and simulations can be processed and represented by feature vectors using image decomposition techniques [56]. Burguete et al. [58] successfully used DIC and image decomposition techniques with shape descriptors to analyse displacement fields on a car bonnet liner subject to high-speed impact. Another study in the literature [59] proposed a validation approach based on an image decomposition technique for reducing the dimensionality of strain data obtained from a computational model and an experiment to allow a quantitative comparison. The work has been embedded in the CEN[10] Workshop Agreement [12], also known as the CEN guide, and is shown in the flowchart from the guide depicted in figure 3.

Since the data obtained from a validation experiment serves as a standard against which the accuracy and reliability of the model output are assessed through comparison, it is essential to include the errors or uncertainties associated with the measured data. The uncertainty associated with the measurement forms part of a quantitative validation exercise.

The following section of this thesis is a literature review on state-of-the-art uncertainty quantification methods in the science and engineering community and their applicability to the research topic discussed in this thesis.

[10] European Committee of Standardisation (CEN). Validation of computational solid mechanics models, CEN Workshop Agreement, CWA 16799:2014 E.

2.3. Uncertainty Quantification

Uncertainty is a significant component of every decision-making process and a critical component of a quantitative validation assessment, as depicted in the flowcharts of figures 2 and 3. The uncertainty associated with a measurement helps to inform decision-makers on the reliability of the outcome from a quantitative comparison assessment. In the context of this thesis, uncertainty is described as a method of expressing measurement errors. On the other hand, an error can be described as the difference between a measured value and the expected value of a measurand.

Uncertainty quantification (UQ) is also essential to assess reliability and credibility and subsequently increase confidence in the results acquired from model predictions and experiments. The ASME V&V [5], [6] process recommended that a robust validation assessment must include an estimate of the experimental uncertainties for all the measured system response quantities (SRQs) of interest and, where possible, the computational model which is being assessed. Roy and Oberkampf [44] also provided a guideline for the design and execution of validation experiments, which recommended that experimental design should be constructed to analyse components of random and systematic uncertainties. Random errors can be due to inherent variability of a test specimen, environmental test conditions, and errors associated with system loads. While systematic errors are examples of errors that arise from a measurement system. However, care should be taken to quantify the significant sources of errors to avoid having large uncertainty bound that makes the model not useful.

Uncertainty quantification can be described as the process of identifying, characterising and establishing those factors in the analyses of complex systems, physical tests and computational models that impact the accuracy of the results. The term accuracy can be described as how well the measured data approximates the actual theoretical value. On the other hand, precision can be described as the degree to which individual measurements vary around a central measurement value. UQ enhances a quantitative validation exercise as opposed to a traditional graphical presentation of visual comparison between two data sets (which often does not account for the experimental errors).

According to ASME V&V 2012 [6], a validation plan must specify a metric that incorporates the uncertainties in a method that generates a single measure of the relative difference between the simulation outcomes and the outcome from a validation experiment in a probabilistic framework. Roy and Oberkampf [23] added that such uncertainties should be propagated through the simulation using either Monte-Carlo or Latin-hypercube sampling technique to evaluate the impact on the final outcome, which can be accompanied with a sensitivity analysis.

2.3.1. Aleatory and Epistemic Uncertainties

There are two common categories of uncertainty: aleatoric and epistemic uncertainties [60], [61], [62]. Aleatoric, also known as irreducible uncertainty, is associated with randomness and variability in the system response quantity (SRQ). It is often not possible to reduce this kind of uncertainty because nothing can be precisely measured. However, such uncertainty can be characterised using a probability density function (PDF) or a cumulative distribution function (CDF) [6].

On the other hand, epistemic or reducible uncertainty arises due to a lack of knowledge or incomplete knowledge about the system under analysis. When different measurement methods generate different results, and it is unknown which results are more accurate, such is an example of epistemic uncertainty. Unlike aleatory uncertainty, it can be characterised by an interval range value with no assumed probability distribution [63]. This type of uncertainty can be reduced through additional or improved knowledge of the system, e.g. through expert opinions (subjective approach), or through conducting further experiments to understand a specified quantity of interest or parameter. Both types of uncertainties are related to computational and experimental results [64].

Numerical simulations are often packed with epistemic uncertainty because of approximations in modelling and simulation to make them more practical to use. Every approximation made in a model leads to a loss of information. For example, the use of simplified structural geometry and boundary conditions, linearization of non-linear relationships, idealised physical laws are some categories of sources of epistemic uncertainty present in a computational model. Extensive research has been performed in this field in the last decade, particularly in research areas of reliability and risk analysis, sensitivity analysis and design optimisation, which has resulted in the development of various methods for identifying and characterising significant sources of uncertainty. Some of these methods include Bayesian analysis [65][66], Monte-Carlo sampling [67], Interval probability methods [67], Design of Experiments, and Sensitivity analysis [68]–[70].

Uncertainty is also inherent in the physical system. It is essential to separate aleatory and epistemic uncertainty sources to avoid unnecessary costs and wasted time trying to reduce irreducible errors. For example, if the variation within a system is aleatoric but characterised as epistemic, money, time, and resources could be wasted trying to reduce the irreducible uncertainty. On the other hand, treating epistemic uncertainty as aleatory may lead to an inaccurate representation of the model's predictive capability. Therefore, understanding and quantifying the significant sources and types of uncertainty, especially for multi-physics systems, enables informed decision-making about the predictive capability of a computational model and for better allocation of resources.

2.3.2. Uncertainty Quantification of Multiphysics systems

Multi-physics systems have numerous sources of errors; however, not all are significant because not all of the errors significantly impact the outcome of the measurements or predictions. Attempting to quantify all sources of the uncertainty will be costly and generate large uncertainty bounds that make it challenging to evaluate the usefulness of a model. This can pose a challenge for multi-physics systems due to the several sources of uncertainty present in the different physics domains, raising the question of how to identify and propagate the significant uncertainty from the different physics domains to account for the uncertainty in the coupled-physics phenomena. Having large uncertainty bounds may result in a false representation of a model's predictive capability. In a multi-physics system, the sources and magnitude of errors would differ from one physics domain to another, usually related to the level of complexity, number of components involved in the physical system, coupling methodologies, and interactions present in such a system.

Over the past decade, the field of uncertainty quantification has been significantly explored, which has led to different proposed approaches and methods for quantifying uncertainty in single physics domains [60] [71],[72]. For example, Hanson [72] suggested a probabilistic Bayesian method for quantifying uncertainties in simulation. Flage et al. [73] demonstrated the use of probability bounds analysis for quantifying epistemic uncertainty within a risk assessment context. Their methods have not accounted for the uncertainty in multiple physics domains, which is one of the challenges of multi-physics analysis. Recently, Urbina and Mahadevan [28], [74] proposed a Bayes network approach to allow uncertainty analysis from different physics domains. Their work suggested a framework that allows the quantification of uncertainty in a hierarchical system which was supported by Thacker's tutorial [36] on the importance of hierarchical validation for complex systems. The V&V qualification framework for coupled multi-physics models is based on the qualification procedure for separate physics models or phenomena [75]. Therefore, it is reasonable that the UQ of multi-physics systems is performed based on separate physics components following the V&V framework.

Most of the research on the quantification of uncertainty in multi-physics systems has been based on computational models, with little work performed on the actual physical systems or experiments. The nuclear industry has particularly been investing in research to generate extended qualification methods that include uncertainty quantification and propagation in their coupled simulation codes (e.g. coupled neutronic/thermal-hydraulic codes) for Light Water Reactors (LWR) that simulate the processes of a physical system [75], [76]. Sun et al. [77] have recently suggested a hybrid approach to building an integrated UQ methodology which consists of an "intrusive" and "non-intrusive" method applicable for a modern-day component-based approach for multi-physics simulations. In intrusive UQ methods, knowledge of the governing equations that underlie the simulation codes is required.

This method represents the input uncertainties through a parametric representation such as Taylor series [78] or orthogonal polynomials [79]. Their method provides a flexible approach and algorithms for UQ in complex systems and can be adapted to address different problems of a multi-physics and multi-scale nature. Another work in [80] proposed an intrusive UQ method that investigates multi-components PDE models, that is, models coupled through network coupling interfaces. Their method exploits the structure of a network multi-physics system to construct a reduced polynomial surrogate of the model output as a function of the uncertain inputs parameters. This method could help address the challenges of collecting uncertainties from separate physics models into a set of inputs which may generate a s high-dimensional input space and make it impractical to construct surrogate models.

More recently, in the nuclear energy industry, work has been carried out on UQ methods for multi-physics and multi-scale systems, such as nuclear light water reactors. The demand to advance the best-estimate predictions with associated confidence bounds is on the increase for nuclear reactor performance and safety analysis. This research has resulted in developing an uncertainty propagation technique based on a stochastic sampling method that considers the uncertainties from basic nuclear data and fuel modelling parameters [81] [82]. They recommended that UQ methods for novel applications should include consistent propagation of a substantial number of uncertainties and sensitivities through separate physics phenomena coupled with non-linear feedback impact on a refined local scale. Due to the vast amount of uncertainties present in a multi-physics system, a local or global sensitivity analysis can be employed to identify significant sources of errors in a computational model.

Sensitivity Analysis

Sensitivity analysis (SA) is a specific component of uncertainty quantification employed to determine the degree to which the uncertainty in a system or result analysis from a system and a model depends on the uncertainty of each input parameter [83], [84]. For example, given that a change of an input parameter X generates a measurable change in the output parameter Y, it is possible to determine the sensitivity of Y to X [85]. The sensitivity can be derived by a direct or an indirect calculation method. It is usual to employ a sensitivity study at the early phase of a system design to identify critical design parameters that can impact the system performance, especially for complex systems with multiple physics domains. The philosophy underlining SA is that if the relationships and the relative significance of design parameters are understood, the system's performance can be easily improved or optimised.

There are several SA methods. Most of these methods are based on the derivatives of one variable with respect to another whilst other parameters are held constant, also known as the *one-parameter-at-a-time* (OAT) approach [86]. This approach only provides a measurement of the sensitivity at the point where the derivative is obtained. Extrapolation around this point is only possible for linear systems. This type of SA may be referred to as "*local sensitivity analysis.*" [68]. The *global sensitivity analysis* has been used to address the limitation of the local sensitivity analysis methods. This method can be used to evaluate significant input parameters or factors by varying all other input factors in the domain space, taking into account the input parameter distributions. Some common approaches of global SA include Monte-Carlo techniques [84] and response surface methods [87].

Contrary to the local SA, the global SA does not segregate any initial sets of model input values but considers the model in the entire domain of possible input parameter perturbations [88] [89]. The third category of SA methods is the *screening approach* which focuses on the functional relation between inputs and outputs. Unlike the global SA method, the screening approach does not consider the input parameter distributions. The screening method proceeds from the field of *design of experiments*. It is commonly used to deal with problems involving a large number of input parameters where only a few of these parameters may influence the output from a systems or model analysis.

The uncertainty and sensitivity analysis literature reviewed here is more on addressing the need to provide reliable predictions with confidence bounds based on the uncertainty of the input parameter used in a model. In this thesis, a local sensitivity was explored during the design phase to identify the critical input parameters. The sensitivity coefficients of these parameters were determined and considered along with the measurement uncertainty as part of the validation assessment.

2.3.3. Measurement Uncertainty

Epistemic uncertainty is often predominant in computational models. As mentioned in the preceding section of this thesis, this type of uncertainty can be reduced through additional information or knowledge about the parameters or conditions of interest. The additional information can be obtained from expert opinions or from an objective designed and tested experiment. Since the measurement data obtained from the experiment serves as a standard against which the accuracy of the model output is assessed through comparison, it is essential to include the errors or uncertainties associated with the measured data as the first step toward validation. All measurements are subject to uncertainty, for example, the standard deviation from a repeat experiment. Therefore, a measurement result will be incomplete if not accompanied by a statement of the sources of errors and associated uncertainty.

According to GUM[11] [90], [91], the uncertainty of a measurement describes the dispersion of a value centered on the measurement value with a stated probability. Several components that contribute to the uncertainty of a measurement include the uncertainty associated with the test environments, the

[11] Guide to Uncertainty of Measurement (GUM)

variability of the test component, the experiment set-up, and the measurement devices (instrument error). The information about the total uncertainty associated with a measurement is critical when the physical test is required for certification purposes.

Measurement device errors, such as the errors associated with DIC systems, can be random or systematic. Pan et al. [45] provided a review on 2D digital image correlation methodologies, including the different correlation algorithms and sources of errors that influence the accuracy of the measurements obtained with the device. In recent years, some of the errors associated with DIC have been investigated considerably. Haddadi and Belhabib [92] investigated the sources of errors associated with DIC when applied to strain measurements and divided the errors into those related to experimental setup and those from correlation algorithms. They used rigid body translation of a specimen in an attempt to quantify these sources of errors and also provided recommendations for reducing some of the errors that were identified as part of their work. Another work in [93] proposed an optimised pattern quality metric as a means to increase the accuracy of DIC techniques. Some other methods [94] have involved the use of a synthetic un-deformed image to generate shifted or deformed images by applying a polynomial interpolation scheme in an attempt to assess DIC errors. Uncertainty analysis for 3D DIC has also been researched. Sutton et al. [95] have investigated uncertainty in 3D DIC based on the effect of camera alignment and positioning error, while Siebert et al. [96] made a comparison between 3D DIC to electronic speckle pattern interferometer (ESPI) and strain gauges in a tensile test and some dynamic tests using a cantilever.

The studies of uncertainties associated with DIC systems highlighted above have investigated its limits from a theoretical aspect and provide insight into the capabilities and limitations of the technique in general. Some of these investigations also attempted to provide a limitation of the DIC method when performed under laboratory conditions. However, these studies do not provide information about the level of uncertainty obtained with a specific system setup used in a routine experiment. The Standardisation Project for Optical Techniques for strain measurement (SPOTs) provided a solution to this issue by designing a reference material to calibrate optical systems for strain measurements [97]. The term calibration is defined in the International Vocabulary of Basic and General Terms in Metrology (VIM) [98] as an "*operation that under specified conditions, in a first step, establishes a relation between the quantity values with measurement uncertainties provided by measurement standards and corresponding indications with associated measurement uncertainties and, in a second step, uses this information to establish a relation for obtaining a measurement result from an indication*." On the other hand, reference material can be described as one that has one or more of its properties sufficiently established to be utilized for calibration of an apparatus and provides traceability through an unbroken chain of comparison to a national or international standard. The outcome of the calibration process is to relate the uncertainty of the system to some national standard through an unbroken chain of comparisons.

It is important to note that the calibration procedure, such as the one developed by the SPOTs project, is different from the calibration performed during a routine DIC setup in which the intrinsic and extrinsic parameters of the system are determined with the application of a precision manufactured target. The procedure developed by the SPOTs project was designed to produce a *minimum measurement uncertainty* for a particular experimental setup. It is referred to as a minimum uncertainty associated with the experiment setup because it is an idealised process that may not capture all the sources of uncertainty associated with the experiment. More recently, Siebert et al. [99] have proposed a new method that attempts to capture all sources of uncertainty associated with DIC measurement on an industrial scale to address the issue of idealisation highlighted above. The method utilises the calibration target, which is usually used for the calibration of a DIC system and a designed compression buckling test of an aircraft fuselage to demonstrate their proposed method.

The reference material proposed by Patterson et al. [100]. for in-plane strain measurement features a beam subjected to a four-point bending within a monolithic frame. Although this reference material was successfully used to establish measurement uncertainties for Electronic Speckle Pattern Interferometry (ESPI) and DIC, it is not without limitations. The geometry of this material is complicated and makes it challenging and expensive to manufacture. The test setup for use in a calibration test is also not seamless and requires the determination of correction factors in the procedure.

Hack et al. [101] have recently successfully used a designed reference material, which features a simple geometry to establish uncertainty of full-field displacement measurements through a calibration experiment. In this work, a cantilever reference material was used to evaluate the uncertainty associated with measurements of static in-plane and out-of-plane displacements. The geometry and schematic diagram of the cantilever is defined in the CEN guide [12] and is designed to be scalable; therefore, all the dimensions are expressed as a function of the cantilever's thickness (T). this material features a thick base section that is securely clamped to an immovable surface during loading application.

In this thesis, the minimum measurement uncertainty for the thermal, mechanical, and thermo-mechanical experiments was established via carefully designed calibration experiments and using the same cantilever reference material for in-plane displacement by Hack et al. [101] whilst following the procedure in the CEN guide [12] to quantify the total measurement uncertainty associated with each experimental campaign. It is proposed in this thesis that the concept of the **superposition principle**, which has its ancestry in the field of mathematics and physics, can be explored to evaluate uncertainties of multi-physics models based on the uncertainty quantified in each physics domain.

A detailed discussion on how the measurement uncertainty was achieved for this research is found in chapter 5 of this thesis.

2.4. Validation Metrics

A validation metric is an essential aspect of a validation assessment because all model validations aim to compare measurement results with simulation results. A validation metric is simply the mathematical distance between a measurement and prediction result. The metric could range from a simple binary metric to a more complex form of metric. It is desired that the outcome from a validation metric should be objective and be accompanied by a quantitative statement stating the agreement or disagreement between the simulation and measurement. The statement should also include a measure of the variability in the defined agreement and a confidence interval [102]. Usually, a low value of the metric indicates a good agreement, and a higher value shows a significant disagreement. Roy and Oberkampf [23] reviewed approaches for achieving quantitative comparison of predictions and measurement results which included uncertainty analysis. Their work takes a philosophical approach and emphasises the significance of performing a robust uncertainty quantification as part of the validation assessment. The work by Oberkampf and co-authors in [35], [102] recommended seven desired properties that validation metrics should have to be useful in the evaluation of model accuracy in the science and engineering community. The properties recommended for a validation metric include: an estimate of the numerical solution error, assessment of the physics-modelling assumptions, inclusion of experimental data post-processing, estimates of the experimental uncertainty, inclusion of aleatory and epistemic uncertainty, exclusion of any adequacy information, and the metric should be a true distance measure.

According to Liu and co-authors [103] and [104], validation metrics can be grouped into Deterministic and Stochastic metrics. Both metrics can be grouped into four categories of validation metrics from a philosophical view according to [103], which include:

1. ***Hypothesis Testing***: In hypothesis testing, two statistical statements, the null hypothesis and the alternative hypothesis, are pre-defined in order to assess if the result from the prediction lies within the measured distribution [105]. This method only provides a "yes" or "no" statement (Boolean statement) of validity about the agreement between the prediction and measurement and does not include the ***confidence level*** of the difference. Classical hypothesis testing is a well-developed method for rejecting a model based on statistical error [102]. This approach comprises of two elements: feature extraction and a quantitative assessment [106].

The goal of feature extraction is to reduce the dimensionality of the data used in a model assessment and to improve the accuracy of the model validation [107]. The relative error metric is an example of a feature extraction method that has been employed in the field of model validation [108].

2. ***Bayesian method (Bayes formula)***: Similar to the classical hypothesis testing, the Bayesian analysis does not directly indicate the validity of a model. However, it does not focus on rejecting the null hypothesis but on accepting it with a defined level of posterior confidence based on prior knowledge – the Bayes factor [103]. In most literature, the Bayesian approach is commonly used for model and design optimisation by calibrating the model parameters with data from a measurement [109] and for uncertainty quantification [110],[66] and is not necessary for validation.

3. ***Area Metrics:*** The area metric measures the agreement of an entire distribution of prediction and measured data sets. It is only appropriate for a few data sets or point data and does not give any criteria for determining the acceptance of model validity. Therefore, the area metric is not suitable for large data sets such as the one obtained with DIC optical measurement technique.

4. ***Frequentist Metrics***: Frequentist metrics differ from hypothesis testing because they do not make use of a Boolean "yes" or "no" statement about the agreement between a model prediction and measurement. This method is based on quantifying the difference between two data sets or by a measure of error difference. Oberkampf and Barone [102] quantified such agreement by measuring the distance between the mean of the prediction and the estimated mean of the measured data. Their work analysed the experimental uncertainty by a confidence interval due to insufficient experimental data. Their approach is limited to a system where the response quantity of interest is close to zero or cannot be time-averaged, as with the case of many applications. Kat and Els [108] employed an absolute percentage error method for each pair of data points to combat this issue. These values were assessed against a pre-defined threshold. By doing so, they could state the probability of the prediction producing results within the defined requirements. It is important to stress that their approach was based on a deterministic validation metric, which meant that the measurement uncertainty was not considered. Recently, Dvurecenska et al. [111] have provided a probabilistic validation metric based on a relative error that allows full-field data to be compared and to assess the reliability of computational solid mechanics models. This work may be seen as an extension of the work by Kat and Els [108] since the validation metric

considered the uncertainty in the measurement data and also provides a statistical statement on the validity of a model.

The work reported in this thesis employs the relative error metric described in [111] in conjunction with error bar plots to quantify the quasi-real-time displacement data acquired during the experimental campaign.

2.5. Conclusions

Several approaches have been developed to validate computational models over the past two decades to build confidence in the model and establish credibility. This is still an area of active research as there is a need to design safe engineering systems and maintain structural integrity during service life. The current state-of-the-art validation approach and strategies presented in the V&V guides and recommended by other authors highlighted in this thesis describe the process of validating a computational model parallel to the corresponding experiment. Their validation process flowchart applies to a single physics problem, and many real-world and engineering modelling efforts necessarily involve complex interconnecting systems with multiple interacting physics domains. It has been recommended in literature to apply the building block or a hierarchical validation approach to complex systems that involve multiple physics domains; by so doing, the multi-physics system is split into a single physics domain. This method allows the credibility of a multi-physics model (involving more than one physics and system load) to be assessed based on the confidence established for each physics model. The hierarchical approach is heavily dependent on linearity and does not apply to non-linear systems and those with evidence of emergent behaviour. Emergent behaviour is typical for complex systems with multiple interconnecting components, multi-physics and multi-scale domains. Since this type of behaviour arises from the interactions between different physics domains and between multiple interconnected components, it becomes reasonable to design coupled experiments that account for the different physics modelled by a corresponding computational model, as this would be a realistic representation. Designing multi-physics tests, which often involve the deformation of a test specimen subjected to more than one system load simultaneously, is usually not a trivial task.

It has been recommended in this thesis that the hierarchical approach can be employed to design well-characterised experiments in single physics domains, which allows the measurement of all significant input into the model to be acquired. It also helps identify significant uncertain parameters, design control measures for the experiment, and build confidence in the design, build, and test of the multi-physics system.

2.6. Knowledge Gaps

It has been identified from the literature review that multi-physics systems can be treated as complex systems that can be decomposed into simpler physics domains. This allows each physics domain to be carefully designed and tested to acquire well-characterised measurement data for a quantitative validation assessment for the couple computational model. However, there is currently no validation processes or accompanying flowchart for multi-physics simulations. This presents a need to extend the current ASME validation flowchart and the processes in the CEN guide flowchart to account for multi-physics simulations, which include:

- An approach for combining data and the associated uncertainties from different physics domains to account for the multi-physics effect,
- The application of a validation metric to test the accuracy of the multi-physics simulation based on the uncertainty quantified at each physics domain,
- A statistical statement of the level of agreement (accuracy) between the simulation and the measurement based on the uncertainty from each physics domain, and the presence of interaction effects.

Chapter 3

3. Proposed Enhanced Validation Process Flowchart

This chapter details the proposed validation approach for multi-physics simulations whilst acknowledging the different philosophical positions to model validation in the science and engineering community.

An Enhanced (extended) validation flowchart in figure 7 is proposed as part of this research project to address coupled physics phenomena. The development of the enhanced validation approach started from the schematic diagram in the ASME V&V [5] guide with input from the CEN guide [12].

Three sets of experiments, thermal expansion, mechanical bending, and combined thermo-mechanical tests, were carefully designed, built, and tested to demonstrate the processes in the enhanced flowchart. The thermal expansion component (measurement and simulation) is referred to as physics domain 1, while the mechanical bending test is referred to as physics domain 2. Each physics domain in the flowchart represents the flows in the ASME flowchart, with additional features for this research illustrated by the processes in the coloured boxes in figure 6. These processes have been specifically developed to handle multi-physics phenomena and the challenges identified in Chapter 2, including designing an experiment with multiple simultaneous system loads (or multi-physics experiments) and the integration of uncertainty from multiple physics domains.

The philosophy of the tiered approach to validation of complex systems was adopted for this research, implying that the multi-physics system or coupled phenomena (thermo-mechanical) was split into single physics domains (thermal and mechanical physics domains) to allow the design and test of well-characterised validation experiments. It is essential to provide sufficient evidence through a rigorous validation exercise to support the model's fitness for use and build confidence that the prediction from the simulation is an accurate representation of the physical system. This approach can be described as "Empiricism." Patterson and Whelan [26] described Empiricism as "inductive generalisation", where conclusions are based on observation data, and the only assumptions permitted are those that can be independently and empirically confirmed to be included in the model. This type of quantitative validation is desirable for fewer levels of complexity (single physics components) where it is possible to design and perform experiments because it will help to establish credibility for coupled multi-physics phenomena where it may be impossible to design physical tests.

The following section is a discussion of the methodology of the enhanced validation processes and flowchart.

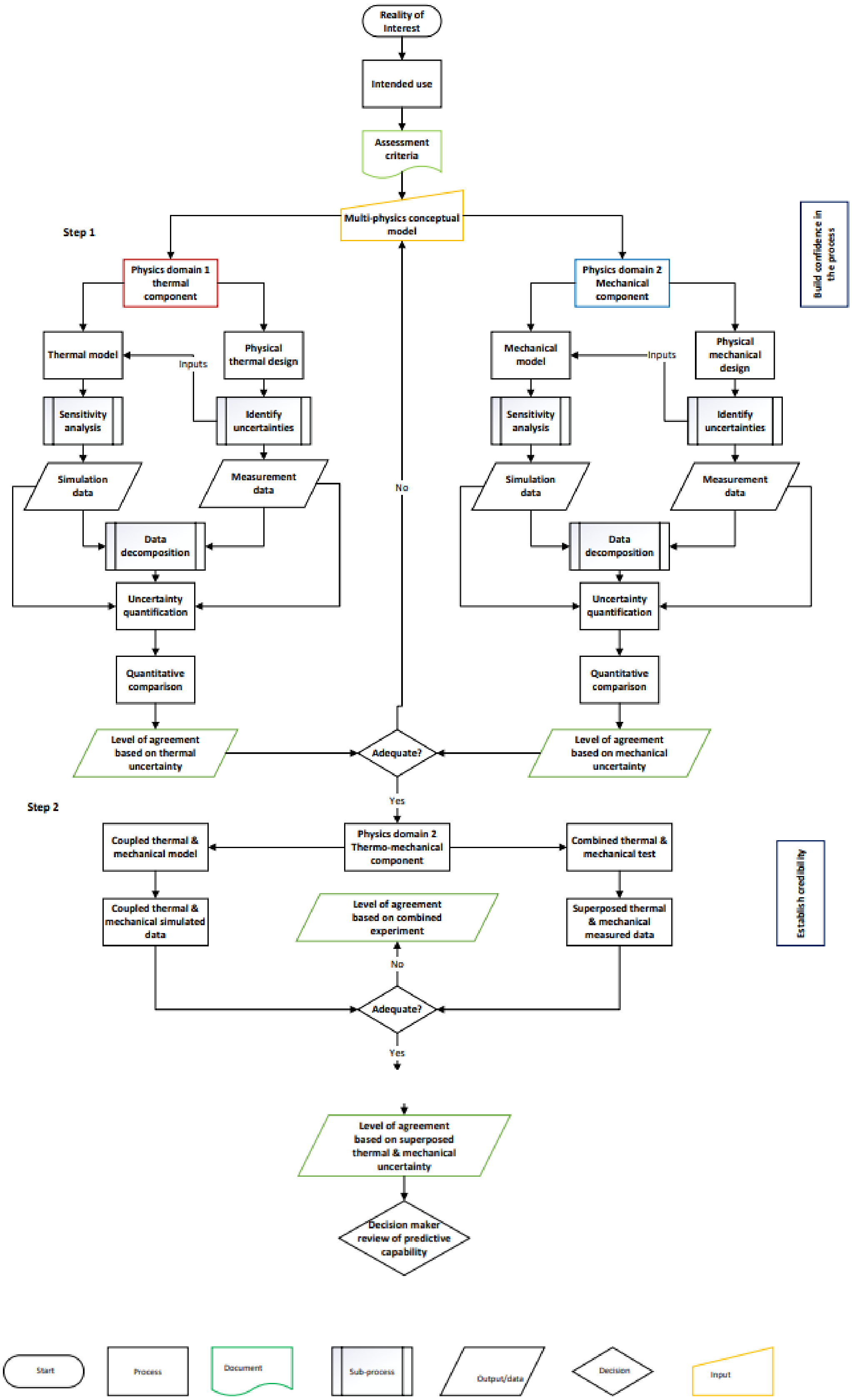

Figure 7: Enhanced validation process flowchart for coupled physics phenomena

A pdf copy of the flowchart, with a bigger font, is attached to this thesis.

3.1. Methodology of the Enhanced Processes in the New Flowchart

The validation approach illustrated in figure 7 follows the structure of the flowchart in the ASME and CEN guides. Each physics domain represents the flows of the ASME V&V flowchart. The process starts with identifying the 'Reality of Interest'**:** the aspect of the real-world problem being studied to assess its performance. This could be a component, sub-system, or full system scale problem. This research work addresses a component scale problem – an idealised nuclear fuel cladding.

Once the reality of interest is identified, the intended use and assessment criteria are defined from which a conceptual model is built, and this involves developing a specification of the physical system and its environment. This includes the statement of assumptions, physical interactions, physical properties, geometry, and the response quantity of interest. The problem statement made during the conceptual phase is then used as an input to develop both the mathematical model, which describes the physical reality of the problem to be solved and as an input to the physical testing.

Unlike the classical V&V flowchart in the ASME guide, the consideration of multi-physics problems has been introduced by extending the flowchart to include an additional physics domain in a hierarchical framework. In this work, a coupled thermo-mechanical component is assumed to be the multi-physics system which is split into the thermal (physics domain 1) and the mechanical (physics domain 2) components, as depicted in figure 7. The hierarchical approach to validation promotes splitting the multi-physics problem into single physics domains, as depicted in figure 7. The splitting of the multi-physics system into simpler components, also known as "divide and conquer",— involves decomposing a system with multiple interacting physics domains into smaller and simpler components where the physics is known and can be tested. The advantage of this approach is that it allows the design of experiments at simpler scales for which well-characterised measurement data required to develop and simulate the corresponding model can be obtained (depicted by the input connector from the physical design to the model in figure 7), which is a critical aspect of a validation exercise. This approach also enables a straightforward identification of which aspects of the experiment and model should either be considered fixed or uncertain (random). Where changing a parameter results in no significant change to the output (response) quantity, such a parameter should be treated as a single-value (fixed). Decreasing the layers of physics could transform a meta-model into a testable model and makes it straightforward to build confidence.

Once all the sources of errors and uncertainty in the physical designs and in the models have been identified for the different physics domains, the implementation of the computational model results in the simulation output. Similarly, the test of the physical system generates full-field response data. This research work used a digital image correlation measurement method to obtain full-field surface displacement from the idealised fuel cladding (the case study for this work) when subjected to elevated temperature and bending loads, while the finite element models were developed using Abaqus simulation software. The full-field data obtained from the simulation and measurements were decomposed using the orthogonal image decomposition methodology described in section 2.2.3 of chapter 2 of this thesis.

The feature vectors obtained from the image decomposition, which correspond to the simulation and measurement for each physics domain, are compared against each other to assess the model's reliability. A crucial step in assessing the reliability and confidence in the model is to quantify the measurement uncertainty in the experimental data. For this work, the minimum measurement uncertainty for the experimental setup for each physics domain is evaluated through a calibration experiment for optical systems detailed in [101]. A detailed description of the calibration experiment to assess the minimum measurement uncertainty for each experimental campaign is discussed in chapter 5 of this thesis.

On the other hand, the computational model is developed with inputs from the conceptual. The first step in the modelling process is to identify all sources of uncertain input parameters that can cause significant changes to the simulation output. This can be achieved through a local sensitivity analysis. Input parameters that result in a considerable shift in the output quantity can be treated as random. The sensitivity analysis is deployed to identify significant input parameters in the model to facilitate the statistical characterisation of such parameters. It is recommended here that a simplified local sensitivity analysis should be performed for the model to identify significant parameters from each physics domain to facilitate the creation of an uncertainty budget, which is a detailed list of different sources or components that contribute to the total uncertainty for each physics component. Where the physics occurring in each domain is known, a one-at-a-time (OAT) sensitivity technique could be employed to determine the variation in the model output due to a change in the input parameters to aid a robust validation assessment.

For this work, a logical structure or process flowchart, such as the one illustrated in figure 8, is developed for multi-physics systems to accompany the enhanced process flowchart. This was designed to help capture and help propagate significant sources of uncertainty through the system. Such structure will also help create an expression of the system equation in a mathematical form. The system equation describes the influence of all uncertainties of the input variable on the output quantity. The structure in figure 8 is similar to a simplified block diagram and captures the systematic (bias) and the statistical (random) uncertain influences from the multi-physics experiment. The statistical influences can be identified through repeated measurements or scientific judgement based on other sources of information, such as manufacturer's specifications and calibration certificates. The systematic influences can be determined from calibration experiments by comparing measurements with different setups, devices, or analytical solutions. The uncertainty determined for each component in the flowchart of figure 8 can be combined following the guidelines in [90] to produce the total measurement uncertainty.

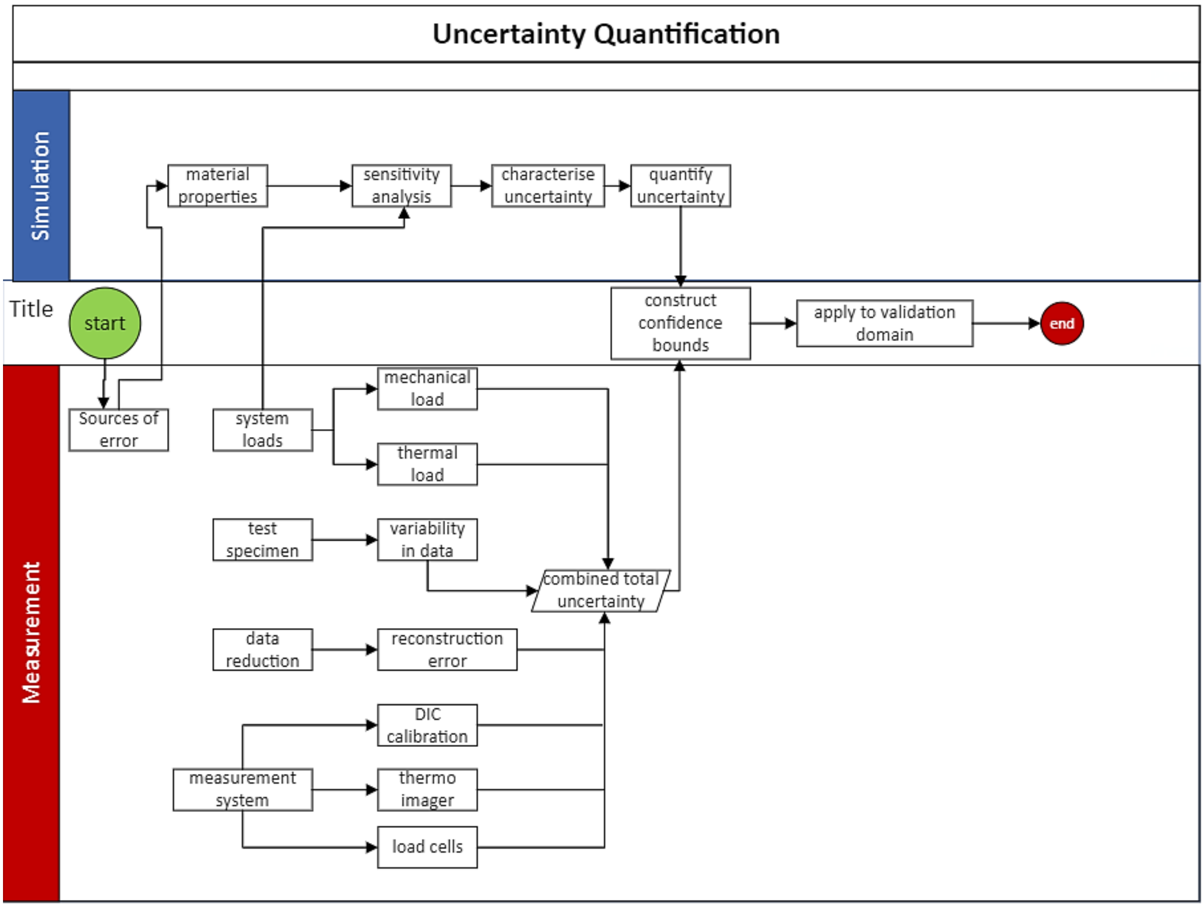

Figure 8: Logical structure for uncertainty quantification and propagation

The quantitative comparison of the measurements and simulations shown in the flowchart of figure 7 for the individual physics domain follows the procedure detailed in the CEN guide [12]. The agreement can be measured by quantifying the difference between the measurement and the simulation results using an absolute relative error metric [111], which can then be expressed as a probabilistic statement, e.g., the expected error with associated confidence limits. Once an acceptable level of agreement is established based on the assessment criteria and minimum measurement uncertainty, the system response (e.g., displacements, strains and stresses) from the individual physics domain can be combined by deploying the Superposition Principle for linear elastic systems.

The Superposition Principle or Property for linear elastic systems has been extensively established in science and engineering. Its history can be traced back to quantum mechanics states and the linear circuit theory, and the term was first used by Helmholtz [112] in 1853. The principle states that for linear elastic systems, the response $y(t)$ due to multiple inputs of $x_1(t)$, $x_2(t)$,… $x_n(t)$, acting simultaneously and independently on the system, is equal to the sum of responses of individual input; also known as a **resultant** response. Suppose the principle of linear superposition is maintained; in that case, a system will behave such that any multiplicative change of an input by a factor implies a proportional change of its output by the same factor. In this context, the factor can be a constant.

This principle applies to linear elastic systems and allows straightforward decomposition of linear systems into sub-systems [113]. This principle has been applied in the literature [114]–[121]. Kim and Cho [116] successfully applied this principle to develop a method for calculating the stress fields resulting from a V-notch plate. Since this approach can be used to estimate the deformation response of a linear elastic system due to different sources of external stimuli or force, the uncertainty associated with individual components of the system can also be estimated following the same approach. So, for a multi-physics system, it is reasonable to quantify the significant uncertainty from each physics domain in a hierarchical approach to help establish the credibility of the multi-physics system model through a quantitative validation assessment.

Care should be taken when using the superposition principle to ensure that the data from the various physics domains are obtained from the same region of interest, i.e., the exact location of the specimen. It is recommended here that the measurement uncertainty from each physics domain should be superposed following the same approach for combining the response data.

A validation assessment aims to establish whether the level of agreement between the prediction and the measured data from a carefully designed experiment satisfies the specified requirements for the intended use of the model. The assessment requirements, dependent on the model's intended use, will differ between single physics and multi-physics experiments. Thus, the level of agreement for the individual physics domain or components in figure 7 will differ from the coupled physics components due to the additional sources of error arising from multiple physics domains, the interaction effect on the structural integrity, and the system complexity.

The difference between the enhanced process flowchart in figure 7 and the ASME V&V and CEN guides include:

1. The enhanced flowchart addresses more than one physics domain and system loads, unlike the ASME V&V,
2. It only considers using the minimum measurement uncertainty obtained from a calibration experiment described in chapter 5 of this thesis when assessing the quality of the measurement data and assessing how well the simulation output represents its corresponding physical test, and
3. In the enhanced flowchart, the superposition method is recommended to combine the measurement uncertainty from the different physics domains to account for the total uncertainty in the combined physics domain.

3.2. Conclusions

An enhanced validation process has been developed as part of this research to handle multi-physics simulations. The proposed enhanced processes in figure 7 are an extension of the classical flowchart provided in the ASME V&V guide with input from the CEN guide for full-field data. The extended approach recommends deploying the superposition principle to combine response data and measurement uncertainties from different physics domains to provide an approximation for the response of the multi-physics domain where it may be impossible to design validation experiments. The goal of the approach is to build confidence in a model's fitness through a rigorous validation exercise that will help establish the credibility of the coupled phenomena.

Chapter 4

4. Physical and Computational Research Methods

This chapter details the research methods and techniques used in acquiring and processing data presented in this thesis. In the previous chapter (Chapter 3), an enhanced validation approach was proposed to validate multi-physics simulations using quantitative experimental data acquired with the DIC measurement method. The processes in the proposed new flowchart have been demonstrated using a suitable test specimen, in this case, an idealised nuclear fuel cladding tube made from austenitic stainless-steel material and planned, designed and tested validation experiments that capture each physics domain or phenomenon in the flowchart in figure 7. The experimental campaign and modelling efforts are split into three parts: the thermal component, the mechanical components, and the combined thermal and mechanical components (thermo-mechanical experiment). The component as used here implies the computational model and the experiment.

As mentioned earlier, three sets of experiments representing three different phenomena were carefully designed, built, and tested to demonstrate the feasibility of the enhanced processes in the new flowchart. The thermal domain of figure 7 represents a thermal expansion phenomenon, the mechanical domain represents a three-point-bending phenomenon, and the thermo-mechanical domain is a combination of the thermal expansion and three-point-bending phenomena. The experiments described in this research were designed to be within the elastic range or limit to avoid failure or fracture of the test specimen during system loading, as this was not desirable and was out of scope for this work.

The first section of this chapter describes the case study employed for this research. The second and third sections describe the basic theory behind the measurement methods, Digital Image Correlation and full-field infrared thermography, which were used to acquire full-field surface displacement and temperature maps during the experiment. The fourth section, through to the final section, details the thermal, mechanical, and thermo-mechanical experimental and modelling components.

4.1. Case Study

Nuclear fuel materials used in reactors are often exposed to complex thermo-mechanical phenomena during their operation resulting in deformation mechanisms such as creep, swelling, cracking, and pellet-clad-interactions (PCIs). An austenite stainless steel tube was used as the test specimen for this research to represent a nuclear fuel cladding of an AGR reactor. The geometry and material properties of the tube and heating element are listed in tables 2 and 3. The test specimen was subjected to combined simultaneous thermal and mechanical loads to represent the fuel cladding during in-service operation. The cladding is used as an exemplar for this research because the deformation includes multiple physical phenomena.

The cladding is one of the critical safety barriers in fission nuclear reactors as it retains most of the radioactive fission products within its volume [122]. This structure consists of a thin-wall tube housing annular ceramic fuel pellets. Due to the relatively high temperature (650^{O}C) and overpressure (4 MPa) of the CO_2 coolant in the core, the cladding creeps until initial contact with the pellet occurs, resulting in pellet-cladding interactions (PCI) [123].

Table 2: The geometry of the stainless steel tube

Test specimen	316l stainless steel tube
Length (mm)	310
Outer diameter (mm)	25.4
Inner diameter (mm)	22.1
Wall thickness (mm)	1.65
Specimen effective heating length (mm)	300
Quartz lamp (heating element)	Ceramic glass
Length (mm)	357
Diameter (mm)	10
Lighted length (mm)	272
Radial gap between the heating element and the inner diameter of the tube specimen (mm)	12.1
Axial constraint of the tube	Simply supported

Table 3: Temperature-dependent material properties of the specimen, 316l stainless steel tube[12]

Temperature (^{0}C)	20	100	200
Young's modulus, E (GPa)	200	194	186
Poisson's ratio	0.25	0.26	0.29
Mean coefficient of thermal expansion (10^{-6}/K)	16.0	16.5	17
Density (kg/cm^3)	7880		
Thermal conductivity (x10^{-6}/^{o}C)	15		
Melting temperatures (^{0}C)	1375 - 1400		

In other words, as the temperature increases, the thermal expansion of the pellets stretches the cladding longitudinally to accommodate any increase in length and causes the cladding to deform, as illustrated in figure 9. The deformation mechanism allows a close-to-uniform strain along the axial length. During a power ramp, PCI induces significant stresses in the cladding, which can lead to failure. Therefore, the analysis of stresses and strains due to combined temperature and mechanical loads are crucial to assess the structural integrity of the cladding and to ensure safe operations. It is also important to note that the computational analysis of nuclear fuel components is usually a multi-physics undertaking, which involves, at a minimum, coupled heat conduction, thermal, and mechanical deformation.

[12] https://www.bssa.org.uk/topics.php?article=139

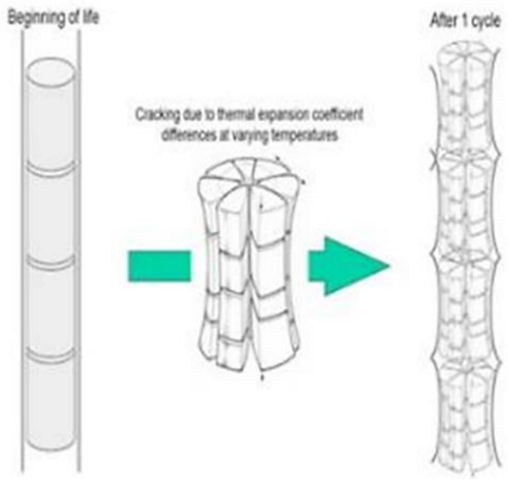

Figure 9: Deformation of a pellet-cad due to variation of temperature and pressure [122]

The experiment campaign for this research was designed to represent the thermal expansion of a nuclear energy fuel cladding due to thermal loads generated by the fuel pellets, the mechanical deformation as a result of the coolant pressure on the cladding, and the combined effect of thermal and mechanical loads of the cladding tube during operation. It is worth noting that the experiments described in this thesis were idealised experiments and did not include the effect of radiation usually experienced in a nuclear reactor.

4.2. Digital Image Correlation Measurement Method

Several non-contact optical full-field techniques exist to measure displacement and strains at elevated temperatures. These techniques include Electronic Speckle Pattern Interferometry [124], laser speckle correlation technique [125], and the Digital Image Correlation (DIC) technique. The DIC technique can be considered the most promising full-field measurement method to be used in industrial settings because it is relatively simple to operate and bypasses the challenges of processing fringe patterns to produce deformation results. In other words, in DIC, the displacements are calculated directly by correlating the digital images captured before and after deformation. In this work, stereoscopic DIC was used to acquire surface displacements because it has the capability to gather full-field information at elevated temperatures, at a wide range of specimen sizes, timescales and loading rates, as well as the capability to measure in and out-of-plane displacements

DIC can be used with either a single camera (2D-DIC) or a pair of cameras (3D-DIC) to capture full-field displacement for planar and curved surfaces, respectively. The former, 2D-DIC, is relatively simple and can be used to capture in-plane deformation. In comparison, 3D-DIC or stereoscopic DIC uses two cameras to capture digital image pairs at each deformation step, allowing calculation of the out-of-plane and in-plane displacement and providing information on the object's curvature through point triangulation. DIC has a typical accuracy in the order of ± 1/100 pixels for in-plane displacement components and ±Z/50000 for out-of-plane displacement components, where Z is the distance from the cameras to the object or specimen [126]. A stereoscopic or 3D-DIC system was used in this research to acquire the surface displacement of the non-planar stainless steel tube during loading. 3D DIC was significant for this research due to the curved geometry of the specimen.

In DIC, deformation information relies on the surface preparation of the specimen, i.e., imaging a speckle pattern on the surface of the specimen before a test load is applied and subsequently correlating each image of the deformed pattern to that of the un-deformed (reference image) pattern. The speckle pattern serves as the deformation carrier. The basic principle of this technique is illustrated in the schematic diagram of figure 10, and Sutton et al. [48] have provided detailed information on the technique.

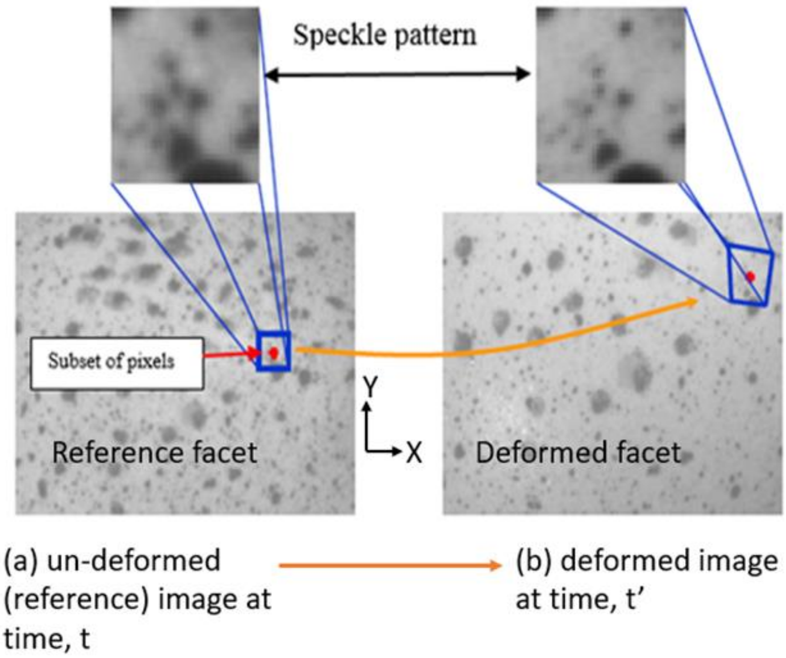

Figure 10: Schematic representation of the DIC principle showing (a) undeformed facet in the reference image is mapped onto (b) the deformed facet in an image from a loaded specimen

Each digital image of the object or specimen is an intensity array that is divided into a square or neighbourhood subset, also called a facet, as illustrated in figure 10. The discrete matrix of the pixel grey level values in each subset forms a unique identification within the object image. The size of these subsets is dependent on the spatial frequency of the speckle pattern imaged on the surface of the object, and the spatial frequency of the speckle pattern is significant to the accuracy of the deformation measurement. The uniqueness of each facet is achieved if the surface has a non-repetitive, isotropic, and has a high contrast pattern. Sutton et al. [127] recommended a process to achieve an optimised subset of uniformly distributed speckles. Prior to loading an object, a reference image of the undeformed specimen is captured. Subsequent images captured during loading are identified as deformed images. Image correlation is performed to correlate the deformed images to the undeformed images by comparing the facets from the reference image to the facets from each of the deformed images using a correlation algorithm based on image matching. During the correlation process, a point *P*(*x*,*y*) within the facet of the reference image is mapped to a point *P**($\tilde{x}$,$\tilde{y}$), using the displacement components, u and v in Equation 4.1, to provide the horizontal and vertical displacements of the centre point of each facet.

$$\tilde{x} = x + u(x, y)$$
$$\tilde{y} = y + v(x. y) \tag{4.1}$$

A higher-order shape function capable of transforming the pixel coordinates in the reference image into coordinates in the deformed images is used to model the shape of the deformed facets. In the work presented in this thesis, the DIC software employed a second-order shape function to map each subset to its distorted shape, defined by the following equations [128]:

$$\begin{aligned} \tilde{x} &= x_0 + u_0 + \frac{\partial u}{\partial x}\Delta x + \frac{\partial u}{\partial x}\Delta \mathrm{y} + \frac{\partial^2 u}{\partial x \partial y}\Delta x \Delta \mathrm{y} \\ \tilde{y} &= y_0 + v_0 + \frac{\partial v}{\partial x}\Delta x + \frac{\partial v}{\partial x}\Delta \mathrm{y} + \frac{\partial^2 v}{\partial x \partial y}\Delta x \Delta \mathrm{y} \end{aligned} \tag{4.2}$$

where (x_0, y_0) and $(\tilde{x}, \tilde{y})$ represents the coordinates of the centre of the facet in the reference and deformed image, respectively, with the in-plane displacements defined by u_0 and v_0. The remaining parameters in the shape function define the surface slopes and distortion. The mapping parameters in Equation 4.2 are determined using a sum of square deviation (SSD) to minimise the difference between the reference and deformed subsets or facets.

Errors can arise in the matching process when the size of the speckle pattern is not unique enough in the defined facet—implying that the facet size is crucial to ensure that the shape function accurately describes the deformation. Interpolating the discrete grey-level values measured with the DIC cameras is essential to achieving sub-pixel accuracy in the facet matching process. A bi-linear interpolation method can be used; although it is computationally efficient, it comes with the cost of generating an increased bias, particularly when processing noisy images [94].

In this thesis, a bi-cubic spline was employed to obtain sub-pixel accuracy of displacement measurements. Whilst this method is computationally expensive, Borner et al. [102] and Sutton et al. [100] work indicated that the bi-cubic spline generates the lowest bias and random error compared to other conventional methods such as bilinear and bi-cubic polynomial interpolation. Sutton [126] stated that performing interpolation with less sophisticated filters such as the bi-cubic spline can result in a bias of approximately 1/40 of a pixel while using an optimised filter will have a bias that is below 1/200 of a pixel. Borner et al. [94] also stated that using an optimised bi-cubic spline filter can result in a bias of around 13 x 10^{-3} noisy images and 1:1 x 10^{3} pixels for noiseless images. DIC measurement technique also relies on the quality of the surface pattern, i.e., the quality of the speckle pattern imaged on the object or specimen is crucial to obtaining good results. Therefore, errors can arise if the pattern is of poor quality. There are practical guides [129]–[132] to generate high-quality speckle patterns, and the generally accepted speckle size is around 3-5 pixels in diameter.

The experimental work presented in this thesis made use of a commercially available DIC system (Q-400 system, Dantec Dynamic GmbH, Ulm, Germany). The system consisted of two Allied Vision firewire cameras 14bits – Guppy Pro F-125 equipped with 1 megapixel Sony 1CX445 CCD sensors. The camera has a maximum frame rate of 31 frames per second at full resolution.

The surface of the tube specimens used in this work was prepared for DIC measurement by applying a high-contrast random pattern to the region of interest, which is essential in the characterisation of facet position and displacement tracking. The speckle patterns were generated by spraying a uniform layer of a commercially available refractory white paint (VHT Flameproof, Cleaveland, Ohio, USA) to the surface of the specimen. This is a high-temperature paint suitable for temperatures of up to 1000°C, and it was employed in this work to prevent debonding of the pattern from the specimen surface during thermal loading. A black version of the same paint was used to create a speckle pattern following the recommendations in [129]–[132] and Lecompte et al. [133]. The scale of the specimen region of interest was considered to determine the creation of the speckle size. A large speckle size requires the use of a large facet or subset that can accommodate around nine uniformly distributed speckles, as recommended by Sutton [126]. However, this compromises spatial resolution. On the other hand, a small speckle size increases the noise level in the results and the risk of aliasing.

In this work, a suitable speckle pattern could not be achieved using the typical spraying method as the curved geometry of the tube specimen made it challenging to generate a good quality pattern. Several attempts were made to achieve an evenly distributed pattern of black paint, as shown in figure 11a. A spray can was initially used, but it proved challenging to obtain evenly distributed speckles due to the curved surface of the specimen and generated speckles that were too small in size with the presence of large spots that were not ideal. A toothbrush using a flicking technique was then employed, and it generated better speckles (figure 11 b) than the previous method using a spray can. Again, this technique also failed to produce good speckles of acceptable size due to the curved surface and small diameter-to-length ratio. Finally, promising results were achieved using a small paintbrush (natural bristle PCB and flux brush, 5 mm diameter) to apply random speckles on the surface of the specimen. The paintbrush bristles were glued together to produce a pointed tip of approximately 1 mm in diameter and was manually used to apply the black paint to the specimen surface in a point-by-point approach.

a

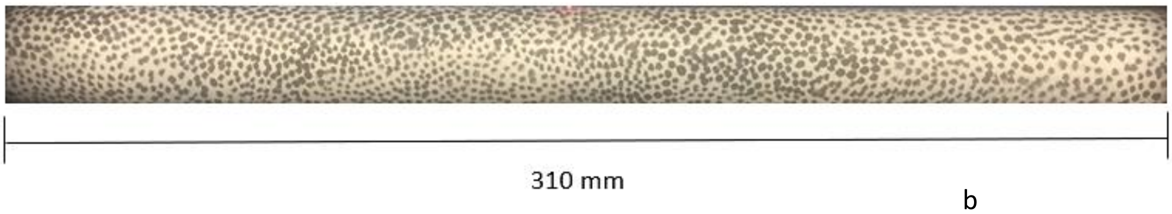

b

Figure 11(a) Picture of initial speckle pattern generated using different approaches, (b)Image of the speckle pattern generated using a bristle paintbrush on the surface of the tube specimen

The most common challenge when performing DIC at elevated temperatures is the increase in black body radiation. Traditionally, DIC methods have been successfully used up to approximately 600^{o}C. Radiation from the test specimen becomes visible when the temperature of the specimen is above 1000K (727^{o}C). This was not a significant challenge for the work presented in this thesis because the experimental temperature was below 600^{o}C. However, the oxidation of the paint used to generate the speckle pattern is a significant challenge when working with elevated temperatures. Most traditional paints degrade at temperatures above 250^{o}C. Researchers have employed sophisticated methodologies to solve this problem at temperatures above 1000^{o}C. Pan et al. [52] fabricated a speckle pattern for high-temperature application (1200^{o}C) by blending black cobalt oxide with a liquid composition of a commercially high-temperature inorganic adhesive to yield a black liquid suitable for their DIC application. Commercially available, temperature-resistant paint has been shown to withstand temperatures of approximately 600^{o}C without significant degradation or debonding of the paint. In this work, a white VHT Flameproof base paint was applied following the direction of the paint manufacturer. The application of this paint was suitable for the test temperature (approximately 200^{o}C) used in the work presented here, and no visible discolouration was observed. The tests reported in this thesis were performed in a ventilated room with an extractor fan to facilitate the mixing of the air around the experimental setup and hence minimise the effect of heat haze.

4.3. Full-field Infrared Thermography

In this thesis, a micro-bolometer with an accuracy of ±2 ^{o}C or ±2% (whichever is greater) was used to capture surface temperatures during the thermal loading. The commercially un-cooled micro-bolometer (TIM 400, MICRO-EPSILON UK, Birkhead, UK) with a 25 x 25 µm focal array sensor had a 382 x 288-pixel resolution and had a maximum framerate of 80 Hz. The setup detects IR radiation across the 7.5 to 13 µm spectral range and has a noise-equivalent temperature difference (NETD) of 0.08K. The microbolometer was placed at approximately 750 mm from the specimen (area of 260 mm x 10 mm). The micro-bolometer device used here is factory calibrated. The range of the temperatures used in this research is within the calibration range of 0-250^{o}C provided by the manufacturer.

Full-field surface temperature maps were acquired by applying a surface emissivity factor of approximately 1. Emissivity is significant to temperature measurements because all objects do not radiate similar energies. For this work, a black matte high-temperature paint was applied to the internal wall of the specimen to enhance its emissivity. It is assumed that the temperature generated by the heat source inside the tube is equivalent to the outer surface temperature detected by the microbolometer. i.e., the thermal gradient in the radial – z-direction is negligible due to the relatively thin thickness (1.65 mm) of the specimen.

4.4. Thermal Component: Experimental Design and Procedures

This section of this thesis introduces and describes the design, build and test of the thermal expansion experiment representing physics domain one of figure 7.

4.4.1. Introduction

The experimental campaign started with the design and test of the thermal component. This work used a stainless-steel tube as the test specimen. The test was designed to create a simplified version of the thermal deformation or thermal expansion phenomenon experienced by the cladding during operating conditions. Nuclear fuel pellets thermally expand upon heating in a reactor. The thermal expansion of the pellets contributes to pellet-clad-mechanical-interactions (PCMI), which can lead to failure under operating conditions. In an as-manufactured fuel rod, there exists a roughly axisymmetric gap between the outer radius of the pellet and the inner radius of the cladding [134]. This ideal gap thickness is reduced during a power ramp as the cladding extends longitudinally until the interface between the pellet and clad is closed. The extension or axial elongation of the cladding is driven solely by the thermal expansion of the fuel pellets. It is essential to accurately predict the thermal expansion of the fuel rod to optimise designs and prevent failure of the structural integrity of the fuel during operation. Therefore, understanding the thermal expansion is significant to determining the fuel performance during reactor operation.

As previously mentioned, in this thermal experiment, a stainless steel tube made from 316L was used to represent the fuel cladding. The aim of the experiment was to mimic the loading configuration of the cladding in a reactor. 316l stainless steel grade possesses high strength at elevated temperatures with relatively high toughness. Its favourable material properties render 316L stainless-steel ideal material for various applications in industries and nuclear engineering applications. Stainless steel of grade 316L has been commonly used to fabricate reactor vessel components [135], [136] and is thought to be an ideal test case for this research.

In this thermal experiment, different loading configurations and heating methods were considered in other to mimic the effect of a fuel pellet on the cladding. Induction heating and infrared radiator heating configurations employed in literature [53] [52] were considered, respectively. These heating configurations and systems proved challenging for application to the thermal experimental setup mainly due to the geometry of the tube used in this work and could not be used to mimic the configuration of a fuel pellet within a cladding. It was also desired in this research to have the thermal load applied in the tube, as this represents the effect of the pellet loads on the cladding and provides a uniform heating configuration. Moreso, having the tube heated externally may also result in an additional challenge for the measurement system, i.e., the DIC cameras will be affected by the illumination from the heating system, which would result in making the experiment more complicated. For the thermal experiment described in this thesis, a halogen quartz lamp described in section 4.4.3 was used to provide the thermal loads. Researchers have previously applied this heating device to their studies. For example, in the literature [54], the authors used a halogen quartz lamp to thermally load Hastelloy–X plates in different configurations and reported good temperature distribution. One of the advantages of using the halogen quartz lamp for this research includes the ability to control with ease the power input to the test system, and the geometry of the lamp is such that it can be easily mounted internally in the stainless-steel tube used as the test case.

In the thermal analysis, the stainless-steel tube was subjected to elevated temperature loads from ambient temperature to a maximum of 200^{o}C, using the heating element described in section 4.4.3. A change in temperature (ΔT) in a cylinder or tube induces thermal expansion or contraction, which causes a change in length (ΔL) and the circumference (ΔC) of the cylinder. This change in the material's dimension is directly proportional to the change in temperature (ΔT). If the material is unconstrained, i.e., free to expand, little or no stress will be generated. When the expansion is prevented by a surrounding material or by an external constraint, it will result in thermal stress. The magnitude of the stress is such that if applied as an external load, it would produce a strain that is equal to the prevented expansion.

4.4.2. Thermal Expansion Experimental Design and Instrumentations

The experimental setup of a thermally induced deformation of the 316l stainless steel tube is illustrated in the schematic diagram in figure 12. This was the first step to achieving a combined (coupled) thermal and mechanical validation experiment.

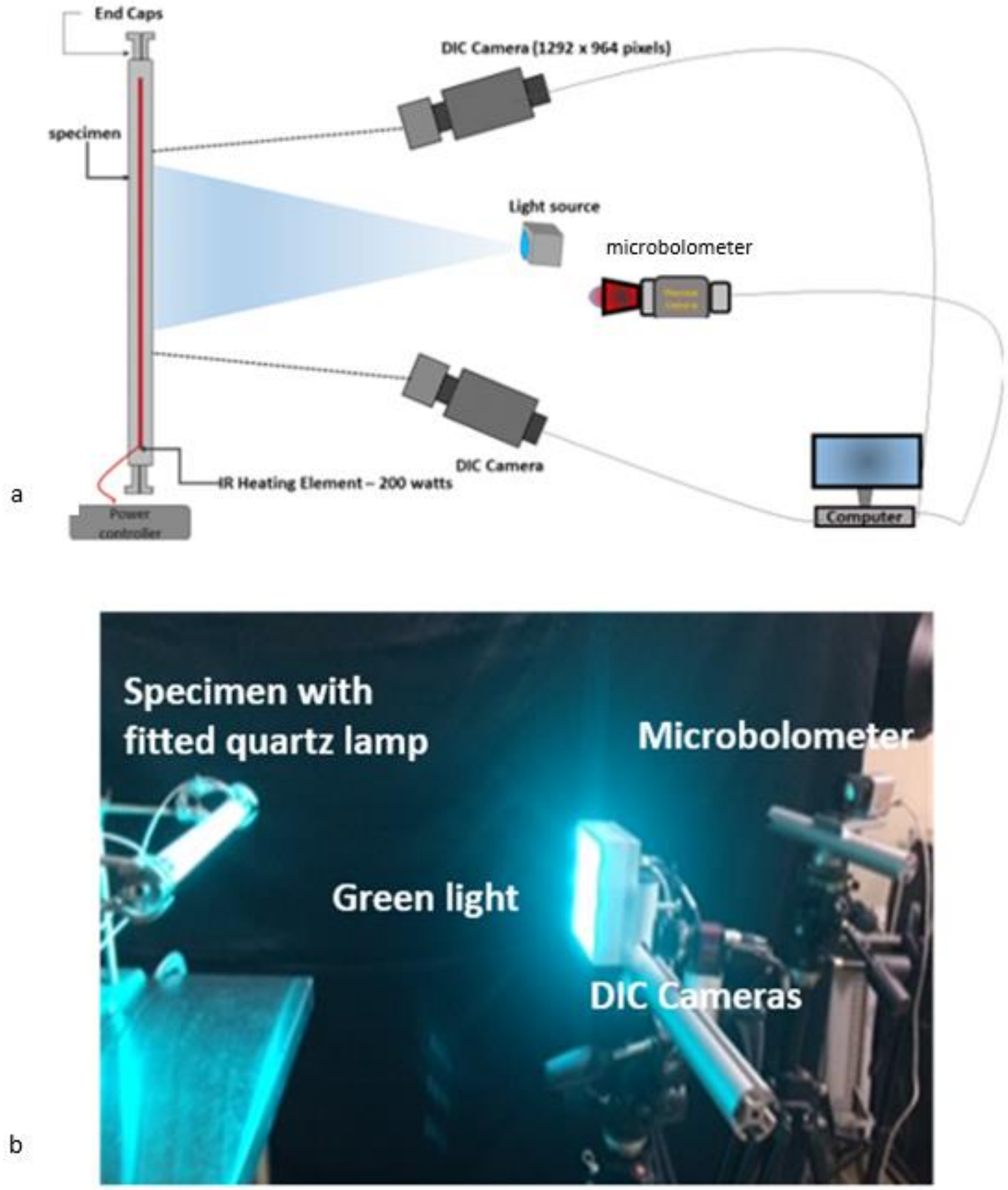

Figure 12: Plain view (a) of the thermal experiment setup showing the tube subjected to elevated temperature loads, (b) is a photograph of the physical rig

The experimental setup illustrated in figure 12 consists of four key elements: 1) the test specimen, 2) a DIC system consisting of a pair of CCD cameras with a green light to measure full-field displacement images, 3) a microbolometer (thermal imager) to measure full-field temperature maps, and 4) a thermal loading system – a quartz lamp (heating element). Descriptions of the DIC measurement system and the full-field infrared thermography has been provided in sections 4.2 and 4.3 of this thesis, respectively.

4.4.3. Heating Element (Quartz lamp)

A quartz lamp was used to heat the tube specimen to elevated temperatures to a maximum of approximately 200^{o}C from room temperature. This heating method was chosen for the work because of its ease of use and control; it is relatively cost-effective and replaceable; the power output can be easily controlled to create different temperature inputs into the system. More significantly, the shape and size of the lamp make it suitable for the thermal experiment design as it can be fitted inside the inner diameter of the tube to mimic the configuration of the fuel pellets and cladding. In other words, the lamp acts as the fuel pellet to provide internal thermal load in the context of this work.

The heating element (QIR 240 1000 VZD, Ushio, Steinhoring, Germany) had an initial power output of 1kW. The power output was limited to 200 Watts for the thermal experiment to generate temperatures within the elastic range of the specimen. The heating element was connected to a control box (potentiometer) integrated into the experimental setup to control the power input into the system.

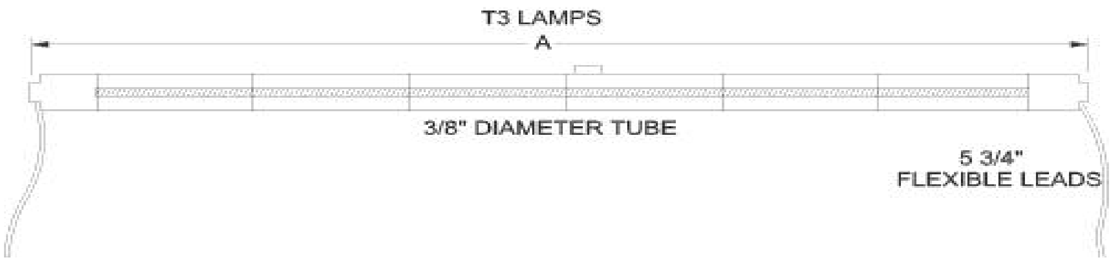

Figure 13: Schematic diagram of the quartz halogen lamp used for this research

4.4.4. Experimental Procedure

In this work, the test specimen or tube was simply supported by specially designed end-caps shown in figure 14 and made from mild steel to allow some degree of thermal expansion in the axial, transverse, and radial directions.

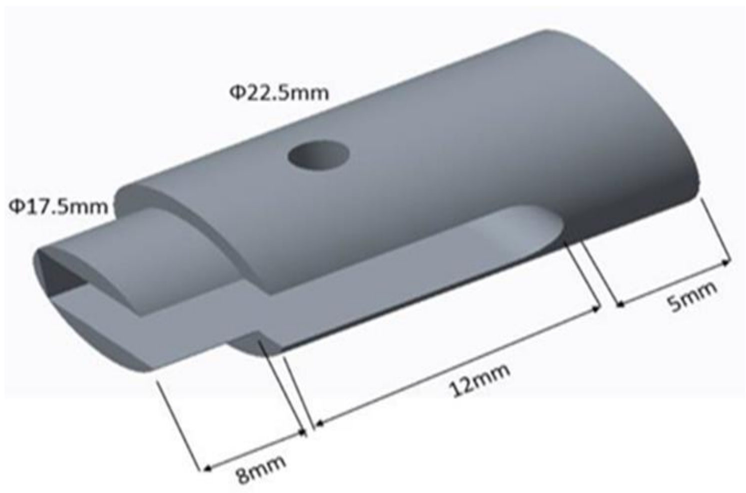

Figure 14: CAD diagram of the end-cap used for the thermal experiment

The end-caps were designed in such a way as to provide a snug-fit with the tube whilst also housing the ends of the heating element. It was also designed to hold the lamp centrally inside the tube to allow radial uniform heating, and the ends of the end-caps were supported in the horizontal plane with two clamps, one on each side of the tube. Careful consideration was given to investigating appropriate materials for the end-caps. The same material used for the tube, 316L stainless steel, was initially considered, but this gives rise to a similar rate of expansion due to the thermal loading of both the end-caps and the tube and could have created a permanent bond during the test. Instead, mild steel was selected as the material for the end-caps because it has a lower thermal expansion coefficient than stainless steel and a higher melting point. Therefore, when the tube is subjected to elevated temperatures, it was expected that the end-caps would not expand at the same rate as the tube and would prevent the formation of a permanent bond between the tube and the end-caps.

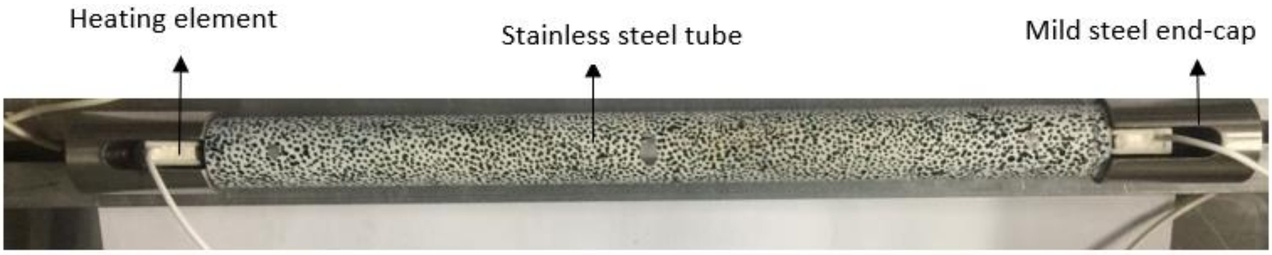

Figure 15: Photograph of the specimen tube with the fitted end-caps made from mild steel used for the experiment

In the thermal analysis presented here, the specimen was subjected to a thermal load from ambient temperature to a maximum temperature of 200^{0}C. The longitudinal (axial) and circumferential surface displacement fields were measured with a commercially-available 3D DIC system described in section 4.2 in this thesis, as the specimen or tube is not planar, while the full-field temperature maps were acquired using a microbolometer described in the section 4.3. A reference image was captured at room temperature in the absence of thermal load, and further images at increments of 25^{0}C up to a maximum temperature of 200^{0}C.

Six repetitions were performed under the same experimental conditions for each temperature increment of 25^{0}C. i.e., six surface displacements at temperatures of 50^{0}C, 75^{0}C, 100^{0}C, 125^{0}C. 150^{0}C, 175^{0}C, and 200^{0}C were captured to estimate the variability of the results and to increase the accuracy of the estimated mean results, which also built confidence in the results generated from the experiment. The thermal analysis served as the first experiment designed and tested as part of a planned coupled thermal-mechanical experimental campaign.

4.5. Mechanical Component: Experimental and Procedure

4.5.1. Introduction

This section of the thesis describes the mechanical experimental design and test performed as progress to achieve a combined or coupled thermal-mechanical experiment.

The mechanical experiment served as the second part of the experimental campaign and represented the physics domain two or phenomenon in figure 7. The mechanical experiment was aimed to represent the mechanical forces exerted on the fuel cladding during in-service operation. To recap, the fuel cladding during in-service operations undergoes different system loads that occur simultaneously, including thermal loads, radiation, fluid dynamics, mechanical loads and combinations of one or more system loads. In the thermal experiment, a halogen quartz lamp was used to provide the thermal loads on the tube and represent the effect of the fuel pellet in the clad, as discussed in section 4.4. The mechanical test was aimed to idealise the effect of the coolant pressure on a fuel cladding. As previously mentioned in section 4.1, the temperature in combination with the coolant (water or gas) can exert pressure on the cladding and result in the creep behaviour of the cladding. The second phase of the experimental campaign in this research was aimed at designing an idealised experiment that represents the effect of the coolant pressure on the cladding. A few design configurations were considered, including the use of hydrostatic fluid pressure and vibration as the sources of the mechanical load. The former involves an additional level of complexity to the design and has a significant safety impact, as the fluid can cause a hazard in the laboratory environment when in contact with the electrical parts of the heating element from the thermal analysis. It is worth noting that for this work, it was important that the system loads and configuration from each physics domain are maintained in the combined thermal and mechanical physics experiment. Therefore, the application of fluid pressure to the tube would likely alter the temperature distribution from the thermal experiment, damage the heating element or halogen lamp, and also can leak out and results in environmental hazards or accidents. On the other hand, the use of vibration would result in a dynamic experiment which was out of scope for this research. After careful consideration, it was determined that a bending test was sufficient to idealise the mechanical loads exerted by the coolant on the cladding and for the simplicity of the experiment.

A custom three-point bending test was designed to capture the mechanical domain or phenomenon in this thesis. Bending tests have been extensively used in the field of engineering [137]–[139], and to investigate the mechanical behaviour of Circular Hollow Structures (CHS) and tubes used in water supply networks [140] [141].

In a standard three-point bending test, the specimen under test is a simply supported beam that is loaded in a three-point configuration and includes two supports and a loading pin positioned at the middle of the specimen length (span length to depth ratio). The mechanical rig designed as part of this research employed some of the working principles of a universal testing machine for bend tests, following the ASTM test standard for Ductile materials (E8/E8M and E290). The stainless-steel tube used as the test specimen was desired to remain within the elastic domain during the test. Therefore, a preliminary bend test was performed in a universal Instron machine to determine the elastic loading range used in the mechanical test. Figure 16 shows the picture of the Instron machine used to perform the preliminary test and the force/deflection results obtained from the test.

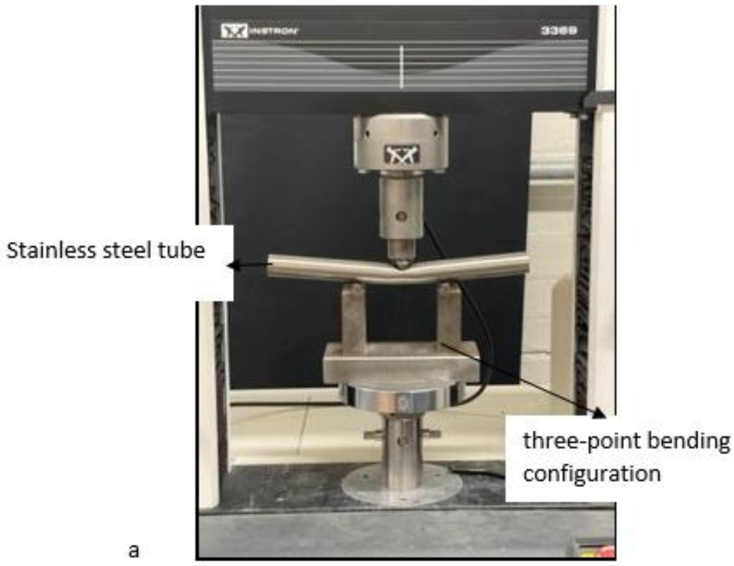

a

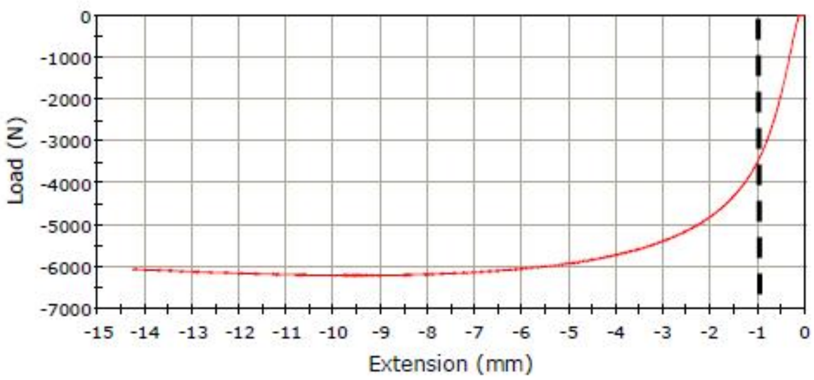

b

Figure 16: (a) Picture of the universal bending rig used to perform the preliminary three-point bending test to determine the elastic loading range and (b) graphical representation of the load/deflection or extension results at increasing loads from 0 to 6000 Newtons

The force versus extension graphical result in figure 16 shows the mechanical behaviour of the stainless-steel tube when subjected to bending loads and was used to determine the loading range for the mechanical test. The result shows that the perfectly elastic region is between 0 to 2500 newtons. For this research, 400 newtons was employed as the bending load, which was at the lower end of the elastic region depicted by the black dotted line in figure 16. From the preliminary bending experiment, 400 newtons loads would result in a displacement of the tube of approximately 0.3 mm. At this displacement, the tube would still retain its structural integrity. The tests (thermal, mechanical and thermomechanical tests) were performed remotely in an environment chamber as a result of safety issues, and as such, a stand-alone rig was designed as part of this research.

In the mechanical experiment presented here, the tube was subjected to a bending load in a 3-point bending configuration. Surface longitudinal (axial) and circumferential displacement fields were acquired with a pair of stereoscopic DIC cameras from a pre-defined region of interest similar to the thermal experiment.

4.5.2. Mechanical Design and Instrumentations

A servo-electric controlled bending rig with a loading capacity of 2.5kN was designed and tested as part of this research. The test rig was designed with the basic principles of a universal testing machine, which comprises two main parts – the loading unit and the control unit. The configuration of the specimen and the exertion of the load are held in the loading unit, while the variation in the application of the load and corresponding results are obtained from the control unit. The three-point bending test rig in this research has a support span length of 260 mm and was designed to allow both load and displacement controls. A linear magnetic encoder and a laser displacement sensor were integrated into the experimental setup as control mechanisms to monitor the vertical displacement of the translating screw jack and the test specimen, respectively. The loading frame was carefully designed and set up to be rigid and to prevent rotations during loading. The rig stiffness was crucial and relevant to the measured deformation. Disregarding the stiffness could result in measurement error.

In this work, the rig loading frame made from mild steel was rigidly attached to a stainless-steel workbench with zero clearance and had a dimension of 500mm (height) by 480mm (width), as shown in figure 17. The loading screw jack was firmly attached to the bottom base of the rigid frame and the workbench to prevent rotation during specimen loading. It is important to note that the test performed in this thesis was for the primary aim of generating quality and quantitative data to demonstrate the validation strategy proposed in Chapter 3 of this thesis.

The key components of the mechanical rig, as illustrated in the diagram of figure 17 and 18, include:

- A mini cubic translating screw jack
- High-torque encoder DC servo motor and driver
- Load cell
- A linear incremental magnetic encoder system
- Laser triangulation displacement sensor
- Load and reaction pins

The subsequent sections describe the functionality of each of the key components listed above.

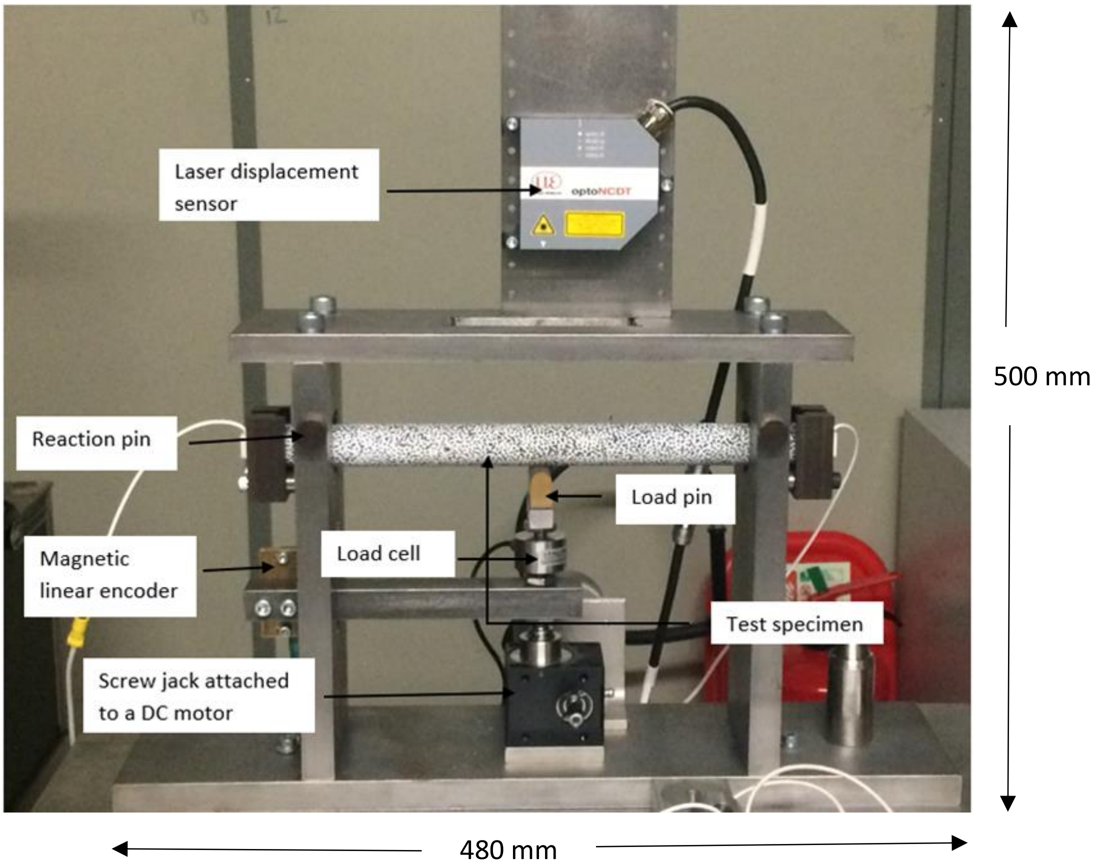

Figure 17: Picture of the three-point bending rig with the associated components

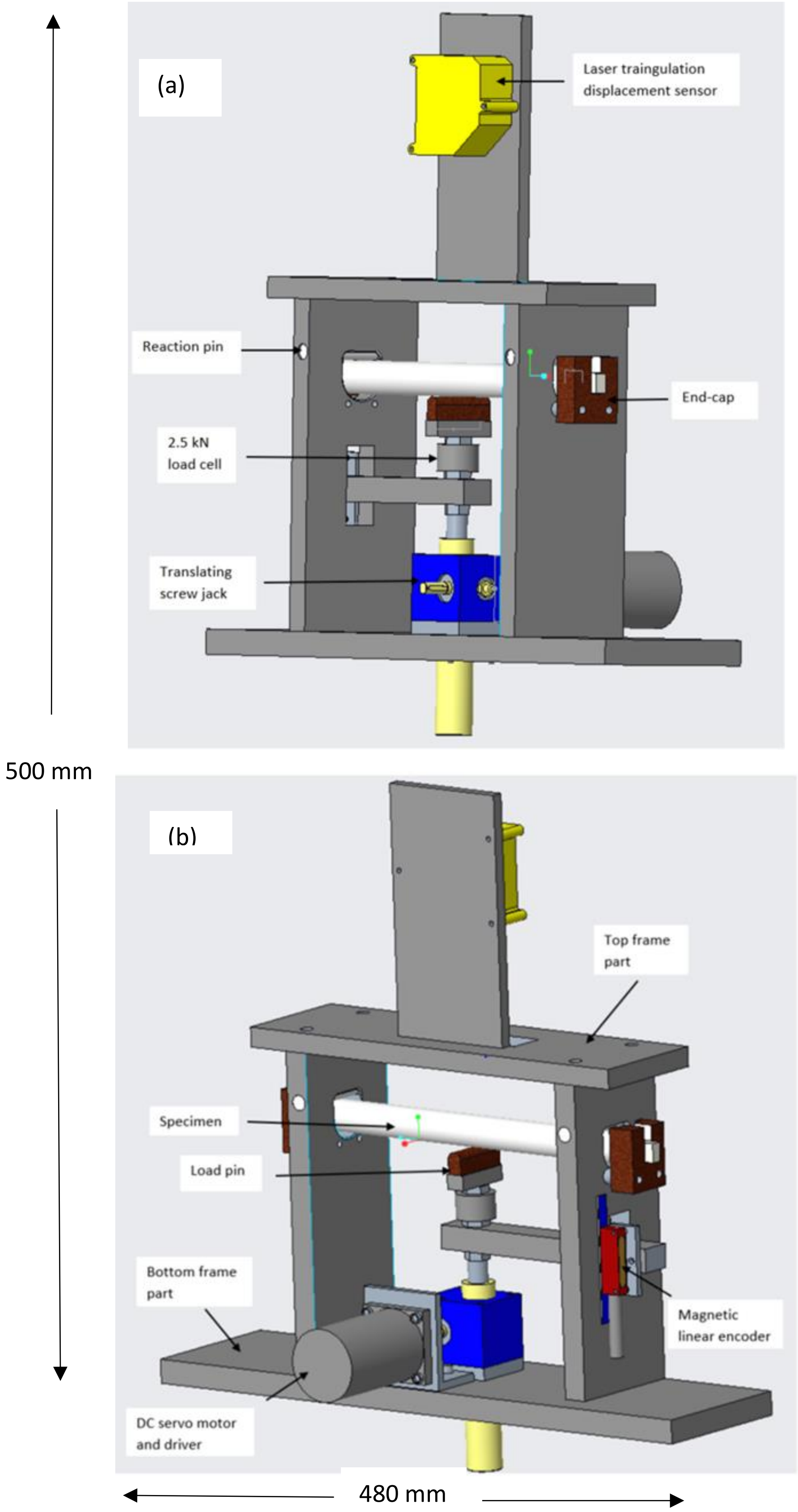

Figure 18: CAD diagrams showing the front view (a) and the back view (b) of the three-point bending rig with the associated components

4.5.2.1. Mini Cubic Screw Jack and DC Servo Motor and Drive

A translating mini screw jack (Kelston Actuation, UK) was used as the load/force generator for this project. The key components of the screw jack include a gear housing, trapezoidal lifting screw, worm screw and worm gear.

The screw jack (figure 19a) was connected to the high torque DC servo motor (figure 19b) through its worm screw and gear interface, as shown in figure 20, to provide rotational movement. In other words, the rotation of the worm shaft causes the worm gear to rotate and results in friction forces acting on the screw thread to enable movement or extraction of the screw. The DC servo motor (Rhino Motion Controls, USA) converts rotary motion into linear motion.

In the work presented in this thesis, the screw jack has a worm gear ratio of 16:1, while the motor has a gear ratio of 10:1 and generates 1800 steps per rotation, producing translation output in the order of 10^{-6} mm per second. This micron displacement of the screw jack was desired for this project to control how much the specimen is displaced under bending load.

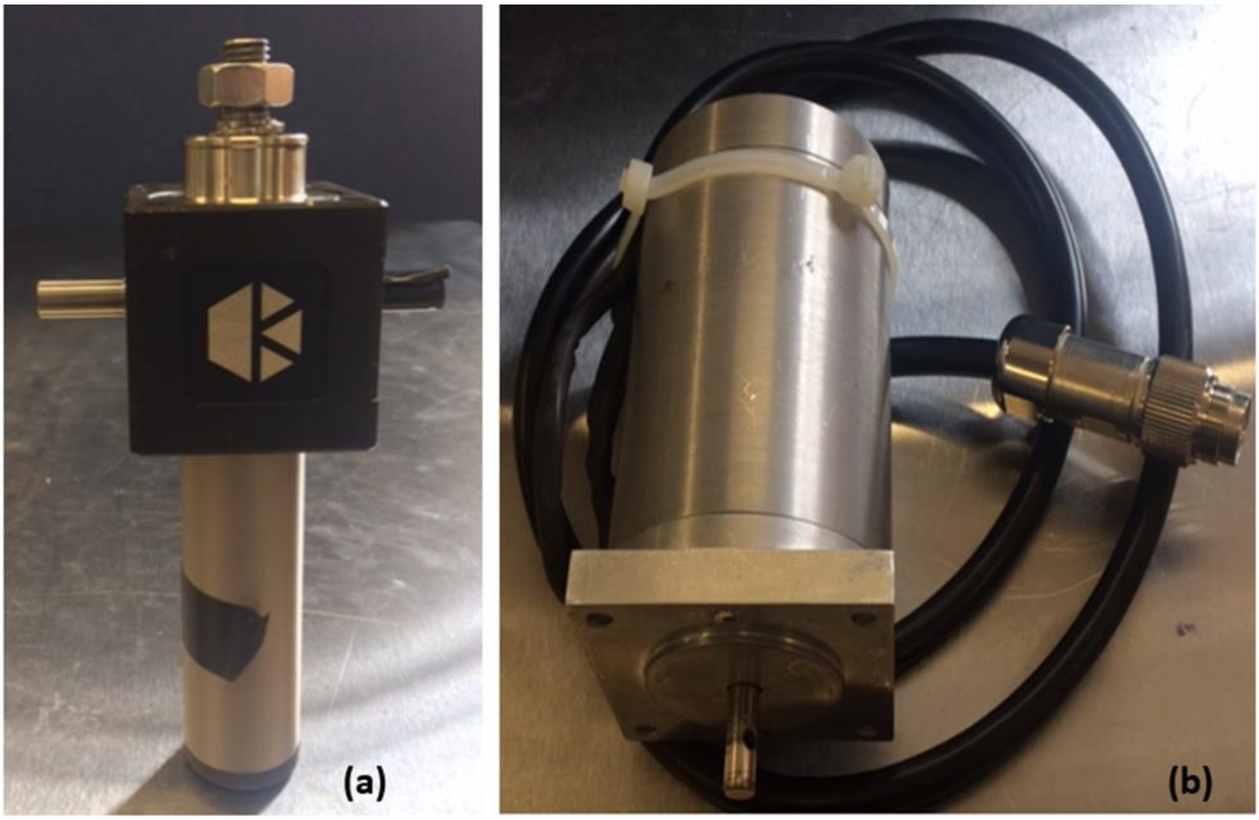

Figure 19: Translating micro screw jack with a capacity of 2.5kN (a) and the high torque DC servo motor and driver (b)

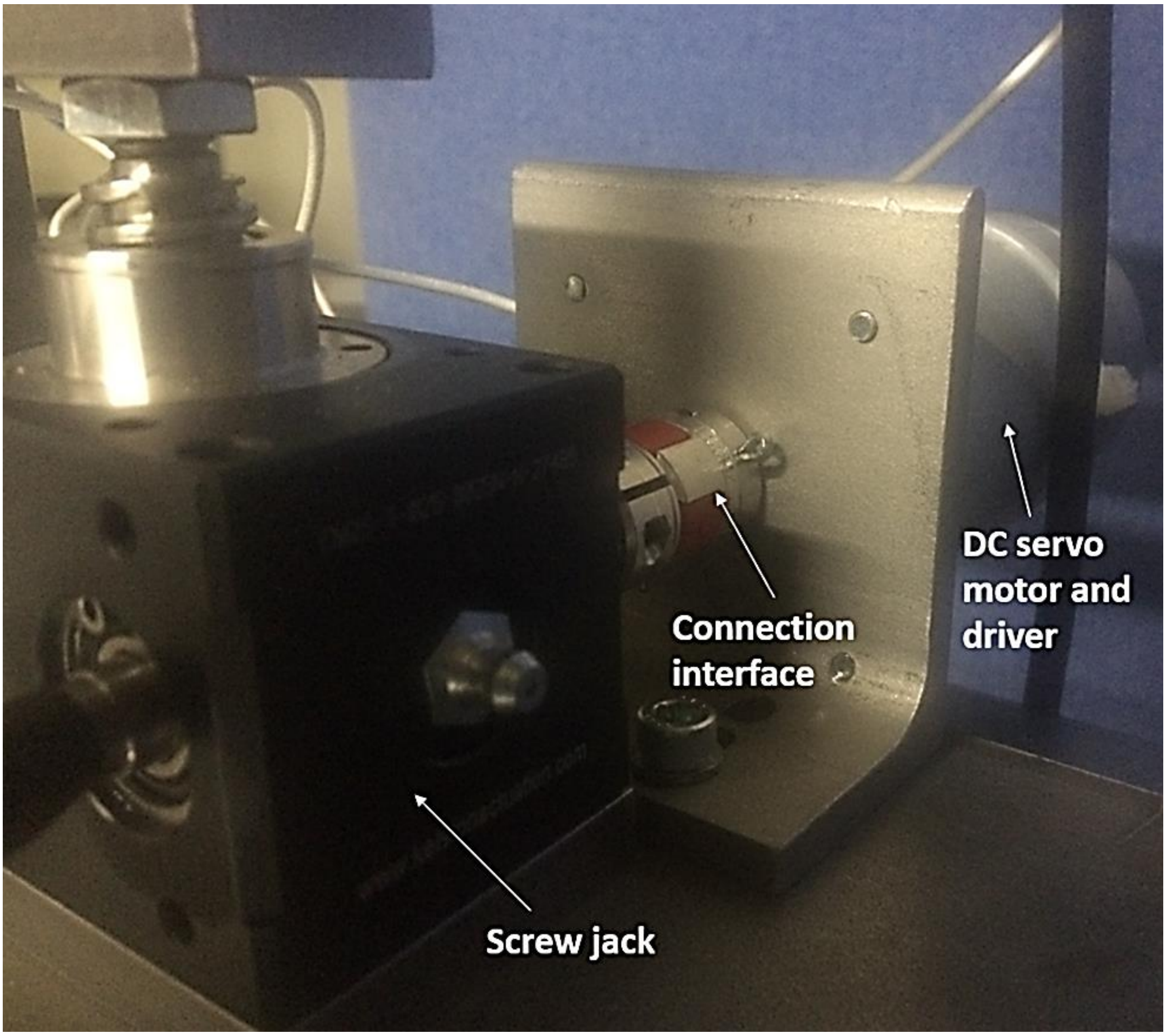

Figure 20: Photograph of the translating screw jack connected through the worm screw to the DC servo motor and drive

4.5.2.2. Load Cell

A calibrated tensile and compression load cell (Richmond Industries Ltd, UK) with a 5kN capacity and operating temperature of 70^{o}C was used for this project to monitor and acquire the force applied to the specimen through the loading pin during the bend test, and it forms part of the loading unit of the rig. The load cell was connected to the shaft of the screw jack and to the load pin, as shown in figure 21, and interfaced with an Arduino through a 24-bit analogue-to-digital converter that converted its output.

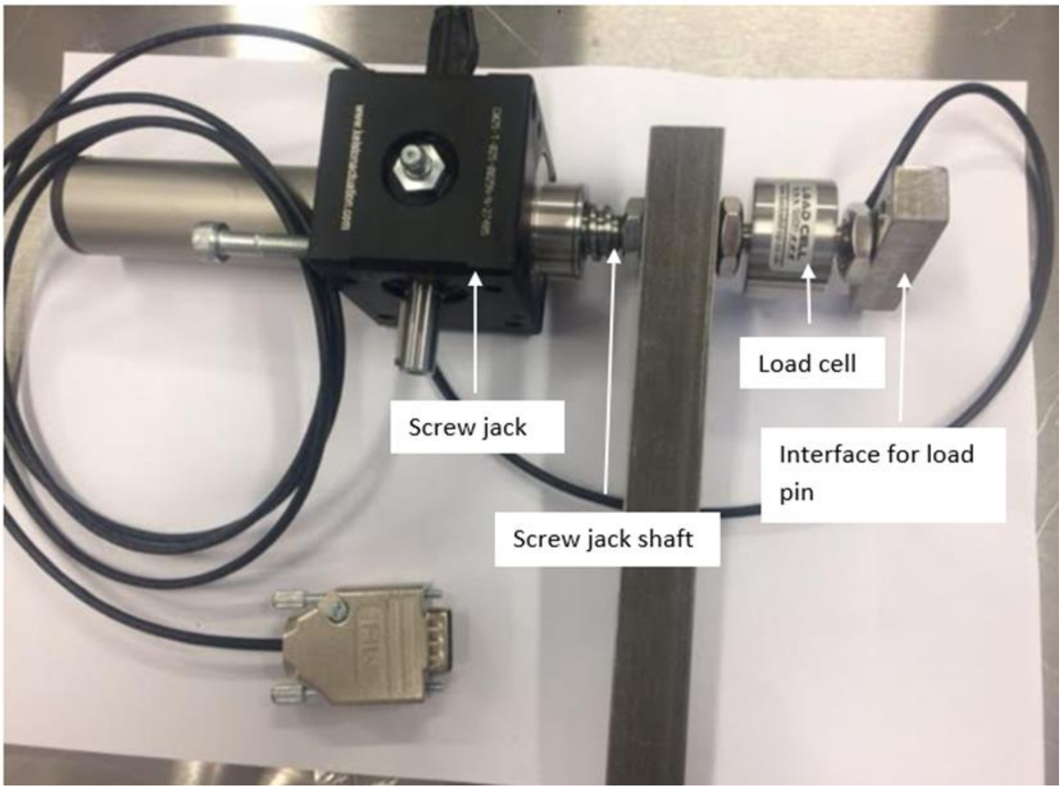

Figure 21: Photograph of the load cell connected to the screw jack and the loading pin interface

4.5.2.3. The Linear Magnetic Encoder System

A linear encoder (RS Component Ltd, UK), a sensor transducer paired with a tape scale (micron-scale), was integrated into the mechanical rig setup to encode the relative position of the screw jack during the application of loads. The encoder relies on three main components for operation: a read head, a sensor, and a magnetic tape. The sensor detects a change in the magnetic field as the read head moves upward and downward. In other words, the sensor detects signals produced by the magnetic code on the tape scale to provide exact linear position information of the read head.

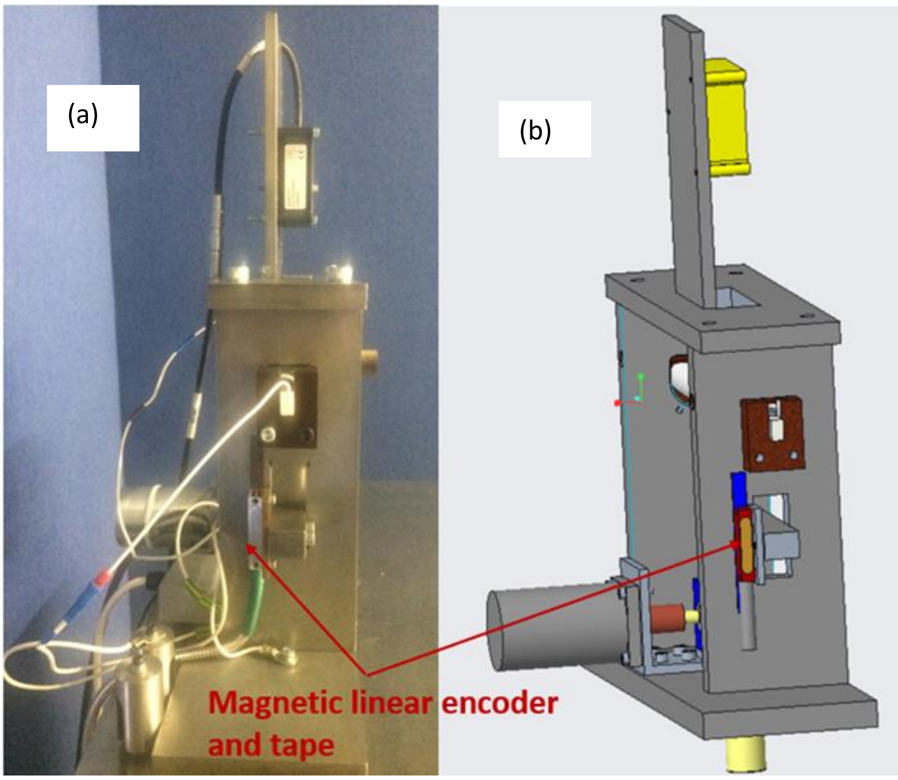

Figure 22: Photograph (a) and CAD diagram (b) of the mechanical rig showing the attachment of the magnetic linear encoder connected through a thin steel plate to the screw jack

In this work, the magnetic linear encoder was attached to a thin steel plate connected to the translation screw jack, as shown in figure 22, to measure incremental motion produced by the screw jack. There are two types of encoders magnetic and optical encoders. A magnetic encoder was chosen for this work because of its robustness and ease of use. It is also insensitive to shocks and vibrations as well as contamination, such as dirt, dust, liquids, and grease.

4.5.2.4. The Laser Triangulation Displacement Sensor

A laser triangulation displacement sensor (optoNCDT 1750, Micro-Epsilon, UK) was integrated into the mechanical rig setup. It was positioned centrally above the tube specimen to measure the transverse displacement of the tube during a mechanical load.

The laser displacement sensor operated on the basic principle that when a beam is projected onto the specimen, in this case, the stainless-steel tube part of the beam is reflected via focusing optics onto a CMOS detector. The detector sends a signal which is utilized to measure the relative distance to the specimen and make the data available through a digital output for processing.

Figure 23:The optoNCDT 1750 laser triangulation displacement sensor integrated into the mechanical rig

In the work reported here, the laser displacement sensor was mounted on the top part of the rig and held in a transverse plane with a mild steel plate perpendicular to the loading point, as shown in figure 23. The sensor has a measuring range of 100 mm, linearity of 60 µm, repeatability of 4 µm, and a measuring rate of 0.3 to 7.5 kHz.

The transverse displacement data acquired with the laser sensor from the specimen under bending load was used to monitor the displacement of the specimen and serve as the basis for constitutive modelling.

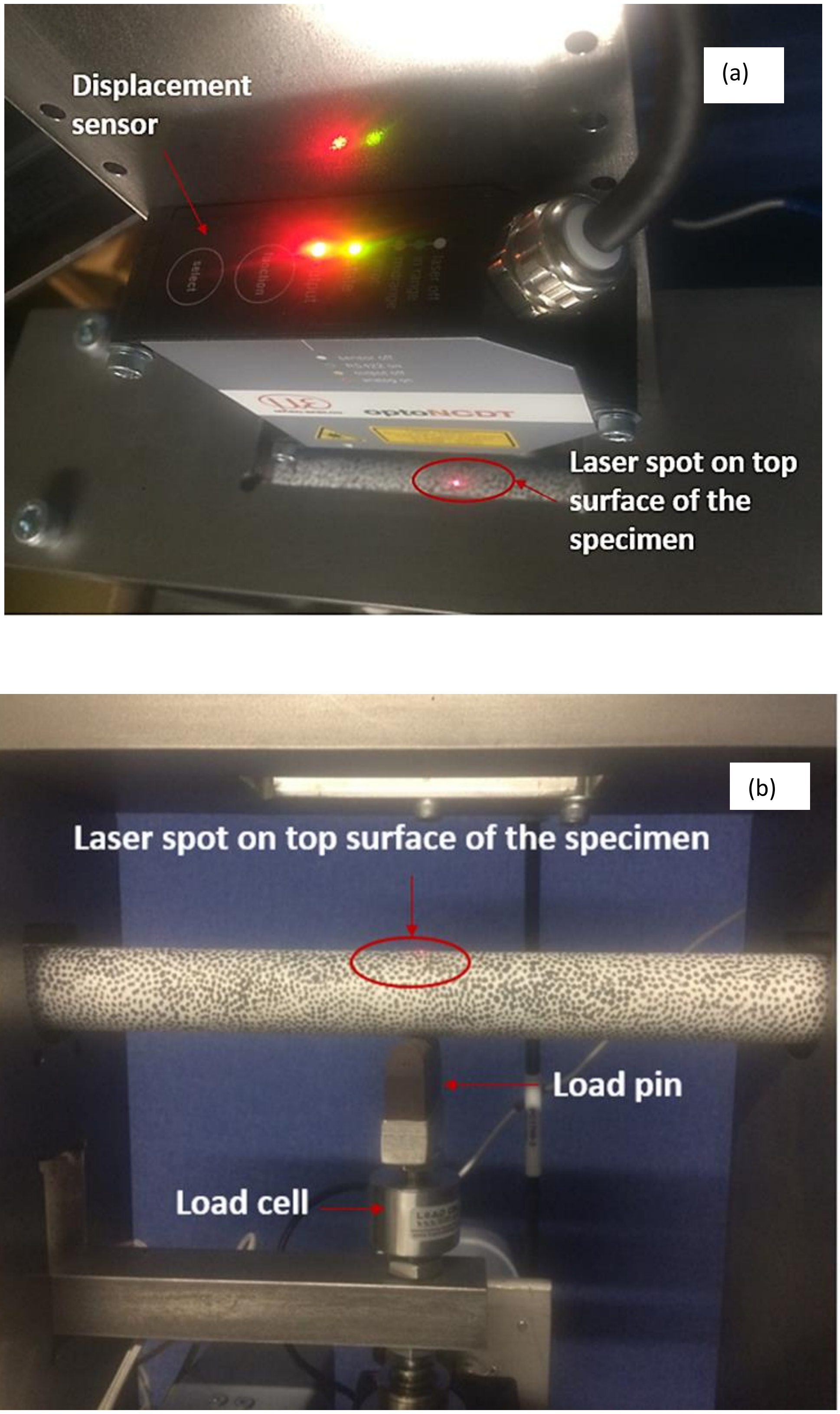

Figure 24: Photographs of the rig showing the position of the laser displacement sensor (a) and the measurement spot of the laser on the specimen (b)

4.5.2.5. The Load and Reaction Pins

A three-point bend test relies on the methods of fixtures used during the test. A three-point bending test is performed by supporting the test specimen near each end with pins or rollers having the appropriate radii as recommended by the ASTM test standard and depending on the application. The radii, sizes, and materials of the load pin and support or reaction pins are significant for this test. It is recommended in [142] that the surface of the loading and support pins or rollers should be hard enough to resist plastic deformation and wear for the load applied during a test. In this work, the three-point fixtures and configuration followed the designation described by the ASTM standard test method (E190/E290 of bend testing of material for ductility). The load and reaction pins in figure 23 were manufactured from a laminate material commonly known as Tufnol 6G/92, a polyimide glass fabric laminate. This material was chosen primarily for its mechanical strength (cross breaking strength of 570 MPa = 570newtons/mm) and insulation properties at elevated temperatures (up to 250^{o}C), which is suitable for the experiment described in this thesis. This material was mainly desired for this work because of its thermal insulation properties and strength, which is crucial for the combined thermal and mechanical experiment.

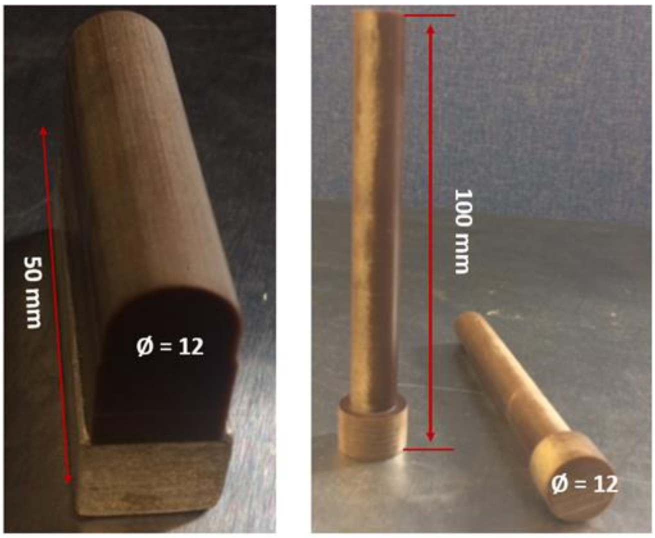

Figure 25: Photographs of the loading and reaction pins with associated dimensions used as part of the fixtures for the three-point-bending test

4.5.3. Experimental Procedure

In this thesis, the test specimen, 316L austenitic stainless-steel tube, was loaded mechanically at a constant force of 400 Newtons and a rate of 6N/second in a three-point bending configuration, as illustrated in Figure 26. A support span of 260 mm was used for this test. It was desired that the specimen remains within its elastic domain during the test. Therefore, preliminary tests detailed in section 4.5.1 were performed to determine the required elastic load to be applied during the test.

This experiment was performed under a hybrid load and displacement control, as illustrated in figure 27. The system was initially set to displacement control as the first step to establish contact between the loading pin and the specimen. This minimised the effect of rigid body (idealized solid, in which the distance between any two internal points stays the same as the body moves around) motion during loading and enabled the remote operation of the system. Once contact had been established, the system was switched to load control. A constant load of 400 Newtons was applied to the mid-span of the specimen to generate a displacement response. A pre-load load of approximately 30 Newtons was recorded during the system setup and was accounted for in the finite element model. The test operating process is depicted in the flowchart in figure 26.

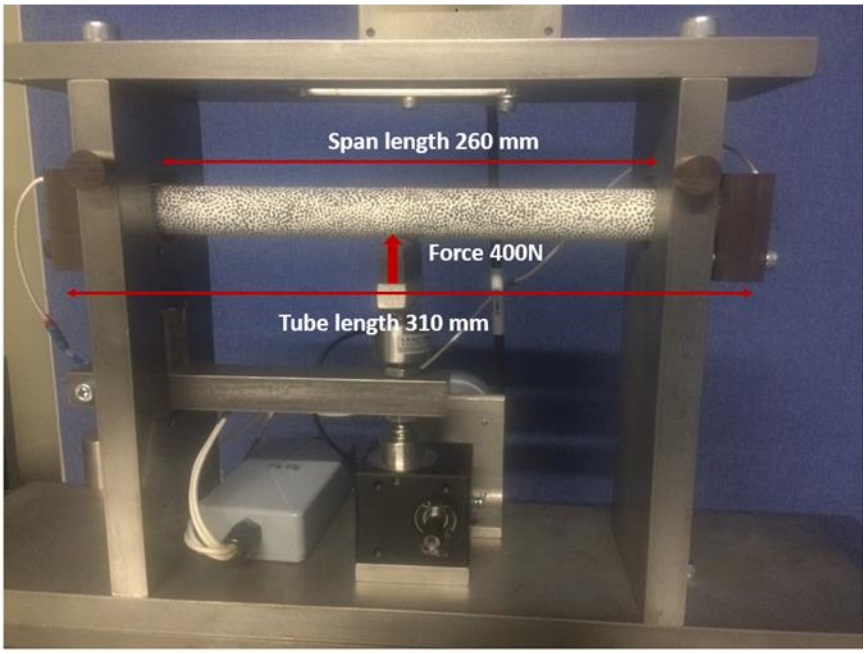

Figure 26: The mechanical experimental setup showing the three-point-bending configuration and the span length

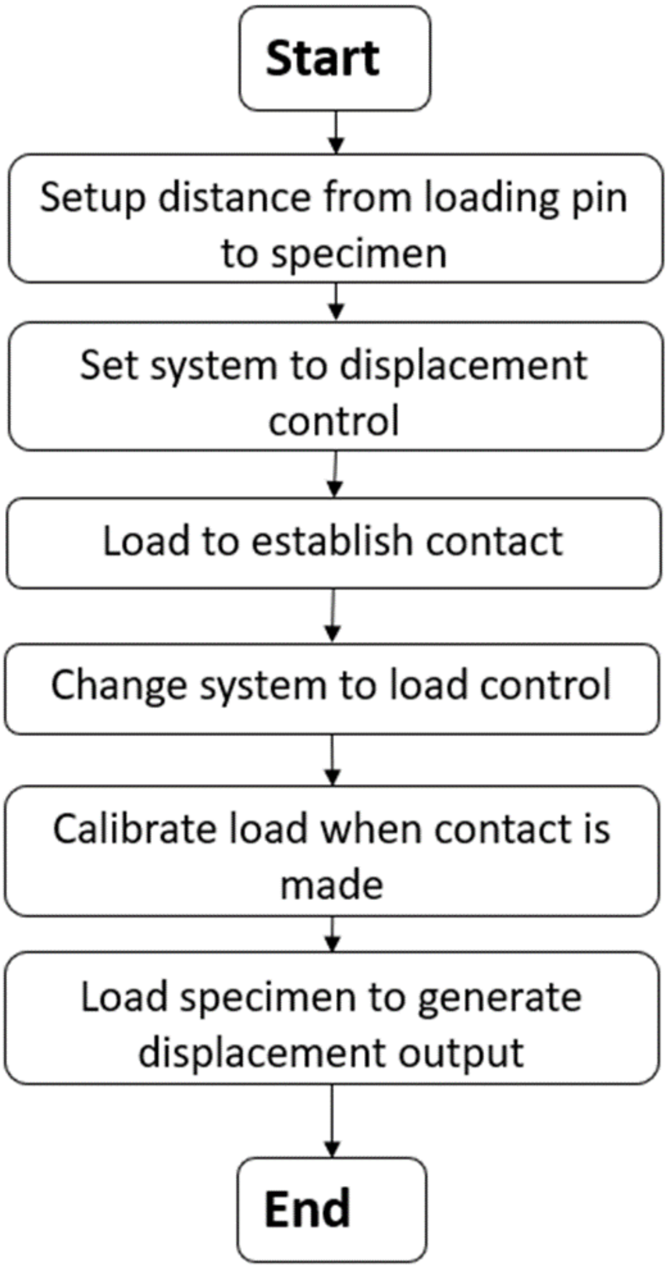

Figure 27: The process flowchart showing the operating process of the mechanical rig under a hybrid displacement and load control

A reference image of the undeformed specimen was captured once contact was established between the loading pin and the tube. Subsequent images of the specimen were acquired at a constant bending load of 400 Newtons, which was applied to the mid-span of the tube (260/2 mm). Full-field in-plane displacement of the specimen was acquired with a pair of stereoscopic DIC cameras fitted with a set of 10 mm lenses (described in section 4.2 of this thesis) adjusted to an f-stop of 1.5. This setup resulted in a spatial resolution of 1mm/pixel.

The speed and movement of the DC stepper motor and screw jack were of the magnitude of microns to allow control of the applied load and displacement and were remotely controlled with an Arduino and LabView program. Figure 28 shows the experimental setup and the DIC displacement system, which was positioned at 750 mm distance from the surface of the specimen. The point deflection of the specimen during loading and the displacement of the DC-powered screw jack was recorded with the laser displacement sensor and the linear magnetic encoder, respectively.

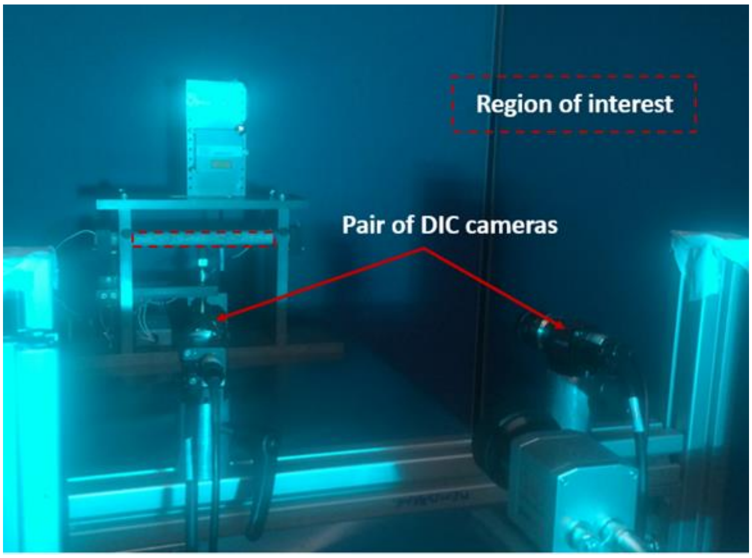

Figure 28: Photograph of the complete system setup and the measurement system, DIC cameras

The images captured and the displacement calculations were performed using Istra 4D software supplied with the DIC system. Image correlation was performed with facets of 17 x 17 pixels with a grid spacing of 4 pixels.

The next section of this thesis details the extension of the mechanical experiment to include the thermal component described in section 4.4 of this thesis.

4.6. The Combined Thermal and Mechanical Components: Experimental Design and Procedure

4.6.1. Introduction

This section details the combined thermal and mechanical (thermo-mechanical) experimental design and procedure, which is the final phase of this research's experimental campaign, and represents physics domain 3 in figure 7. The principle of superposition of several loads acting on a system was investigated and employed during the design of the thermo-mechanical experiment reported in this thesis.

In practice, structural members of an engineering system are often under the action of several loads and physics, especially for complex systems. As previously discussed in the literature review section of this thesis, it is often impractical to perform a full-scale experiment on such systems. In such a case, the system can be broken into simpler tiers, also known as an experimental hierarchy, that captures separate physics phenomena or represents a single type of loading. The deformation for each type of load can be evaluated separately to inform the design of the combined experiment. It is also possible to superimpose the deformation behaviour from the separate phenomenon to account for the deformation behaviour of the full-scale system. A full-scale engineering system can be described as a system that includes multiple physics domains and components operating simultaneously over a length of time.

The superposition principle has been applied for decades in the field of science and engineering and has been increasingly used most recently to analyse system loads. Lihui and Meng [143] applied a modal superposition approach to determine the train-induced dynamic Stress Intensity Factors (SIFs) of tunnel lining cracks using a computational simulation. Keller and co-author [144] demonstrated the applicability of the superposition principle of SIFs to include high compressive residual stresses and crack closure phenomena of their specimen. It is reasonable to imply that this technique has been widely used and accepted in the science and engineering community, and its principles have been employed in this research to combine the processes from the thermal and mechanical components. The principle of superposition is valid only when the system being analysed remains within the linear elastic range or domain, and this was considered during the design of the thermo-mechanical experiment.

As a recap, one of the purposes for designing the thermo-mechanical rig or combined thermal and mechanical rig was to demonstrate the feasibility of processes in the enhanced validation flowchart in figure 7 and to illustrate a method for designing multi-physics validation experiments.

In the enhanced process flowchart, it was proposed that deformation results can be superposed from different physics domains with the associated uncertainties to give an approximation of the combined effect. The system must be elastic for the superposition principle, which is also desired for engineering structures in operation. It was also significant that the boundary conditions of each physics domain, i.e., the thermal and mechanical physics domains, are replicated in the combined thermo-mechanical physics domain. Altering the boundary conditions of the different single physics domains would most likely produce results that are not relatable to the individual physics domains. Therefore, for this combined experiment, care was taken to capture the boundary conditions from the individual physics domains, as described in sections 4.6.2 and 4.6.3, respectively.

In the work reported in this thesis, the thermo-mechanical system was assumed to be a multi-physics system with different occurring physics domains, i.e., the thermal and mechanical physics domains. The thermo-mechanical system was broken into the thermal and mechanical single physics domains following the hierarchical experimental approach recommended in [36] to allow a straightforward, well-characterised experimental design and test. Likewise, breaking the experiment into two phases: the thermal and mechanical components allowed the significant uncertain parameters of each physics domain to be identified and quantified in the final outcome.

4.6.2. Thermo-mechanical Experimental Design and Instrumentations

The mechanical test rig described in section 4.5 in this thesis was adapted to include the thermal effect to achieve a thermomechanical test. Since the superposition principle assumes a linear elastic relationship between the applied loading and the resultant response, it was necessary that the maximum deformation measured in this work be less than the elastic limit of the test specimen.

The following were considered during the design of the thermomechanical rig for the purpose of performing validation tests:

1. It was essential to maintain the boundary conditions from the thermal and mechanical experimental designs,
2. The test was designed within the linear elastic domain of the specimen, as fracture of the material was out of scope,
3. The test was designed for safe operation.

The actions taken to incorporate the mentioned considerations are discussed in the subsequent paragraphs of this section.

To maintain the boundary conditions of the thermal and mechanical experiments in the thermo-mechanical experiment, the mechanical servo-electric bending rig was equipped with the quartz lamp (heating element) from the thermal experiment in a three-point bend test configuration. The geometry and dimensions of the end-caps were specially designed for the thermo-mechanical experiment to provide the following functions: 1) to provide a simply-supported boundary condition for the test specimen, 2) to hold the heating element in the horizontal position inside the tube specimen, and 3) to act as a housing unit for the ends of the heating element as illustrated in figure 29. The design and functions of the end-caps were to aid in maintaining the boundary constraint from the thermal test in the thermos-mechanical experiment.

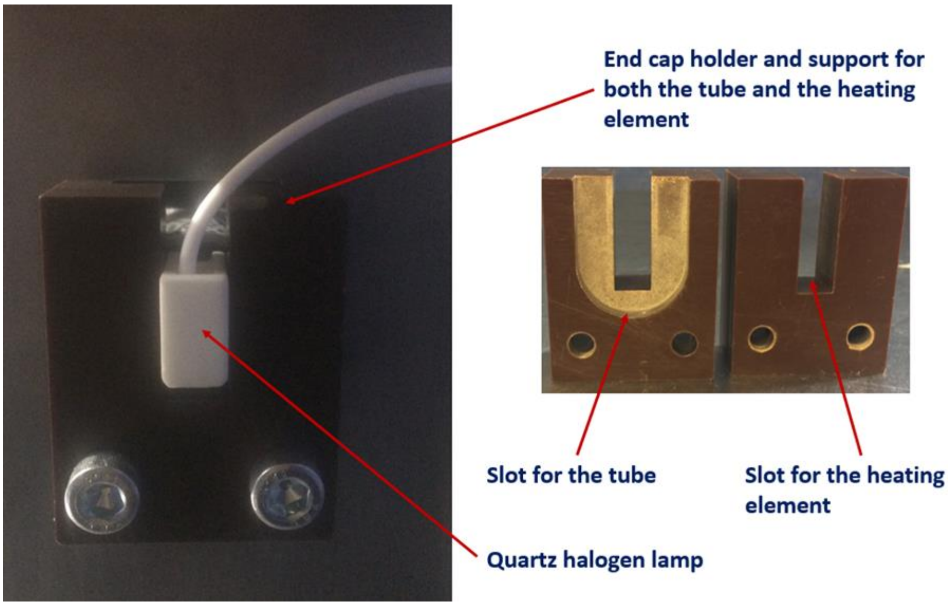

Figure 29: Photographs of the end-caps showing its function as a holder for the heating element (left) and its geometry (right)

In the thermal experiment, mild steel material was used to design the end-caps. However, for the mechanical and thermo-mechanical experiments, the end-cap, loading pins and reactions pins were made from a polyimide laminate material commonly known as Tufnol 6G/92. Tufnol material was used in the thermo-mechanical experiment primarily because of its low thermal conductivity compared to mild steel and high fracture strength, making it suitable for use in the thermomechanical test environment. In addition, it was necessary to maintain the significant boundary and loading conditions from the thermal and mechanical experiments. Tufnol material has a low thermal conductivity compared to the test materials, 316L stainless steel, and was used to prevent significant heat conduction from the specimen during the thermo-mechanical loading. This was necessary to replicate or maintain the exact thermal boundary condition from the thermal-induced deformation experiment described in this thesis. The end-caps were also designed to produce the simply-supported constraint boundary condition from the thermal and mechanical experiments.

As previously mentioned in this thesis, the experimental campaign was designed within the specimen's elastic limit. Preliminary tests were performed to ensure that the specimen was not loaded beyond its elastic limit, as illustrated in figure 16 of this thesis. The test helped determine the magnitude of the bending and thermal load that would generate an elastic response. The results obtained from the preliminary bending tests showed that the tube remains perfectly elastic up to approximately 3000 newtons with a resultant deflection of 1mm. The elastic response behaviour of the tube subjected to bending load would further reduce in the addition of the thermal load. Therefore, it was reasonable for this work to apply a bending load of 400 newtons, as the thermal loads generate thermal stresses, which would further reduce the material's stiffness. Also, the specimen or tube s equipped with the halogen quartz lamp, which has a diameter of 10mm, resulting in a radial gap or clearance of 12 mm between the inner diameter of the tube and the quartz lamp. Therefore it was crucial in this experiment to ensure that the displacement generated due to bending and expansion does not break the quartz lamp inserted inside of the tube. This reason was an additional justification for employing a bending load of 400 newtons.

In the combined experiment, the impact of the heat generated by the halogen quartz lamp on the measurement components of the rig was a challenge because the measurement devices, such as the laser displacement sensor and the load cell, have operating temperature limits below the maximum thermal load applied to the tube. As a result, the effect of temperature could limit the operation of these devices. To mitigate this challenge, the laser displacement sensor and the load cells were positioned at a range where the temperature from the tube was not significant to the function of the device. The laser displacement sensor has an operating temperature of 70^{o}C and was positioned approximately 75mm away from the surface of the heated tube. Also, the top frame of the rig acted as a shield for the displacement sensor and prevented heat from the tube from being dissipated on the measurement devices that were attached to the rig. In the case of the load cell, it was positioned at a range (50 – 60 mm) away from the heated tube underneath the Tufnol loading pin, where the temperature was within its operating temperature. The Tufnol loading pin also served as a shield for the load cell due to its thermal resistance material property. The temperatures of both devices were closely monitored by a hand-held temperature probe to ensure that the temperature was within its operating range and for the safe operation of the devices. The experiments were performed remotely in an environment chamber for safety.

4.6.3. Thermo-mechanical Experimental Procedure

In the thermo-mechanical experiment, the test specimen was loaded thermally from ambient temperature to a maximum temperature of approximately 200°C with the halogen quartz lamp, and a constant force of 400 Newtons was applied to the mid-span of the tube in a three-point bending configuration with the DC-powered screw jack. A reference image of the specimen was recorded at ambient temperature and at zero-load. Subsequent images were obtained at increments of 25°C up to a temperature of 200°C at a constant force of 400 Newtons. Full-field surface temperature and displacements were acquired with the microbolometer and the pair of stereoscopic DIC cameras (with the same settings as used for the thermal and mechanical experiments), respectively, as illustrated in figure 30. In addition, the circumferential displacement of the tube and the translating screw jack were monitored with the laser displacement sensor and the magnetic linear encoder, respectively. The test was performed under hybrid displacement/load control as described in the mechanical experiment and illustrated in the process flowchart in figure 27.

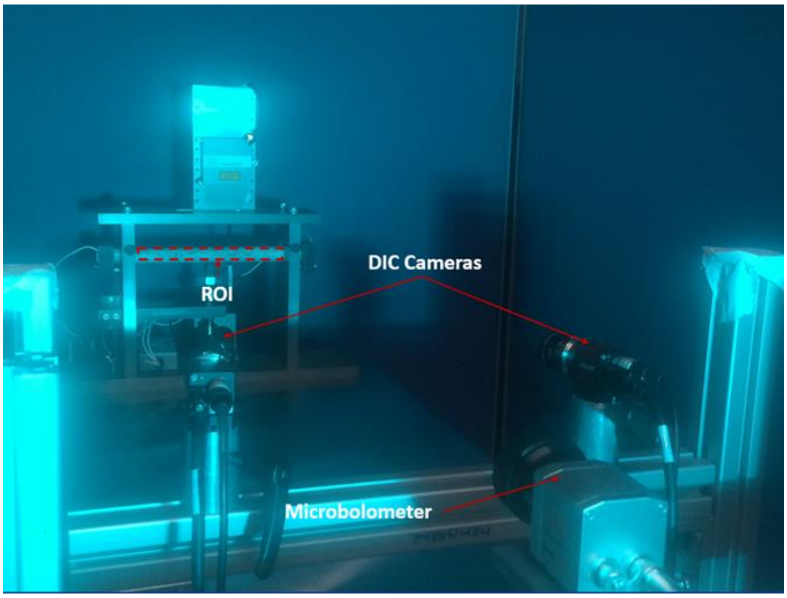

Figure 30 The thermo-mechanical rig setup with the DIC and microbolometer measurement devices

4.7. Numerical Study: Development of the Finite Element Models

4.7.1. Introduction

One objective of this research project focused on the development of Finite Element (FE) models of the simplified case study in section 4.1 of this chapter and included models of the thermal, mechanical, and combined thermal and mechanical (thermo-mechanical) components. The FE models are used as tools to demonstrate the processes of the proposed extended validation and uncertainty quantification (UQ) methods for multi-physics simulation. It is important to note that the focus was to demonstrate the validation process for multi-physics simulations, including quantifying multiple measurement uncertainties rather than creating a perfect model. Therefore, the models developed as part of this project are not intended to be used for in-depth investigation of the performance of the tube.

As previously mentioned in Chapters 1 and 2, computational models are increasingly being used in the science and engineering industries as a substitute for physical tests. It is expensive to design and build a full-scale system to perform physical tests. This has led to increased interest in Model-Based System Engineering (MBSE) to shorten development time and lower costs. The question of reliability arises when employing the results from a computational simulation to inform decisions regarding the structural worthiness of engineering components. The accuracy of such models is usually determined through a validation assessment. A robust validation assessment reveals how well a model and its embodiments in a computer code represent the physical system it is designed to represent.

An extended flowchart has been developed as part of the project and is presented in Chapter 3 to describe the validation of multi-physics computational models. The processes in the flowchart illustrate a hierarchical approach to designing experiments and combining the associated uncertainties from single physics domains to predict the behaviour of a component or system in the multi-physics domain.

Three different models were developed in this work, representing the physical experiments; the thermal, mechanical, and thermo-mechanical models. The thermal expansion tube is referred to as the thermal model. The three-point bending of the tube represents the mechanical model. The thermo-mechanical model involves the combined loading regime from the thermal and mechanical models, including its associated boundary conditions. The system response quantity (SRQs) predicted for this project is the in-plane displacement fields.

4.7.2. Development Process of the Finite Element Models

Finite Element (FE) modelling is widely used in structural design as a predictive tool for solving problems involving static and dynamic loading. On a broader scale, FE can be achieved in seven steps, namely: 1) modelling, 2) material definition, 3) system excitation or loading definition, 4) boundary conditions, 5) meshing, 6) solution or solver, and 7) post-processing. Steps 1 to 5 can be grouped as the pre-processing stage, and step 6 is the problem-solving stage.

The pre-processing stage involves the development of a discrete system having independent elements known as the mesh. The mesh represents the mass and stiffness of a continuous system or component, as in the case of this project. In other words, the geometry of the continuous structure is divided into smaller discrete shapes called finite elements that make up the mesh. Each of these elements is defined by a mathematical description regardless of the complexity of the structure. The boundary conditions of nodes and elements, along with the structural material's properties, are also defined in the pre-processing stage of a FE analysis and impact the mathematical description of the element. The boundary conditions include the initial condition of the structure and its environmental conditions, constraint, system excitations or loads, and analysis type used to run the model. The selection of the analysis type is based on the physical phenomenon of the model and the governing equations, which could be linear or non-linear relations. When a linear relationship is assumed between the system load and the corresponding displacement, the solver assembles the global

stiffness (K) and the force (F) vectors to solve the problem equation. For static analysis, this is given as:

$$KU = F \tag{4.3}$$

where U is the displacement vector, and it is unknown.

The outcome of the pre-processor stage produces a set of instructions passed onto the solver in the problem-solving stage. In this stage, the partial differential equations are converted to linear or non-linear algebraic equations in terms of matrices. The matrices of the individual elements are assembled into global matrices for the continuous structure and then solved for the unknown variables. The solver processes the code and generates an output that is a representation of the solution. In the post-processing stage, the output results generated by the solver are presented in the form of displacement/stress/strain contour and plot diagrams.

The finite element models presented in this thesis were developed using the Abaqus/Standard software package version 6.14 (Hibbitt, Karlson & Soreson Inc) for the pre-processing analysis and post-processing of the results. The Abaqus/Standard software package can simulate linear and non-linear problems and was suitable for this work as it required less computational time than Abaqus/Explicit.

4.7.3. Thermal Component: Thermally-Induced Deformation of a 316L Stainless Steel Tube

This section of this chapter details the development of the thermal FE model as part of a combined or coupled thermal and mechanical model. The thermal model represented a single physics domain or phenomenon and was designed to capture the boundary conditions and constraints in the physical experiment reported in section 4.4, i.e., the thermal deformation experiment. The thermal expansion finite element model represents physics domain one of the enhanced process flowchart in figure 7.

An FE model of the test specimen, a grade 316L stainless steel tube subjected to internal elevated temperatures, was developed with the temperature-dependent material properties presented in Table 3. Plots of the Young's modulus and coefficient of thermal expansion as a function of temperature are presented in the discussion chapter of this thesis. The thermal model was developed to capture the in-plane, axial and circumferential displacements and to demonstrate the process of performing a hierarchical validation assessment detailed in Chapter 2.

In this work, the FE model representing the tube specimen has an outer diameter of 25.4 mm, an inner diameter of 22.1 mm, and a length of 310 mm was modelled in Abaqus/Standard software package and using a global coordinate system as shown in figure 31.

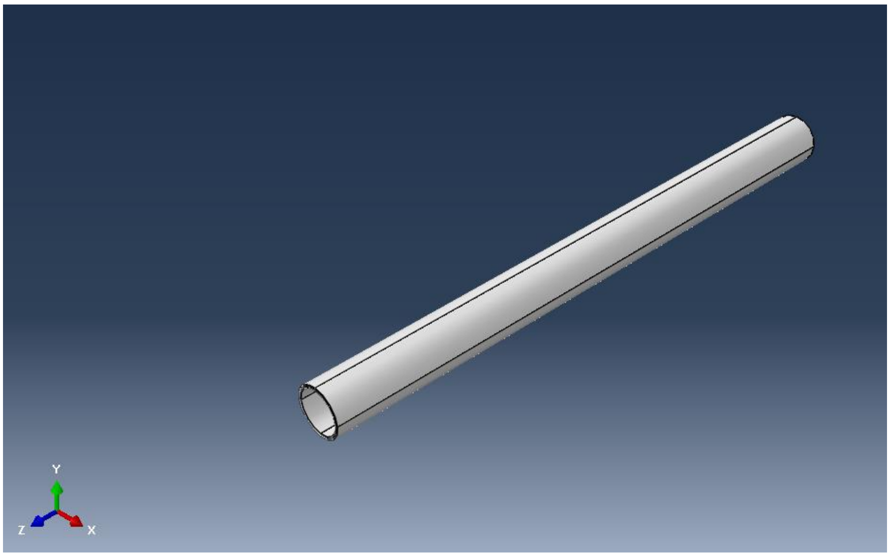

Figure 31: Modelled geometry of the tube for the thermal model

The tube model was meshed using an 8-node linear hexahedron element type, C3D8R, with reduced integration and hourglass control for a reduced computational time. A total of 6240 elements and 7900 nodes were used for meshing the tube geometry. During the meshing of the tube, a preliminary mesh convergence test was performed to determine the sensitivity of the mesh size to the displacement solution generated. The tube was initially meshed with 12400 elements and 16000 nodes and generated a displacement solution that was comparable to the solution obtained with the mesh in figure 32 (used in this study) but took thrice the computational time for the solution to converge. The mesh size was gradually altered until it was clear that additional mesh refinement did not affect the solution generated.

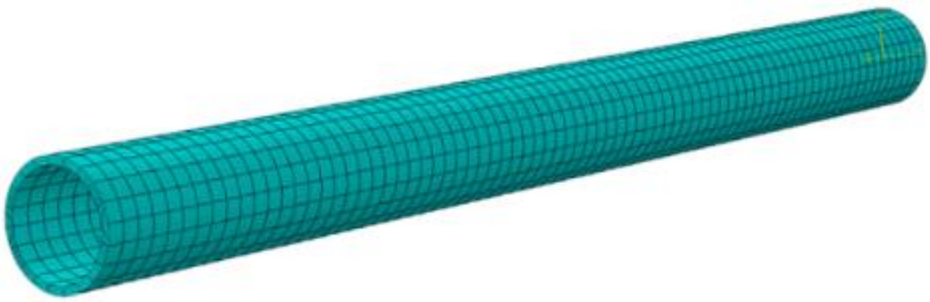

Figure 32: Diagram of the thermal model mesh, linear hexahedron elements with reduced integration was used for the mesh

The development of the 3-D FE thermal model was based on the following assumptions:

1. The model has a uniform initial temperature of 28°C, which was obtained from the thermal experiment and used as the initial boundary condition in the FE model
2. The geometry was assumed to be ideal and does not account for any geometric imperfections for simplicity,
3. The material was assumed to be isotropic for simplicity,
4. The analysis was defined using a linear relationship between the applied load and the corresponding displacement to capture the design of the corresponding experiment,
5. The stiffness matrix was assumed constant throughout the study, and
6. A simply-supported constraint was assumed in the model and is believed to represent the experimental constraint.

The constraint from the thermal experiment was simplified in the model, which means that the end-caps and clamps used in the experiment were not included in the model. The constraint from the thermal experiment was replicated in the model by constraining specific nodes at the end of the tube's outer diameter to prevent translation and rotational displacement, as shown in Figure 33. This was defined as the initial condition before thermal loading.

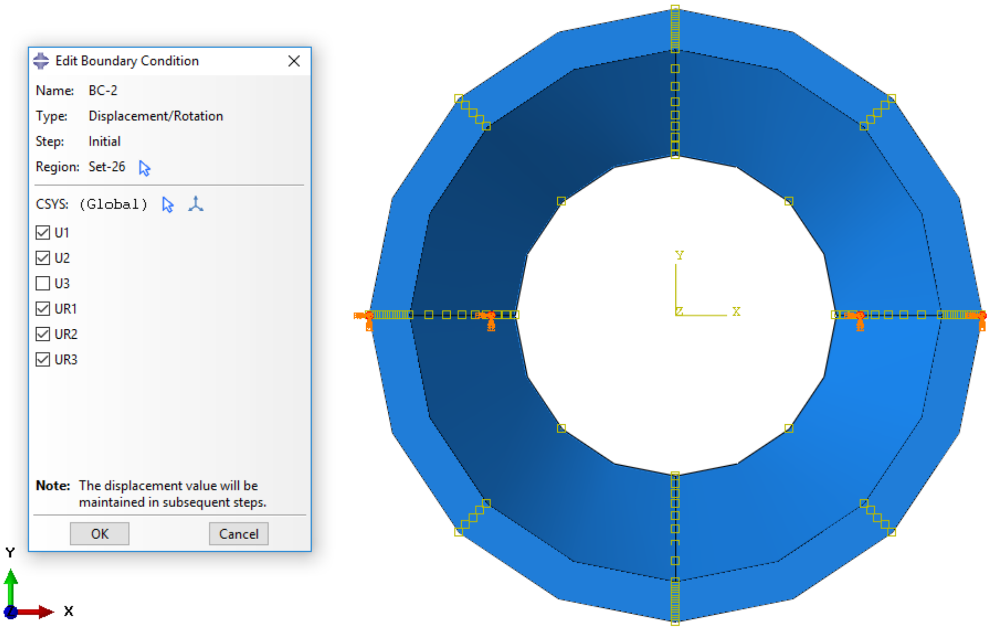

Figure 33: The thermal model showing the nodal constraint represented by the yellow ribbons, defined as the initial condition of the tube before being subjected to elevated temperature loading

In this model, U1=U2=UR1=UR2=UR3=0, U3≠0, where U and UR represent the translational and rotational displacement, respectively, in the x,y, and z-directions. This implies that the tube was constrained in the circumferential (U2 and UR2) direction and in the radial UR3 direction but allowed displacement in the Longitudinal U3 direction.

A uniform temperature of 28^{o}C was pre-defined as the reference temperature in the FE analysis. The temperature was linearly increased to a maximum of 200^{o}C in every 25^{o}C increment, as shown in figure 34.

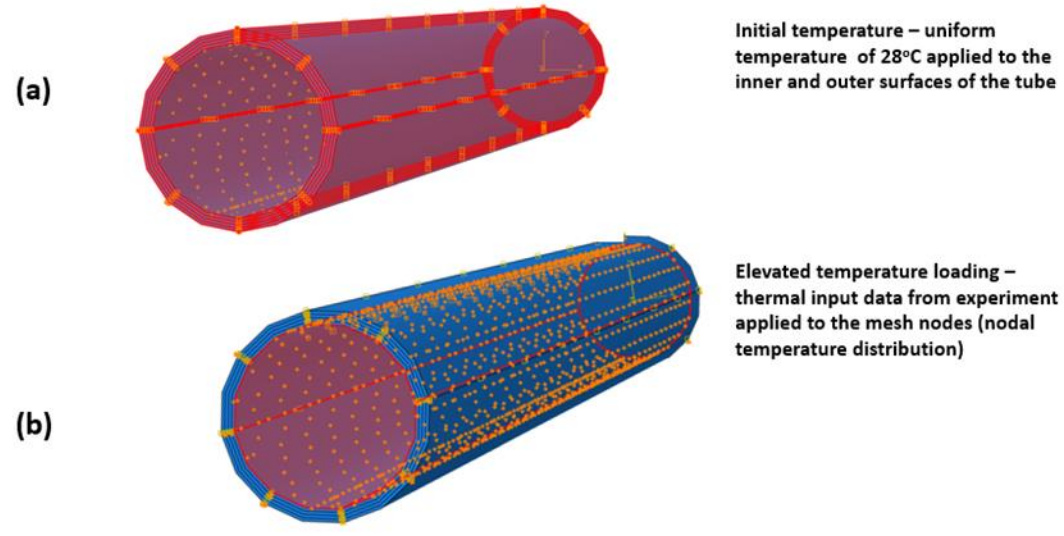

Figure 34: The thermal finite element model of the tube showing (a) reference uniform temperature (28^{0}C) distribution and (b) the tube at elevated temperature to a maximum of 200^{0}C at every 25^{0}C increments

The temperature load used for this analysis was acquired from the thermal experiment with the microbolometer. A Matlab script in the appendix was specially written to wrap the temperature profile captured from the experiment around the geometry of the finite element model, as depicted in figure 34, to represent the experiment using the pre-defined field interface in Abaqus modelling software.

The analysis was performed over a timeframe of 1800 seconds for each step load (i.e., for each temperature increment) corresponding to the experiment. The recommended Full Newton solution technique was selected for this analysis, as it is recommended for iteration problems in the Abaqus software package.

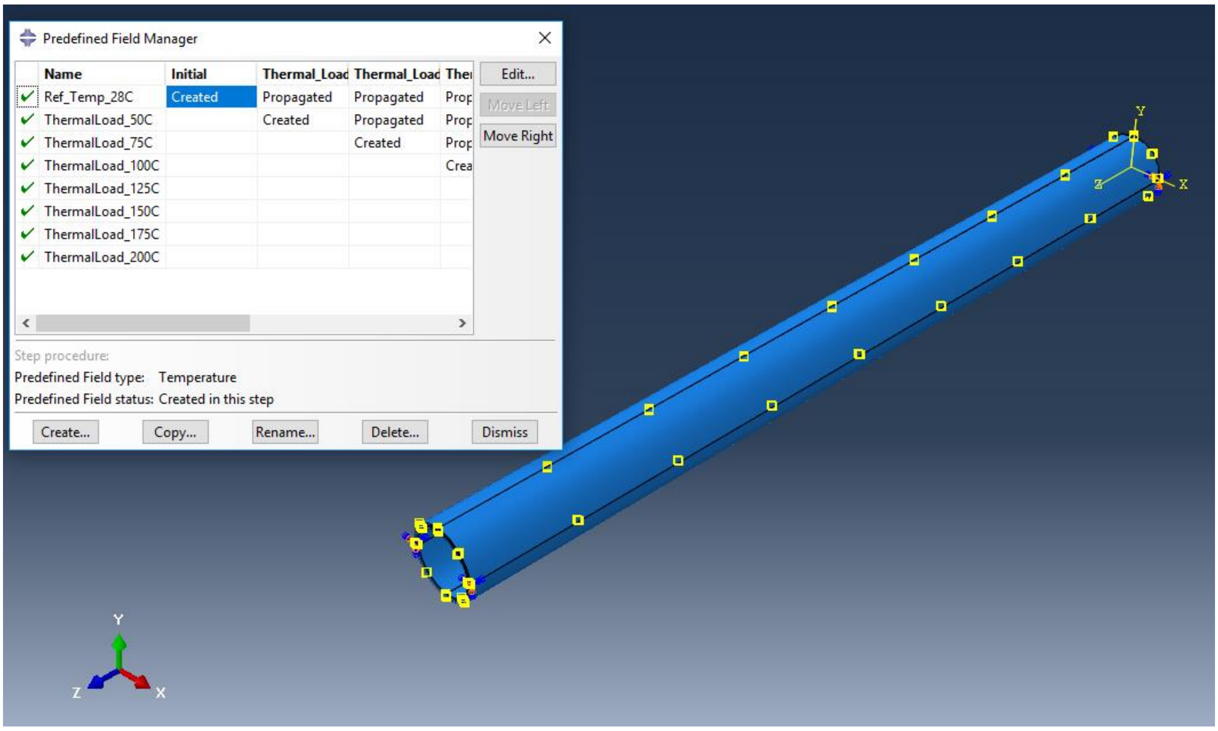

Figure 35: The tube finite element model showing the incremental temperature loads specified in the pre-defined field

On successful completion of the simulation run, the temperature profile generated for each increment load was extracted and compared to the temperatures recorded from the thermal experiment. The system response of interest for this analysis are the longitudinal and circumferential displacements.

The next section details the mechanical component, which is a model of the tube subjected to bending load in a three-point bending configuration.

4.7.4. Mechanical Component: Three-Point Bending of a Simply Supported 316L Stainless Steel Tube

In the mechanical analysis reported in this chapter of the thesis, the test specimen, a simply-supported stainless steel tube of grade 316L, was subjected to external mechanical bending at room temperature in a three-point bending test configuration. The three-point bending finite element model represents the physics domain two in figure 7. The configuration model is based on the setup of the physical experiment, i.e., the mechanical experiment reported in section 4.5. For simplicity, only the crucial features of the test rigs, such as the stainless-steel tube, the loading and reaction pins, were modelled in this analysis, as illustrated in Figure 36. The geometry and dimensions of the tube and pins used in the physical test were replicated in the mechanical model.

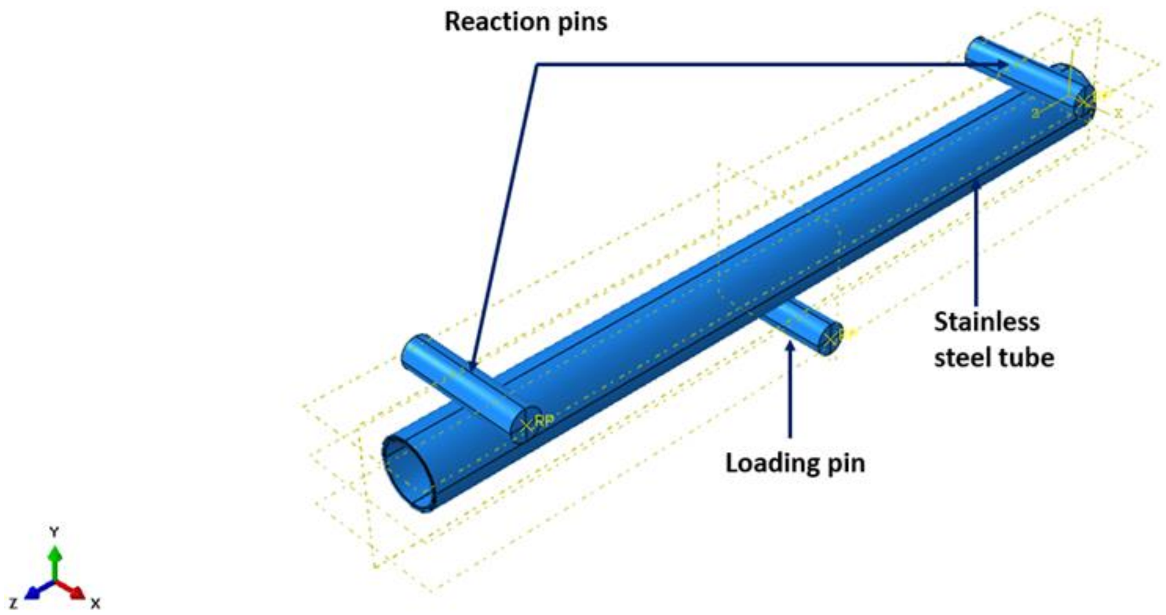

Figure 36: Mechanical model showing the tube subjected to a three-point bending configuration with the load and reaction pins

The tube was modelled and meshed with the same elements (linear hexahedron elements, CD38R) used in the thermal model. The addition to the mechanical model is the reaction and load pins, which were modelled with discrete rigid quadrilateral elements, R3D4. Rigid body elements were used to model the pins to assume that the pins would remain undeformed throughout the analysis. Rigid body is a collection of nodes and elements whose motion is governed by the motion of a single reference node, illustrated by the reference point (RP) in figure 36. The relative motion of the nodes and elements in a rigid body remains constant throughout the simulation and, as such, does not deform but can undergo large rigid body motions. In this study, it is assumed that the reaction and loading pins remain rigid during the analysis. Therefore, the pins do not undergo deformation when in contact with the tube during loading. In other words, the pins were used as a form of boundary constraint in the analysis. A total of 2433 elements and 2285 nodes made up the mesh of the loading and reactions pins, as shown in figure 37. The pins modelled in this analysis were 50 mm in length with a diameter of 12 mm each, which corresponded to the dimensions of the physical pin used in the mechanical experiment. The global cartesian coordinate system, X, Y, Z, used in this study is defined along the thickness of the pins, transverse, and axial directions, respectively.

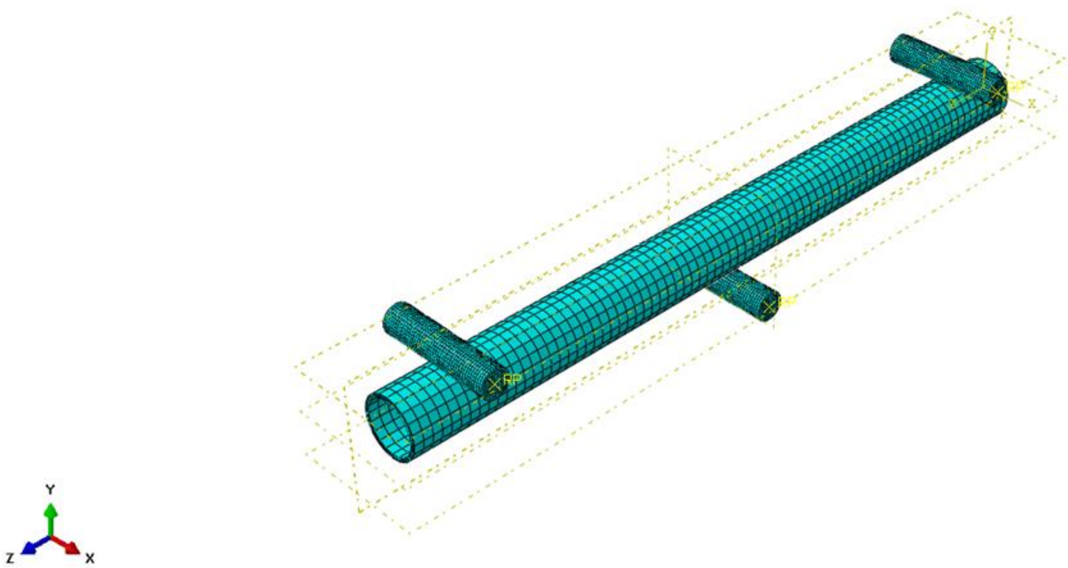

Figure 37: Mechanical model showing the configuration and meshing of the tube and pins

The configuration of the three-point bending model has a span length (the distance between the reaction pins) of 260 mm with the loading pin positioned in the middle of the tube's length, i.e., L/2 corresponding to 310/2 mm.

The boundary conditions from the physical test, which were the constraint and contact between the tube and the pins, were replicated in the model by applying a Master-Slave contact interaction method, as illustrated in figure 38. The rigid body surfaces were connected to the deformable tube surface using a surface-to-surface contact method that employs a Master-Slave contact algorithm. In this study, the pins were selected as the master surface, as recommended in Abaqus/Standard for rigid bodies, and the tube (deformable-body) is set as the slave surface. A finite sliding solution was selected for this analysis, as recommended in Abaqus for such simulations. Finite sliding allows arbitrary relative motion between the contacting surfaces, and a coefficient of friction between the surfaces of the tube and the pins was defined as 0.2, as recommended in Abaqus. The frictional force served to resist the relative sliding of the surfaces in contact. This force was maintained in the analysis on the condition that the surfaces remained in contact. However, in this analysis, the surfaces were allowed to separate after contact, and no penetration of the interacting surfaces was permitted.

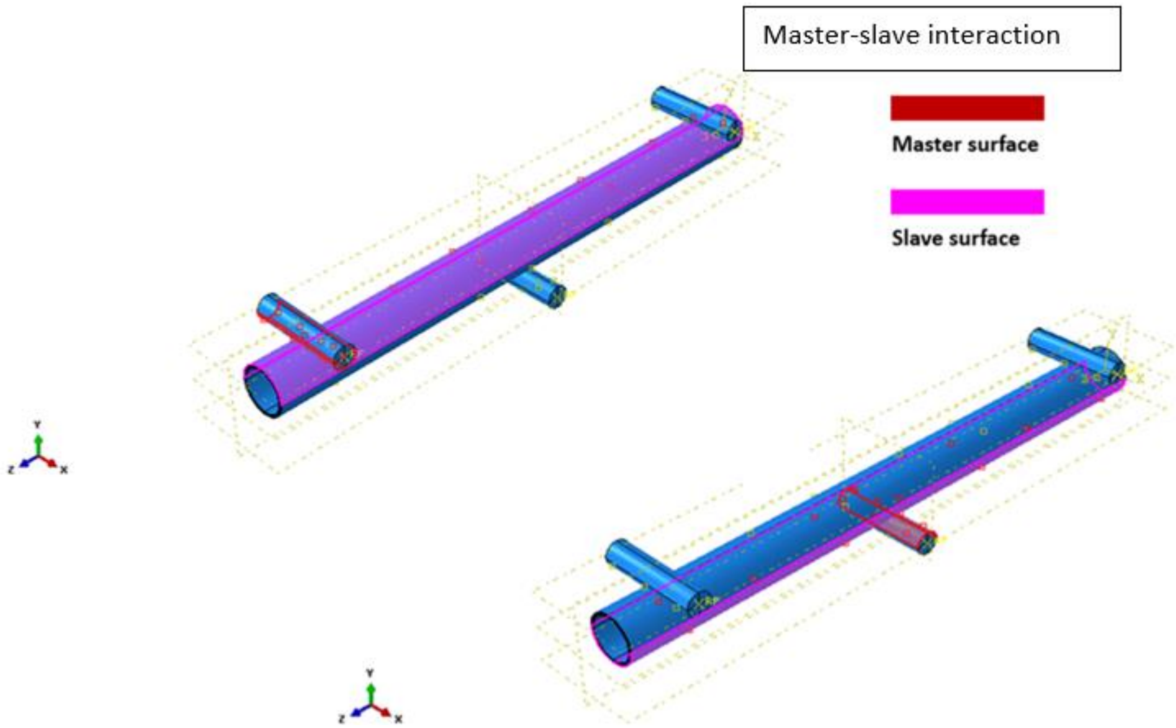

Figure 38: The mechanical finite element model illustrating the surface-to-surface contact and interaction solution used in the analysis

In this study, the reaction pins were constrained in the x, y, and z directions to prevent displacement during mechanical loading, implying that U1=U2-U3=UR1=UR2=UR3=0. On the other hand, the loading pin was only constrained in the x and z- directions but was allowed to displace in the y-direction for loading purposes. The tube was loaded in bending with a constant concentrated force of 400 Newtons, which was applied through the reference point (RP) of the loading pin. The model was solved to determine the in-plane, axial (longitudinal) and transverse (circumferential) displacements resulting from the applied force.

The next section of this chapter describes the coupled thermal expansion and three-point bending finite element model.

4.7.5. Thermo-mechanical Component: Coupled Thermal and Mechanical Deformation of a Stainless-Steel Tube

The coupled thermo-mechanical FE model represents physics domain three of figure 7. This model is a combination of the thermal expansion and three-point bending behaviours modelled in the preceding sections of this chapter. Therefore, the assumptions, boundary conditions, constraints, and system loads from both the thermal and mechanical physics domains were integrated into the combined or coupled thermo-mechanical FE model.

The intended use of the thermo-mechanical finite element model was to validate the displacement results from the superposed thermal and mechanical experiments and predictions and demonstrate the processes in the new extended validation flowchart.

In the thermal and mechanical finite element study, the models were modelled using a linear hexahedron element for 3D stress analysis. However, to capture the combined thermal and mechanical behaviour, a coupled temperature-displacement element with reduced integration, C3D20RT, was used in the thermo-mechanical analysis. In this coupled analysis, the effect of the temperature load on the tube's displacement and the displacement effect on the temperature is considered and solved simultaneously.

The thermo-mechanical model configuration is the same as the mechanical finite element model in figures 36-38. The system was modelled in a three-point bending configuration with fully coupled-temperature-displacement elements. The rigid loading and reaction pins were modelled as element-based rigid surfaces. As previously mentioned, the rigid body reference points (RP) for the rigid surface that defines the reaction pins are fully constrained to have no rotational displacement (UR) and translational displacement (U). The loading pin was allowed to move in the transverse y-direction.

The thermal boundary conditions, elevated temperature loads and constraints used in the thermal expansion finite element model were prescribed in the thermo-mechanical model. In this analysis, the tube is thermally loaded from a reference temperature of 28^{o}C to a maximum elevated temperature of 200^{o}C in increments of 25^{o}C. A concurrent constant force of 400 Newtons was prescribed at the reference point of the loading pin to provide the mechanical bending load of the tube. The thermo-mechanical model was solved for transverse or circumferential and axial displacements resulting from the combined thermal and mechanical loading.

4.8. Conclusions

A thermal, mechanical, and thermomechanical rig has been successfully manufactured and tested with the associated numerical simulations to meet the aims and objectives of this research. To recap, the aim of this research was to develop an approach for the validation of multi-physics computational models using data obtained from validation experiments. One of the research objectives includes designing validation tests for the different physics domains illustrated in the enhanced flowchart of figure 7, using the nuclear energy fuel cladding as a suitable case. The thermo-mechanical component was split into two individual physics domains, the thermal and mechanical physical components, to illustrate the hierarchical approach to designing a multi-physics experiment, which was another objective of this research

In the thermal component, the tube (an idealised cladding in this work) was subjected to a maximum temperature load of 200°C to study the thermal expansion phenomenon and generate full-field displacement data for the validation of the corresponding simulation. The thermal experiment represented the effect of the fuel pellet on the cladding, as described in section 4.1 of this chapter. The mechanical component, which includes the physical test and the numerical simulation, was then designed to study the tube deformation due to a three-point bending to loads of 400 newtons and represents the effect of the coolant pressure on the cladding. Finally, the effect of the thermal and mechanical components was successfully coupled to produce the thermo-mechanical phenomena of the tube subjected to a maximum thermal load of 200°C and a bending load of 400 newtons. The boundary conditions from the individual physical tests were successfully maintained in the combined thermos-mechanical test through the control measures taken during the design phase. The thermo-mechanical experiment corresponds to the idealised phenomenon of a nuclear energy fuel cladding during the service operation.

The experimental campaign described in this chapter meets the second and third objectives of this research, which was aimed at designing multi-physics validation tests following a hierarchical approach by splitting the coupled physics into single physics components where it is feasible to obtain the boundary conditions and data needed to design the combined thermo-mechanical experiment.

Chapter 5

5. Assessment of Measurement Uncertainty

5.1. Introduction

This section of this thesis details the process followed to determine the minimum measurement uncertainty for the thermal, mechanical and thermo-mechanical experiments. As previously mentioned, Digital Image Correlation (DIC), an advanced non-contact optical technique, was used as the measurement technique to acquire full-field surface displacements in the physical tests. The DIC technique has been widely used due to its advantage of only requiring a simple equipment setup compared to other optical measurement methods such as the electronic speckle pattern interferometry (ESPI). However, there is an increased interest within the stress analysis community and industry to determine the level of uncertainty in measurements made with a DIC system if it is to be used alongside computational techniques [145].

Over the past decades, researchers have been increasingly investigating the sources of errors associated with the DIC technique. Rigid-body motion [94] has been used to investigate and to estimate the measurement errors associated with the lighting, optical lens, and speckle patterns. Pan [136] investigated thermal errors associated with DIC by providing a theoretical analysis that underpin the origin of the thermal errors that originate from self-heating and ambient temperature. The author also attempted to quantify these errors through a designed experiment. Other works have attempted to assess the errors associated with a DIC technique using deformation fields generated from a synthetic finite element analysis [146]. These studies address the uncertainties associated with the DIC techniques based on their limitation from a theoretical aspect and provide insight into the general capability of the technique.

The limitation to these studies is that the information provided does not capture the level of uncertainty obtained with a specific system setup used in a routine experiment. The Standardization Project for Optical Techniques of Strain Measurement (SPOTS) [97], designed a reference material for the calibration of optical systems. The reference material designed by SPOTS can only be used for static in-plane measurements. Hack et al. [101] extended the design concept from the SPOTS project and designed a reference material that can be used for static in-plane, out-of-plane displacements, and dynamic scenarios. Their work used a cantilever as the reference material to evaluate uncertainties associated with measurements of static in-plane displacements and out-of-plane displacements, which was incorporated into the CEN guide [12].

In the context of this thesis, reference material is described as “a material or substance with one or more of its properties sufficiently established to be used for calibration of an apparatus” [145] and offers traceability via an unbroken chain of comparisons to an international standard.

The calibration of a commercially-available DIC system (Dantec Q-400, Ulm, Germany) presented here used the cantilever beam as the reference material and followed the calibration processes of Hack et al. [101] to determine the minimum measurement uncertainty associated with the thermal, mechanical, and thermo-mechanical experimental setups. In this research, the reference material designed by Hack et al. [101] was chosen over the material designed for strain measurement in SPOTs [97]. This was so because the cantilever beam material by Hack et al. has a more simplified geometry requiring a simple experimental setup

The principle underlying DIC is complex and involves various sources of uncertainties. Therefore, the calibration experiment detailed by Hack et al. provides a method to assess the experimental uncertainty associated with a specific experimental setup. According to the CEN guide, the system load and the corresponding displacement obtained from a specific physical test should be accurately represented in the calibration experiment, implying that the system response from the calibration experiment must be similar in magnitude to the system response from the test.

5.2. Reference Material Design and Analytical Description

The reference material used for this measurement calibration was a fixed-free cantilever manufactured using a computer-controlled milling machine from a single piece of 2024 aluminium [101]. The reference material was designed to be scalable, so all the dimensions are expressed as a function of T, that is, the cantilever thickness. The dimensions of the reference material and associated uncertainties are presented in figure 39 and Table 4.

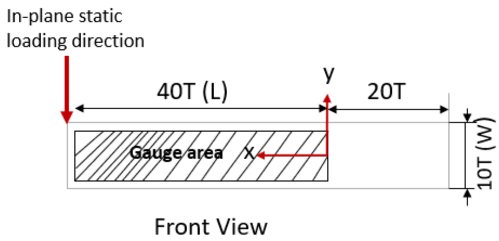

Figure 39: The geometry of the cantilever reference material showing the normalised dimensions with the gauge area shown shaded [101]

Table 4: The critical dimensions of the cantilever reference material and the associated uncertainties

Parameter	Units	Mean values	Uncertainty, u
T	mm	3.98	0.008
L	mm	160.01	0.012
W	mm	40.00	0.014
M	mm	251.6	0.01

The reference material was designed with a thick base to allow it to be securely clamped while a displacement load was applied to its free end. The gauge area was defined as the surface of the cantilever, with the origin of the coordinate system defined at a point in its root. This surface was set as the region of interest and measured with the DIC instrument. The geometry of the cantilever beam was measured using a series of independent observations in order to establish the uncertainty associated with its dimension, and this is given in table 4.

The in-plane, transverse theoretical displacement is derived from m_y^T Timoshenko's beam theory [101].

$$m_y^T = \delta_y \frac{(30\nu L y^2 + 11\nu W^2 x - 30\nu x y^2 + 30 L x^2 + 12 W^2 x - 10 x^3)}{L(11\nu W^2 + 20L^2 + 12W^2)} \tag{5.1}$$

where δy is the tip deflection, L is the length of the cantilever, W its width and ν is Poisson's ratio, and the superscript T indicates that this is a theoretical value.

5.3. Calibration Experimental Procedure

The calibration experiment detailed here was setup to generate values of displacements similar to the maximum values in the data field from the thermal, mechanical, and thermomechanical computational models as recommended in the CEN guide [12] for optical measurement methods. A speckle pattern similar to the one used for the validation experiments was applied to the surface of the cantilever beam using an aerosol can and a paintbrush. The aerosol can was used to apply the white base paint, while the paintbrush was used to apply the speckle pattern (black paint) in order to generate a similar pattern to the one used in the experiments. It is worth noting that a suitable speckle pattern can be used and does not need to be similar to the speckles on the test specimen. What is crucial, according to the guide, is that similar loads applied to the test specimen should also be applied in the calibration experiment. The thick section of the reference material was rigidly clamped to an optical table such that the cantilever was horizontal with the x-y plane vertical. Dead weights of 15kg, 30kg, 45kg, and 60kg, which were suspended from a steel wire, were applied to the tip of the cantilever, subjecting it to a bending moment in the x-y plane. The displacements at the tip and root were monitored using a pair of calibrated dial-gauges, as illustrated in figure 40.

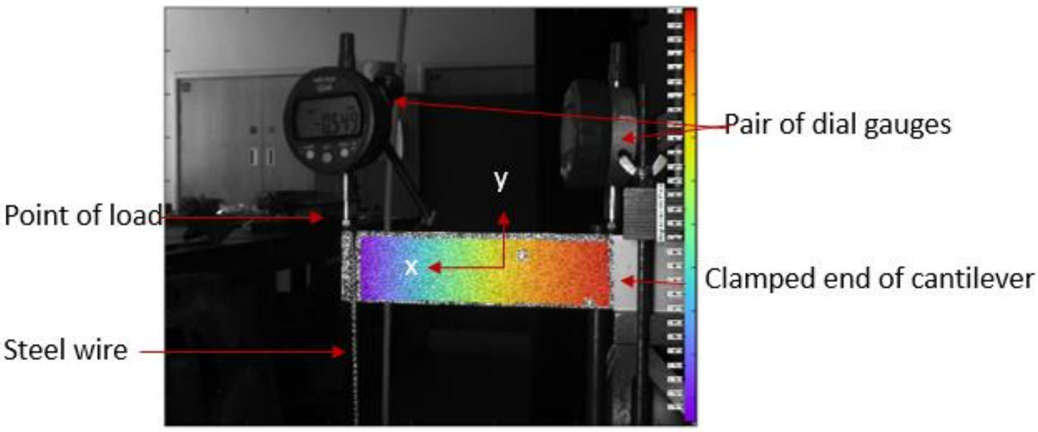

Figure 40: Experimental setup for in-plane loading configuration with a pair of dial-gauges, one at the tip and the other at the root of the cantilever beam for measuring displacements, a steel wire plus a weight hanger used for applying dead-weights

Surface images were acquired using a pair of DIC cameras (1292 x 964 pixels) fitted with a matched pair of 10 mm fixed focal length lenses. The camera arrangement was such that the gauge area was within the field of view resulting in a spatial resolution of 2-pixel mm^{-1}. A green LED light source was used to illuminate the speckle pattern. The cameras were located 500 mm apart at a distance of 550 mm from the surface of the reference material. The setup of the measurement system used for the calibration experiment represents the setup used for the physical tests reported in chapter four of this thesis.

The intrinsic and extrinsic values of the experimental setup were determined by performing a parameter calibration which involved capturing eight images of a specially designed target material. The target was supplied as part of the 3-D DIC system and consisted of a 9 x 9 checkboard pattern of white and black squares. The individual size of the checkboard square was 20 mm, resulting in a total target size of 180 mm by 180 mm.

5.4. Calibration Results

An image of the cantilever beam was captured in the absence of load, which served as the reference image to evaluate the displacements in subsequent images. The images were processed using the proprietary software (Istra-4D, Dantec Dynamics, Ulm, Germany) provided with the DIC system. To allow correlation, the images were subdivided into square facets of size 17 pixels and a grid spacing of 4 pixels, similar to that used for processing the displacement data acquired from the validation experiments reported in this thesis. The full-field displacement results were imported into MATLAB software in the hdf5 file format. For visualisation purposes, plots were produced to compare the theoretical vertical displacement calculated from equation 5.1 to the measured displacements obtained with the DIC system. These contour plots are shown in figure 41.

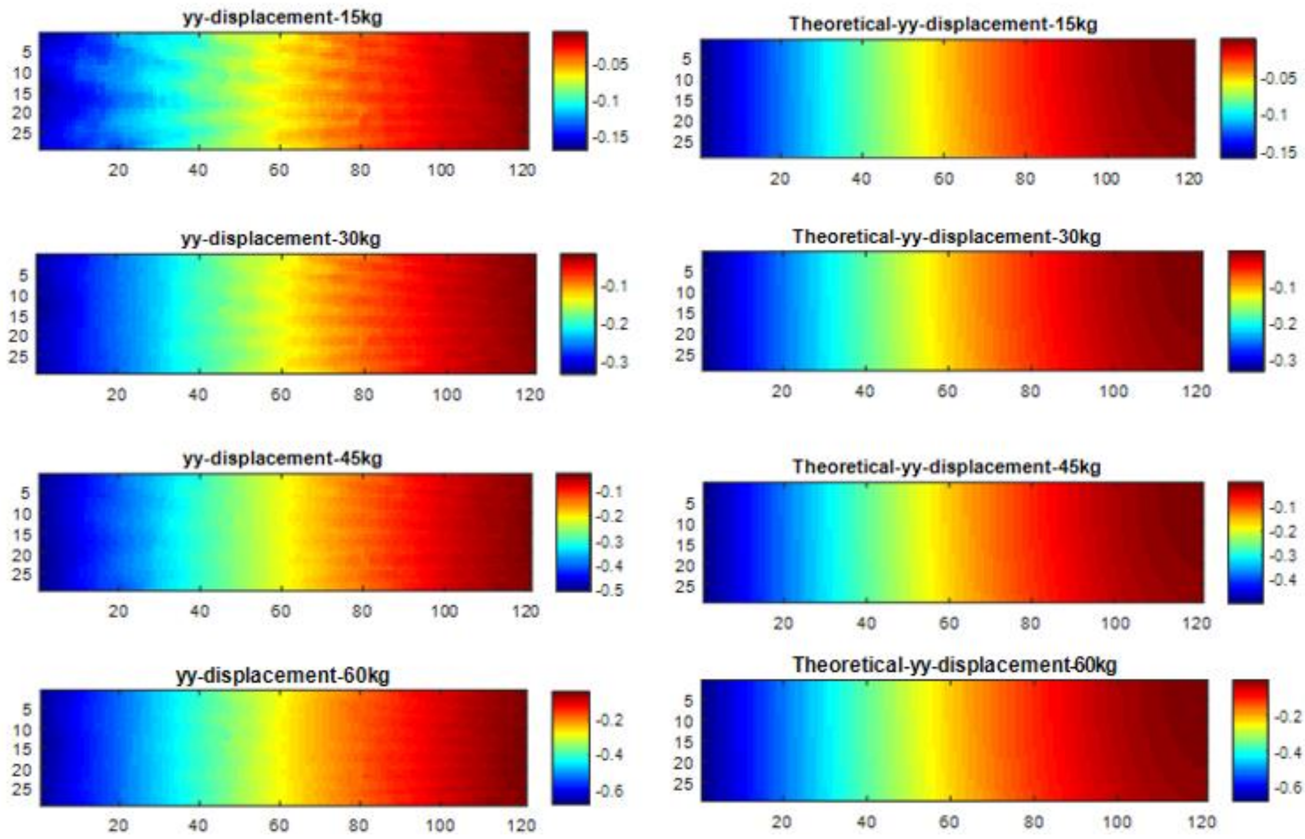

Figure 41: yy-displacement for the reference material subjected to in-plane bending of 5kg, 30kg, 45kg, and 60kg; the data maps of the left: measured from DIC system, and on the right: theoretical surface based on equation 5.1

For the purpose of comparison and as a step toward evaluating the minimum measurement uncertainty, the theoretical displacements at different loads were plotted against the measured displacements, and the Root Mean Squared error (RMSE) between the theoretical and measured displacements were evaluated in MATLAB statistical environment as depicted in the plots of figure 42.

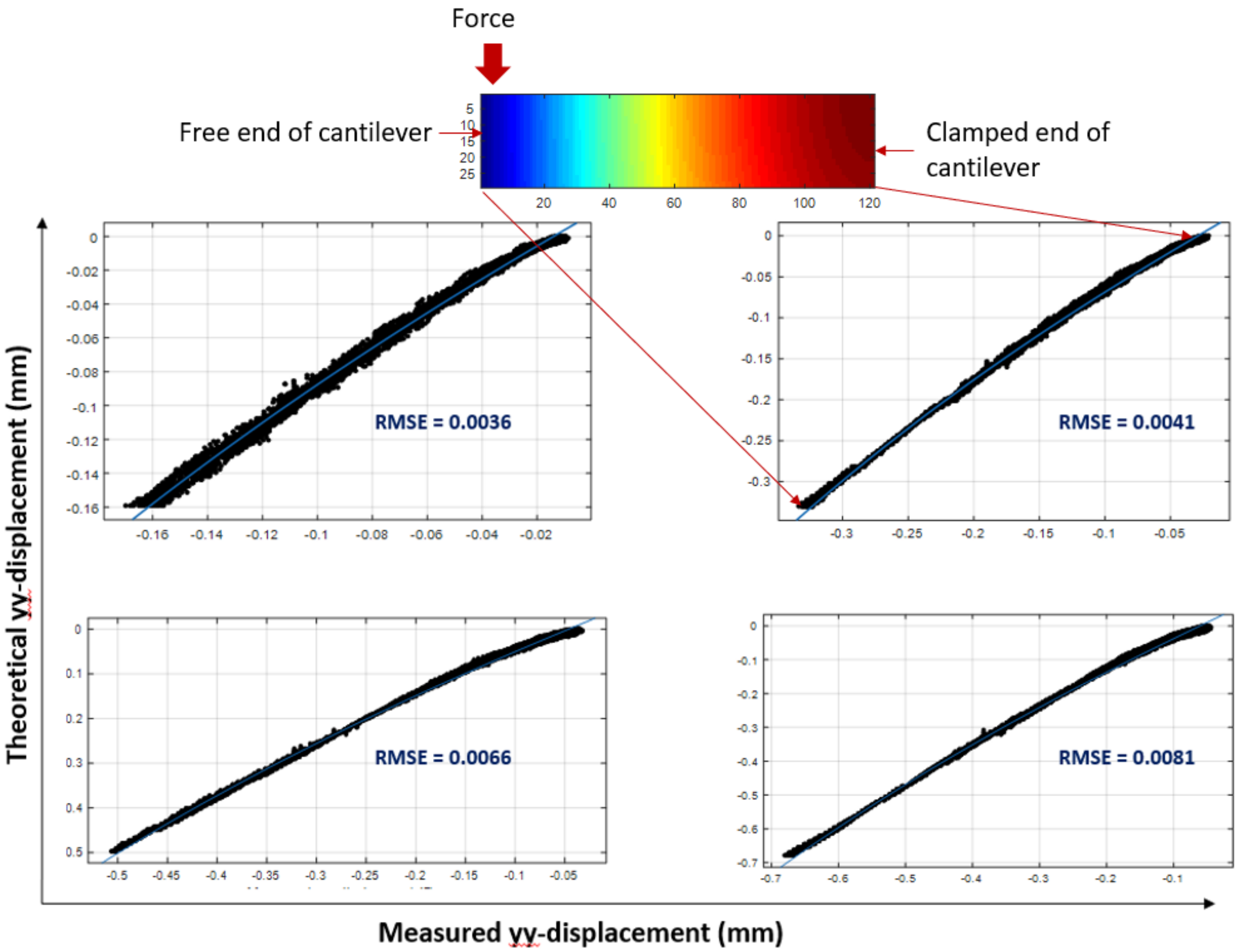

Figure 42: Comparison plots of the theoretical and measured yy-displacements at different tensile loads along with the RMSE

There would be no difference between the theoretical and measured data fields in an ideal situation so that the field of deviations and the RMSE would be zero. However, in practice, this is never the case due to inherent variability and the presence of random uncertainty components, as illustrated in the plots in figure 40. The minimum measurement uncertainties for the thermal, mechanical, and thermomechanical rigs are the RMSE derived and presented in the plots in Figure 42 and are 0.0066 mm, 0.0041, and 0.0081 mm, respectively. The displacement values obtained from the in-plane bending at loads of 45kg and 60kg were similar to the values obtained by Hack et al. [101] and are acceptable for this experimental setup.

5.5. Conclusions

The use of a cantilever reference material to evaluate the minimum measurement uncertainty of the DIC measurement system employed for this project has been assessed for the maximum in-plane displacement fields, in this case, the transverse displacement fields. The minimum measurement uncertainty was found to be 0.0066, 0.0041, and 0.0081 mm, respectively, for in-plane yy-displacements. This uncertainty was evaluated using a protocol embedded in the CEN guide [12] with a modification to allow the application of in-plane bending loads.

The determination of the minimum measurement uncertainty is required for the validation assessment to determine the credibility of the computational models. It is also a measure of the quality of the experimental data.

The minimum measurement uncertainty serves as the first step to evaluating the total measurement uncertainty for the experiments reported in this thesis. The other sources of uncertainties associated with the measurement depicted in the flowchart of Figure 8 can be taken into account when performing the validation assessment between the prediction and the measured system response quantity.

Chapter 6

6. Results and Discussion of the Measurements and Numerical Simulations

6.1. Introduction

A detailed description of the results obtained from the experiment and finite element model for the thermal, mechanical, and thermomechanical physics domains with respect to the load-deformation relationship is discussed in this chapter of this thesis. It is essential to provide a brief recap on the aim and objectives of this project in order to throw light on the significance of the results obtained from the models to be validated and the experiments that were specifically designed, built, and tested or performed to validate the computational models.

The aim of this project was to develop an extended approach or strategy for the validation of multi-physics computational models using quantitative data from a designed multi-physics validation experiment and building on the current state-of-the-art validation processes detailed in literature [4],[5], [6],[12]. Many of the validation efforts detailed in the literature address only one system load. i.e., where the deformation of a test specimen is due to either thermal, mechanical or vibration loads occurring at a given time. This research extends the effort to investigate the deformation behaviour of the test tube due to two system loads co-occurring using a nuclear fuel cladding as the case study. The aim of this project was achieved by first developing an extended process in the new flowchart presented in figure 7 of chapter 3, which illustrates the three separate physics domains: the thermal, mechanical, and thermomechanical components. To demonstrate the validation processes in each physics domain required the design and development of experiments and computational models, respectively, and a method for combining the results and measurement uncertainties from the different physics domains to account for the combined effect in the multi-physics domain (thermomechanical physics domain).

As a result, three sets of experiments (thermal, mechanical, and thermomechanical) were performed to investigate the structural displacement response of the specimen when subjected to thermal, mechanical and combined thermal and mechanical system loads and to validate the corresponding computational models following a hierarchy method described by Oberkampf [36].

The thermal physics domain represents the thermal expansion behaviour of the tube subjected to elevated temperatures for physics domain one. In contrast, the mechanical physics domain demonstrates the bending behaviour of the tube when subjected to a constant bending load of 400

Newtons for physics domain two. Finally, the combined thermal and mechanical (thermomechanical) physics domains represent the multi-physics behaviour of the tube under the influence of simultaneous bending and temperature loads and represent physics domain three in figure 7 of chapter 3.

The first section of this chapter describes the image decomposition process employed in this research to decompose the full-field displacement results from the experiment and simulation using Chebychev coefficients. Subsequent sections in this chapter discuss the load-deformation behaviour/relationship observed for the thermal, mechanical, and thermos-mechanical physics domains. The thermal physics domain refers to the thermal expansion of the specimen subjected to elevated temperature loads from ambient to 200^{o}C. In the mechanical domain, the specimen was subjected to a three-point bending load of 400 Newtons. The combined thermomechanical physics domain refers to the simultaneous loading of the tube with thermal and bending system loads.

6.2. Orthogonal Image Decomposition of Full-field Displacement Results

The longitudinal and circumferential displacement images captured with the DIC cameras from the experiments were post-processed using the Istra 4D software supplied with the DIC system. Successful image correlation was performed with facets of 17 x 17 pixels with a grid spacing of 4 pixels. To aid quantitative data comparison between the simulations and measurements , proper orthogonal image decomposition was employed to reduce the full-field displacement fields from an order of 10^2-10^3 data points to 10^1 data points using the Euclid software [147]. As illustrated in figures 3 and 7, the process of representing the displacement fields by a feature vector containing coefficients, also referred to as shape descriptors, was performed independently for the model results (for the different physics domains) to be validated and from the experiment results (from the different physics domains) performed for the purpose of validating the model. Section 6.2 of this chapter describes the image decomposition process.

The image decomposition method is based on polynomial fitting, where 2D data fields with a large number of data points are fully represented by a relatively small set of coefficients, also known as shape descriptors or coefficients. Usually, the shape descriptors are coefficients of the orthogonal polynomial employed to describe the image. As such, a defined set of appropriate polynomials contain the information required to describe the vital features of the image uniquely [148]. This method allowed a significant reduction in the displacement results and facilitated a quantitative comparison between the results from the simulations and the measurements. Chapter two of this thesis covers the description and literature review on image decomposition methods.

In this work, the data describing the displacement fields were treated as images, matrix of grey-scale values, $I_{(I,j)}$, and decomposed using discrete Chebychev coefficients to generate a set of shape descriptors or feature vectors that described the deformed shape of the tube. The resulting image from the reconstruction process is represented by $\hat{I}_{(I,j)}$, as shown in the image decomposition process in figure 43a. The predicted and the measured displacement responses were decomposed using the first 15 Chebychev polynomial terms shown in figure 43 b.

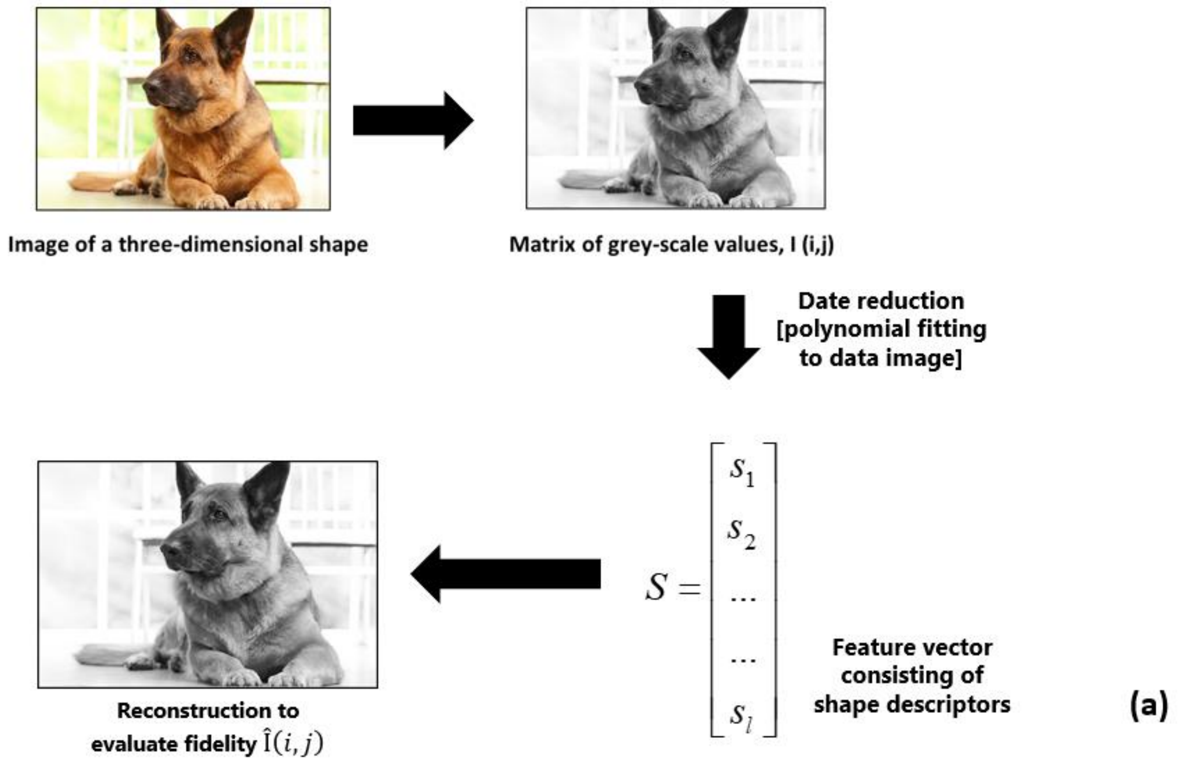

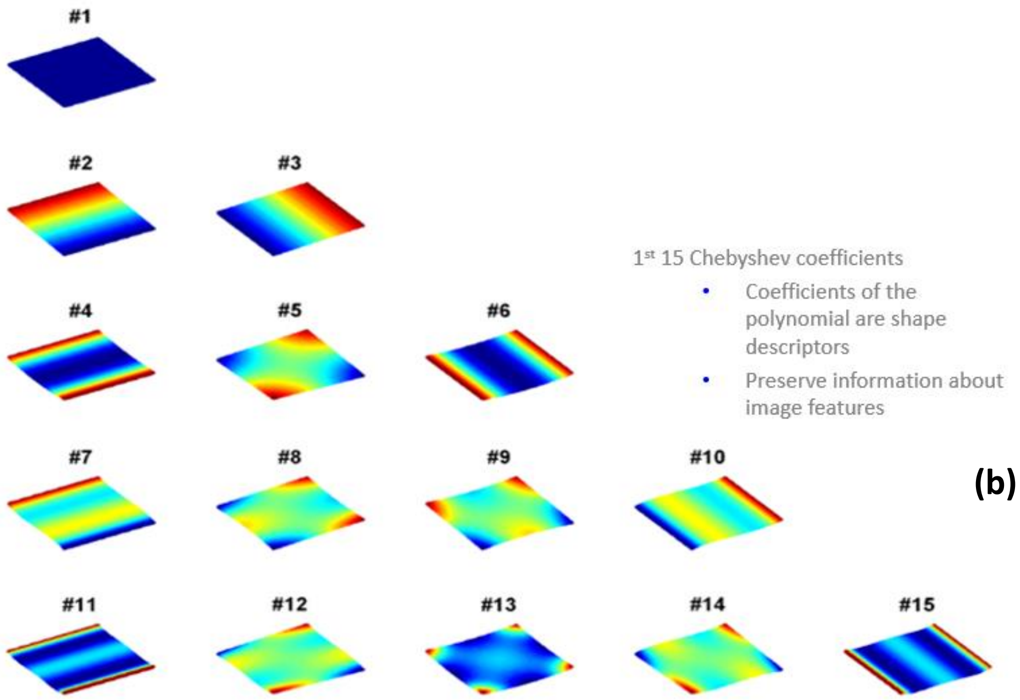

Figure 43: Pictorial illustration of the image decomposition process using Chebychev polynomials (a), and images of the first 15 Chebychev coefficients (b) [56]

In this work, and for validation purposes, it was essential to test the accuracy of the reconstructed displacement fields by assessing the goodness of fit of the reconstruction of the displacement field to the original displacement field using the average squared residual (u_{resid}) in equation 6.1.

$$\mu_{resid} = \sqrt{\frac{1}{N}\sum_{i,j}^{N}\left(\hat{I}(i,j) - I(i,j)\right)^2} \tag{6.1}$$

where $\hat{I}_{(I,j)}$ is the reconstructed value of $I_{(I,j)}$. The average residual is taken as the reconstruction error from the decomposition process, which also constitutes the uncertainty of the shape descriptors. It is recommended in the CEN guide [12] that the reconstruction error must be less than or equal to the minimum measurement uncertainty obtained from the calibration of the measurement instrument detailed in chapter 5 of this thesis. It also suggested that no clusters of residuals between the original and reconstructed data should be greater than three times the average square residual of the data fit. A cluster is defined here as a group of adjacent pixels comprising 0.3% of the total number of pixels in the data from the region of interest.

For a quantitative validation process, the indication of the quality of the experimental data is essential, and the experimental uncertainty $U(S_E)$, is the typical basis for this assessment. The experimental uncertainty for this work is calculated from equation 6.2, which is a combination of the minimum measurement uncertainty, U_{meas}^2, determined from the calibration experiment of the DIC measurement instrument in chapter 5 and the average residuals, $U_{E,}^2$ from the decomposition process.

$$U(S_E) = \sqrt{U_{meas}^2 + U_E^2} \tag{6.2}$$

The process of representing the displacement fields by feature vectors was performed independently for the results from the experiment and the results from the finite element model being validated, as illustrated in figure 7 in chapter 3 of this thesis. However, the identical type and order of shape descriptors were used, which resulted in two feature vectors representing the experiment and the model, respectively. The experimental or minimum measurement uncertainty, $U(S_E)$ evaluated for the thermal, mechanical, and thermo-mechanical components or physics domains, are presented, along with their results in this chapter

The reliability of the results obtained from the experiments was assessed based on the recommendations listed in the literature by Roy and Oberkampf [23] [43] on what validation experiments should include. Some of the essential components of a robust validation experiment provided by Roy and Oberkampf and considered in this work including, (i) a validation experiment must be designed to capture the physics of interest and measure all modelling data, (ii) a validation experiment must measure all response quantities following a hierarchical approach to produce a robust predictive capability of the complete system, and (iii) a validation experiment must be designed to measure components of random and systematic experimental uncertainties or error.

The work reported in this thesis has successfully captured each of the attributes of a good validation experiment listed in the preceding paragraph and is discussed in subsequent sections in this chapter.

As previously mentioned, the following up sections in this chapter discuss the load-deformation behaviour of the specimen subjected to thermal, mechanical and thermos-mechanical system loads. Chapter 7 details the quantitative comparison and validation of the predictions from the computational models against the measurement results.

6.3. Load-deformation relationship of the thermal component

The results of the thermal expansion experiment and the finite element models of the tube subjected to elevated temperature loads from room temperature to 200°C are presented here, representing physics domain one in figure 7 (the extended process validation flowchart). The temperature fields and displacement results were extracted from 1/3 of the tube's surface geometry, approximately 260mm long (of 310 mm length) by 8.2 mm circumference, as shown in figure 44 depicted by the red dotted box.

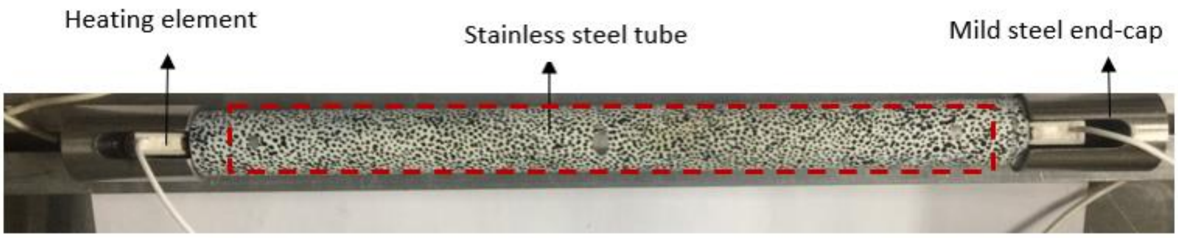

Figure 44: Photograph of the tube showing the region of extracted temperature and displacement results in the red dotted box representing approximately 1/3 of its surface geometry

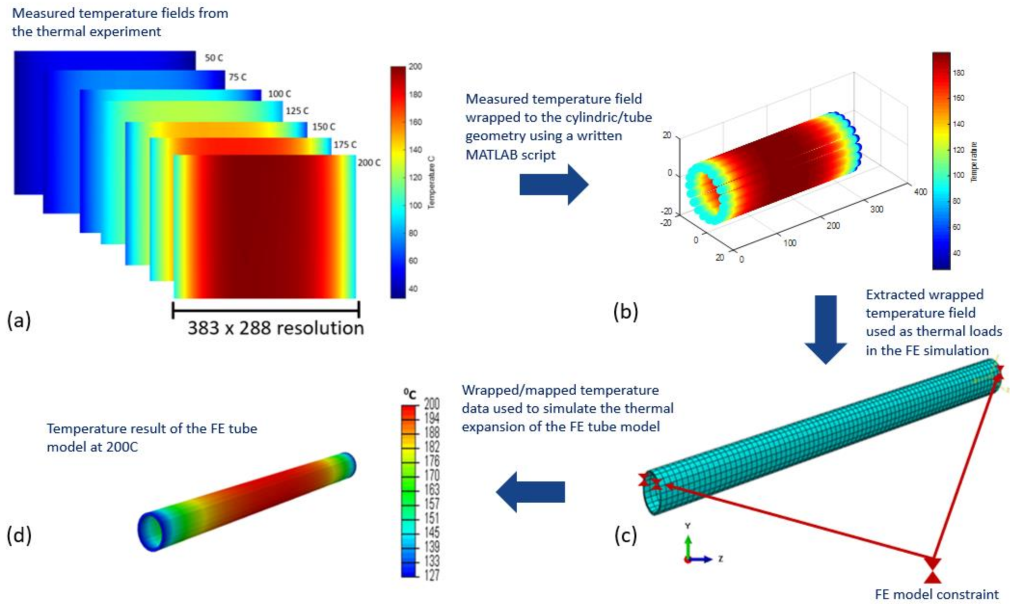

Figure 45 (a) exaggerated view of the temperature fields from 50°c to 200°C obtained from the thermal experiment, (b) represent the temperature field wrapped around the tube's geometry with a MATLAB script, (c) the measured temperature loads are fed to the FE model through the Abaqus software, and (d), shows the resulting temperature of the finite element model at a maximum of 200°C on completion of the simulation

Figure 45 shows the process followed to map the temperature profiles obtained from the experiment to the finite element model to simulate the thermal expansion behaviour of the tube. A cylindrical geometry was developed in MATLAB (figure 45 b) using the stainless steel tube's radius and height (length) in table 2. The height (H = 310mm) and the angle of the cylinder were discretised to allow mapping of the temperature fields to the surface geometry, which generated the temperature loads in the x,y, and z coordinates. This data was fed to the FE model as the system load using the pre-defined temperature interface field in the Abaqus modelling software and subsequently ran to generate the tube's thermal expansion or displacement at elevated temperatures.

The temperature fields from 50 to 200 degrees Celsius are presented in figure 46 for the FE model and the experiment.

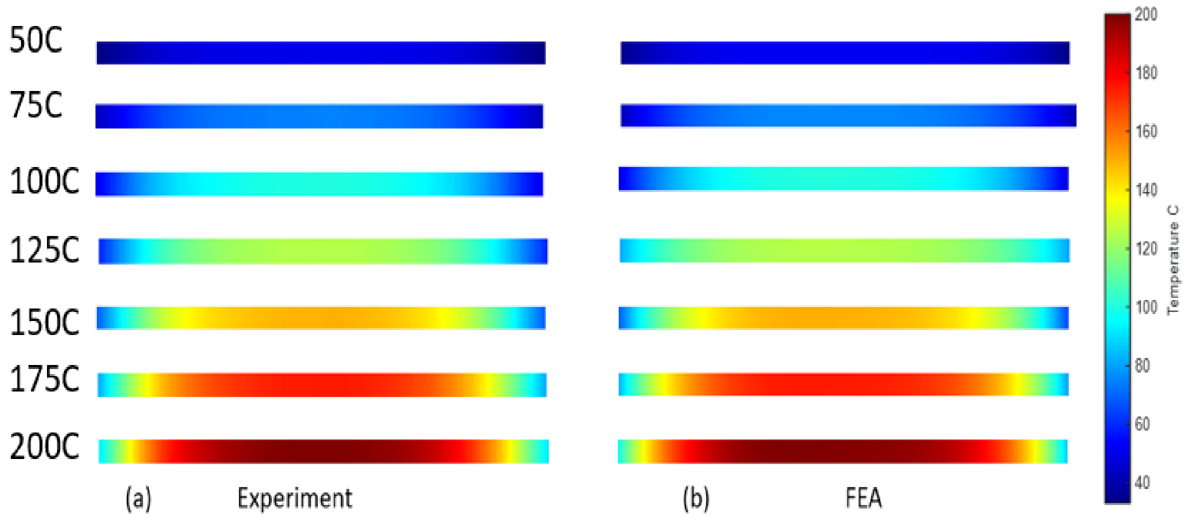

Figure 46: Representation of the full-field temperature maps from the thermal experiment (a) and (b) from the FE analysis at elevated temperatures from 50C to 200C

The temperature fields from the finite element model in figure 46 b are similar to those from the experiment. This virtual comparison was performed to confirm that the temperature fields from the experiment were successfully replicated in the model as a first step to the validation of the results from the computational models.

The temperature variations measured in both the longitudinal and circumferential directions increase with increasing thermal loads, as shown in Figure 46. The axial temperature distribution of the specimen follows a parabolic profile (parabola is a symmetrical, curved, U-shaped graph. The equation of a parabola graph is $y = x^2$). In this study, the longitudinal temperature variations were significantly higher than the circumferential temperature variations because heat energy was conducted away from the middle of the tube, which is an accurate illustration of the second law of thermodynamics (states that "in all energy exchanges if no energy enters or leaves the system, the potential energy of the state will always be less than that of the initial state." This is also commonly referred to as entropy). In the thermal test, the end-caps used for the test were not designed to provide a complete enclosure for the specimen, thus, enabling heat convection in the longitudinal direction of the tube. Also, the powered length of the heating element was 38 mm shorter in length than the specimen (310 mm), which explains the significant temperature variation in the longitudinal direction. The temperature distributions from the thermal experiment were successfully replicated in the finite element model and are comparable, as seen in figure 46.

The longitudinal and circumferential displacement at elevated temperatures, from ambient to 200°C, from the thermal component (measurement and simulation), were also extracted from the region of interest depicted by the red dotted box in figure 44 (experiment) and illustrated in figure 47a and were decomposed using fifteen Chebychev polynomials, which is described in section 6.2 of this chapter. The reconstructed longitudinal and circumferential displacement fields and their shape descriptors (presented in the bar charts), are presented in figures 47 and 48, respectively.

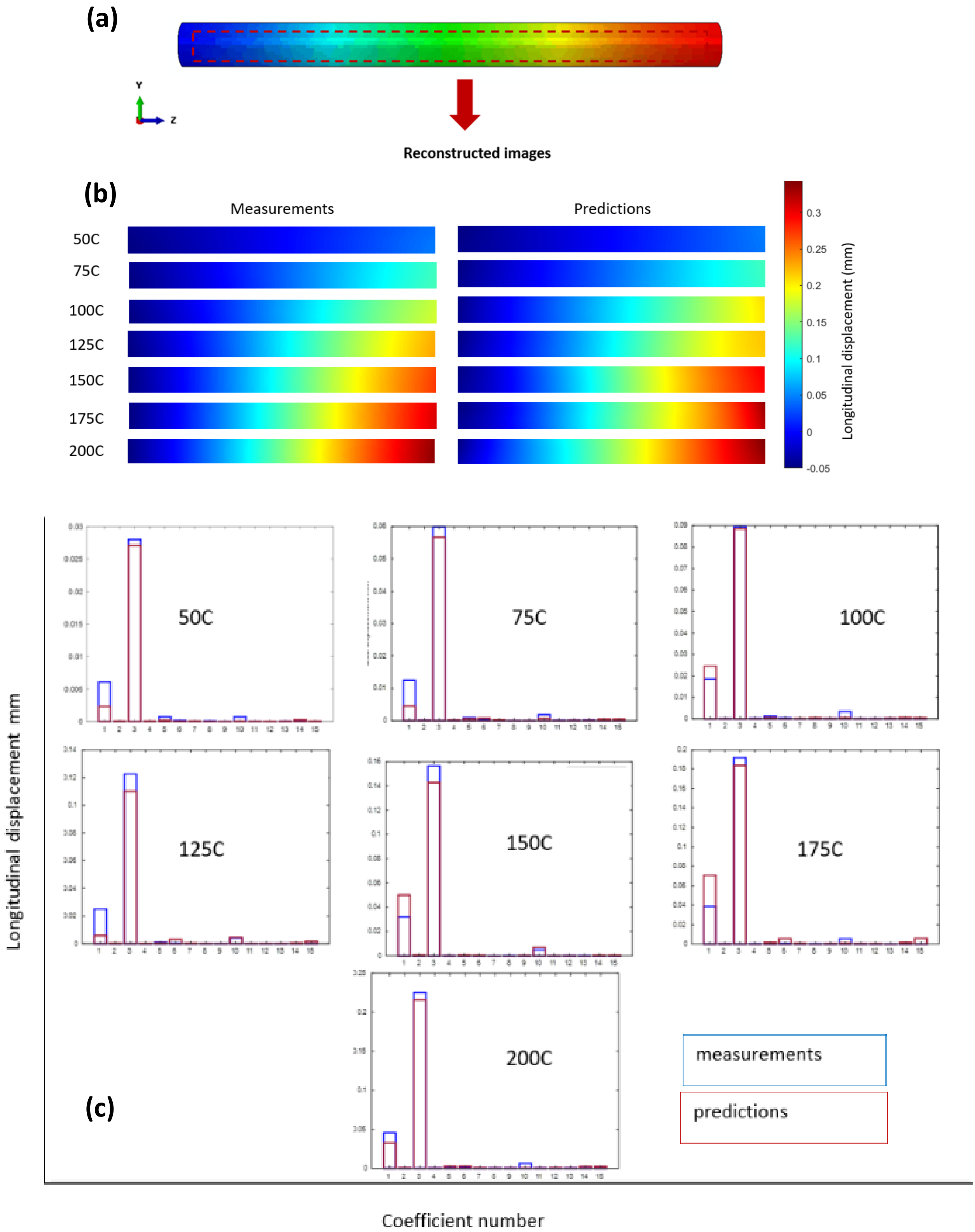

Figure 47: Full-field axial displacement of the tube, (a) showing region of extracted data, (b) extracted displacement fields, and (c) the associated bar charts of the values of the Chebychev coefficients

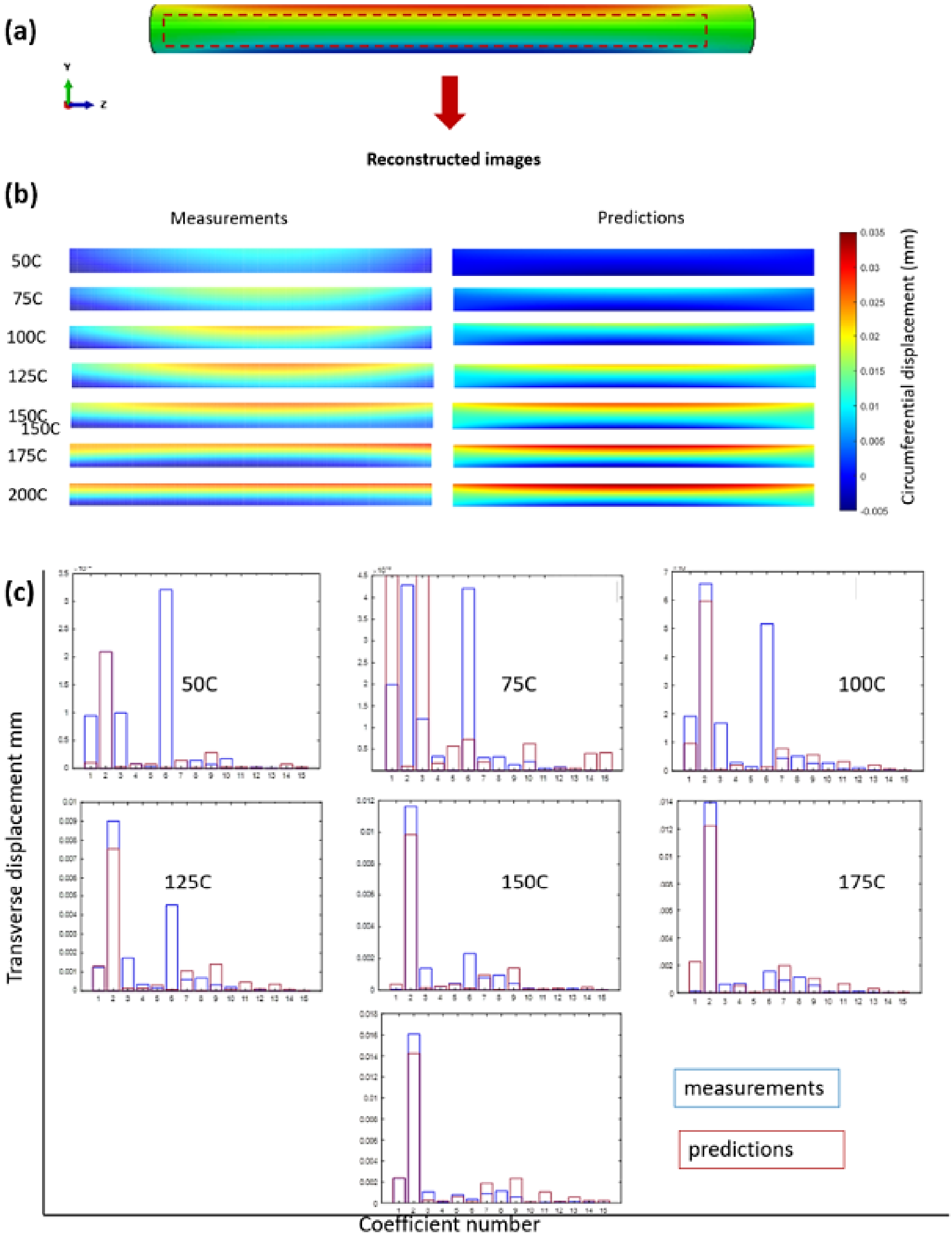

Figure 48: Full-field circumferential displacement of the tube subjected to increasing temperature loads from 50°C to 200°C at 25°C increments, (a) showing region of extracted data, (b) extracted displacement fields, and (c associated bar charts of the values of the Chebychev coefficients

As expected, under the effect of temperature loads, the simply-supported stainless steel tube expanded at a rate directly proportional to the coefficient of the linear thermal expansion. The coefficient of linear thermal expansion is a material property that is indicative of the extent to which a material changes its dimension with temperature changes. i.e. the fractional increase in length per unit rise in temperature. For this research, the coefficient of thermal expansion changes by a fraction of 0.5 for 100^{o}C temperature increments, as illustrated in the plot of figure 49, which is captured in the thermal displacement results. Therefore, this is a significant material property to consider for the analysis of a thermal expansion phenomenon.

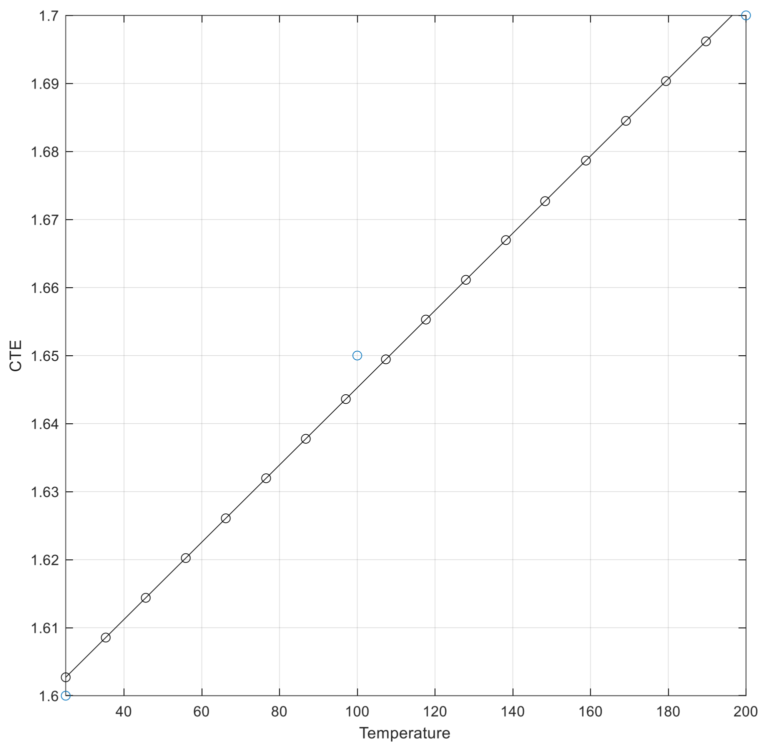

Figure 49 : CTE of the 316l stainless steel tube specimen as a function of temperature [13]

[13] https://www.bssa.org.uk/topics.php?article=139

As seen in the comparison plots of figure 47, the significant shape descriptors describing the longitudinal displacement of the tube specimen are **#1 and #3**. The other shape descriptors are close to zero, having values less than ten percent of the maximum value in the bar charts. The first shape descriptor, #1, is the average magnitude of the data. In contrast, the third descriptor, #3 (over 90% of the sum of the other descriptors), indicates rotation about the x-axis – implying stretching in the longitudinal direction, representing the thermal expansion of the tube. This observed behaviour in the experiment and model accurately illustrates the thermal expansion behaviour of materials [149] [150] subjected to thermal loading in the absence of external constraint; such material will expand at a rate proportionate to the coefficient of thermal expansion.

Longitudinal expansion $$\Delta \mathrm{L} = \alpha . L_{0.} \Delta \mathrm{T} \quad (6.3)$$

Circumferential expansion $$\Delta \mathrm{C} = 2\pi r_{0.} \Delta \mathrm{T} \alpha \quad (6.4)$$

where α is the coefficient of thermal expansion, which varies significantly with temperature, $\Delta \mathrm{L}$, change in length, $\Delta \mathrm{C}$, is the change in circumference, and $\Delta \mathrm{T}$ is the change in temperature. When the expansion is hindered by a surrounding material or by an external constraint, it will result in thermal stress. The magnitude of the stress is such that if applied as an external load, it would produce a strain that is equal to the hindered expansion.

Subsequently, the significant shape descriptors in figure 48 describing the circumferential expansion or displacement are #1 and predominantly #2 from thermal loads of 125°C to 200°C. At lower temperatures, the displacements generated were significantly small and noisy and resulted in unreliable results. Smoothing can be applied to cleanse the data from noise, but that was not performed in this research because the circumferential expansion can be negligible. The second shape descriptor indicates rotation about the y-axis, which represents circumferential thermal expansion. These load curve relationships agree with the fundamental principle that governs the behaviour of unrestrained structures when subjected to thermal effects. The shape descriptors from the thermal analysis representing the predicted and measured longitudinal and circumferential displacement fields exhibited a high degree of linearity relationship with respect to the thermal loads and the corresponding displacement response. The observed linearity behaviour shows that the thermal expansion of the tube is proportionate to the elevated temperature loads, and the displacements were within the elastic domain. Stainless steel tubes of 316l grades have a high deformation temperature between 25°C to 600°C, as illustrated in the stress-strain curve in the literature [151].

6.4. Load-deformation relationship of the mechanical component

The results from the three-point bending experiment and the finite element model of the tube subjected to a constant bending load of 400 Newtons are presented in this section, representing physics domain 2 in figure 7 (the extended process validation flowchart). The mechanical test was designed to idealise the effect of the coolant pressure on a nuclear fuel cladding.

The longitudinal and circumferential displacement fields were extracted from 1/3 of the tube's surface geometry, approximately 260 mm long by 8.2 mm, as shown in figures 50 (experiment), 51 and 52 (simulations) by the red dotted box. The extracted displacement fields were decomposed with fifteen Chebychev polynomials, and the shape descriptors from the reconstruction process are presented in the bar charts in figures 51 and 52.

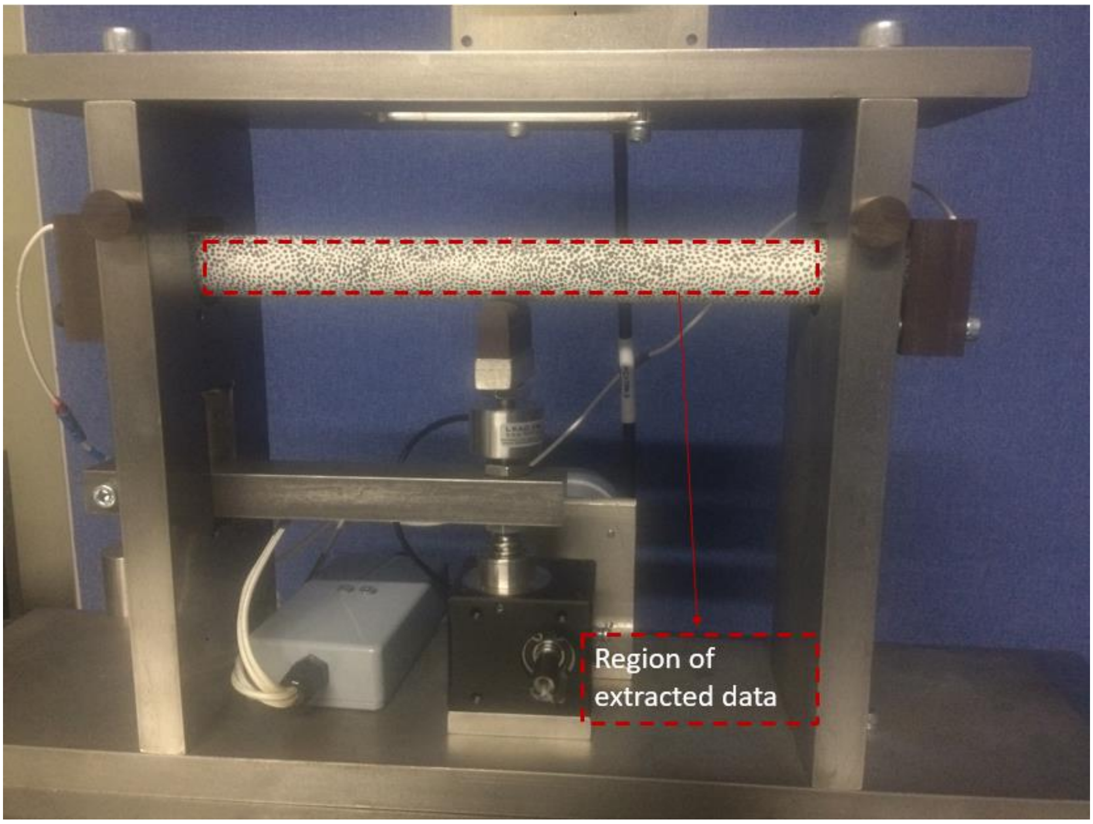

Figure 50: photograph of the three-point bending rig showing the tube subjected to a bending load of 400 Newtons. The region of interest from where the displacement fields were extracted is depicted in the red dotted box

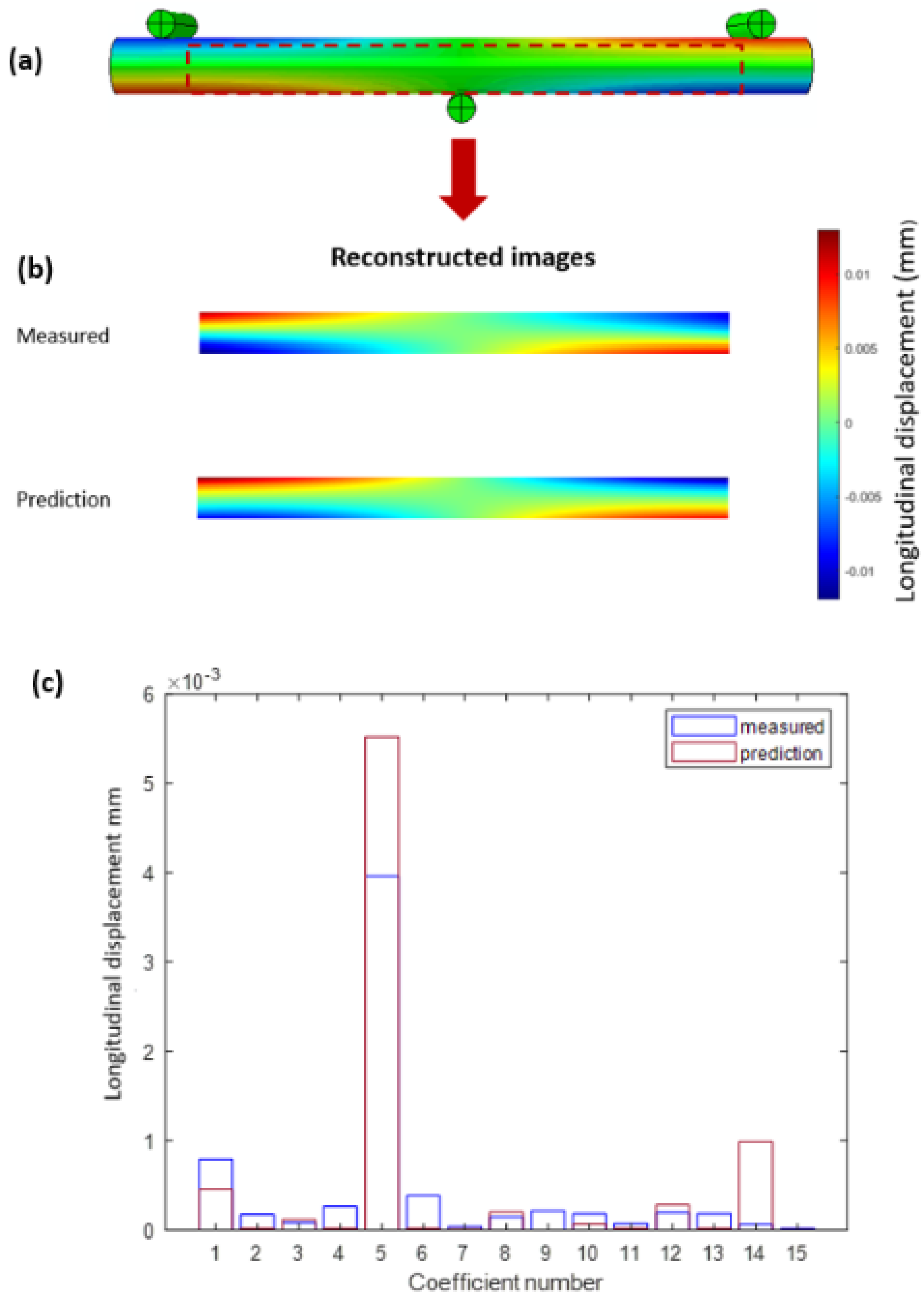

Figure 19: Longitudinal displacement of the tube subjected to a bending load of 400 Newtons, (a) showing region of extracted data, (b) reconstructed and extracted displacement fields, and (c) the associated bar charts showing the Chebychev coefficient values

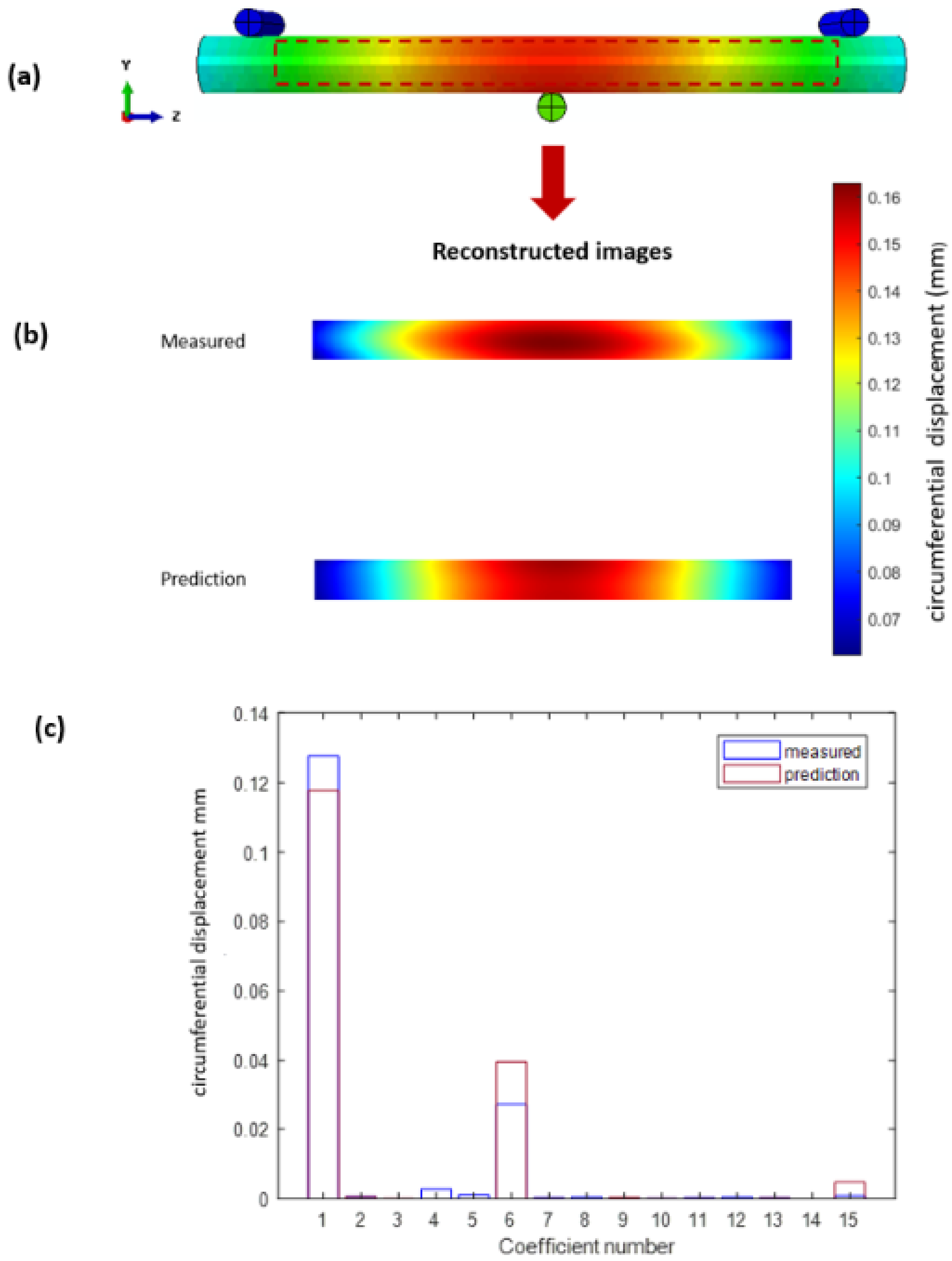

Figure 52: Circumferential displacement of the tube subjected to a bending load of 400 Newtons, (a) showing region of extracted data, (b) reconstructed and extracted displacement fields, and (c) the associated bar charts showing the Chebychev coefficient values

The displacement behaviour observed for the three-point bending of the tube agrees with the first principles for a beam subjected to concentrated bending in a three-point system configuration. For this research, the preferred bending load of 400 newtons was used as this was within the safe elastic limit of the specimen. A maximum average circumferential displacement of 0.153 mm was observed at the mid-span of the specimen for both the simulation and the measurement with negligible longitudinal displacements of approximately 0.01 mm. These results are comparable to the results obtained from the analytical solution from Equations 6.5 and 6.6 and support the elastic beam theory. Longitudinal displacements of points on the neutral axis of the tube specimen, as shown in the displacement field in figure 51b, were negligible, close to zero, while the vertical deflection is primarily due to bending.

$$Y_{max} = \frac{PL^3}{48EI} \quad (6.5)$$

$$x < \frac{L}{2} = \frac{Px}{48EI}(3L^2 - 4x^2) \quad (6.6)$$

where P is the force applied, L is the specimen length, E is the modulus of elasticity, and *I* is the moment of inertia, also known as the second moment of area.

In the case of the mechanical component, the significant shape descriptors describing the longitudinal displacement of the specimen are #1 and #5, while for the circumferential displacements are numbers #1 and #6. The shape descriptor number #6 indicates the bending of the tube in the vertical direction perpendicular to the point of load. Shape descriptor #1 is the magnitude of the displacement response.

The results obtained from the model to be validated and the bending experiment performed for the purpose of validation successfully capture the expected physics behaviour of a simply-supported material subjected to concentrated bending load in a three-point bending configuration and shows a linear-elastic response. Detailed discussion on the displacement output will be covered in chapter 7 of this thesis.

6.5. Load-deformation relationship of the thermo-mechanical component

The combined thermal and mechanical (thermomechanical) measurement and simulation full-field displacement field are presented in this section of this chapter. The thermomechanical component represents physics domain three, referred to as the multi-physics domain for this research, as portrayed in figure 7. The displacement results were extracted from 1/3 of the tube's surface geometry, approximately 260mm long by 8.2 mm, which is the same region of interest (represented by the red dotted box in figures 53 and 54) as the thermal and mechanical components.

For the combined or coupled thermal and mechanical (thermomechanical) component, a constant bending load of 400 Newtons was applied to the mid-span of the specimen in a three-point bending configuration at 25^{o}C increments of temperature from ambient to 200^{o}C. The constraints from the separate physics tests, the thermal and mechanical domains, were carefully replicated in the thermomechanical test by employing instrumentation control measures in the design process (described in chapter 4). It is essential to successfully replicate the boundary conditions and system loads in the combined experiment, as this was a significant aspect of validation experiments involving multi-physics components. Figures 53 and 54 represent the full-field longitudinal and circumferential displacement maps; the reconstructed displacement fields and the associated shape descriptors are presented in the bar charts.

The longitudinal and circumferential thermomechanical displacement maps show a reasonable degree of linearity. i.e. the displacements increase as a function of the applied thermal and mechanical loads. As seen in the displacement fields and bar charts in figure 53, the significant shape descriptors describing the longitudinal displacement of the tube are numbers 1 and 3. The other shape descriptors are close to zero or are less than ten percent of the maximum value. This result is similar to the results obtained from the thermal experiment and model in terms of magnitude and shape, implying that the thermal load drives the displacement of the tube specimen in the longitudinal direction at elevated temperatures. The longitudinal bending of the tube was negligible and close to zero, as expected.

In the case of the circumferential displacement fields presented in figure 54, the significant shape descriptors are numbers 1 and 6. similar to the longitudinal displacement field, a reasonable degree of linearity with respect to the bending and thermal load was observed. However, this was not properly captured by the shape descriptors because the incremental difference between the output generated at increasing thermal loads and a constant bending force from room temperature to 200^{o}C was small to produce a significant effect. However, the linear behaviour was noticeable in the point-data plot discussed in chapter 7 of this thesis. The observable displacement behaviour response was similar to the response obtained from the mechanical domain, where the significant shape descriptors are numbers #1 and #6. The first shape descriptor represents the average magnitude of the data, and the sixth shape descriptor indicates the bending of the tube specimen.

There was approximately an eight to ten percent difference in the circumferential displacement results obtained from the thermomechanical domain in figure 54 with increasing temperatures compared to the results from the mechanical domain in figure 52. However, it is crucial to point out that the mechanical load predominantly drives the tube's vertical displacement and the elastic beam theory supports this behaviour.

The difference in the displacement values between the maximum (200^{o}C) and the minimum (50^{o}C) thermal loads at a constant bending force of 400 Newtons for the circumferential displacement is approximately 0.07 mm, as shown in figure 54. This difference is associated with the thermal effect, i.e., the circumferential thermal expansion of the tube given by equation 6.4.

Under combined thermal and mechanical system loads, the longitudinal displacement produced by the thermal loads tends to reduce the bending moments (bending moment is the reaction induced in a structural element when an external force or moment is applied to the element, causing the element to bend) produced by the bending load. This implies the presence of an interaction effect of the system loads from the different physics domains. It is essential to be aware of any interactions occurring in a multi-physics experiment and/or simulation in order to determine significant sources of errors that can impact the outcome of the solution. Such an exercise is vital to determine how well a computational model of a system simulates the corresponding physical system, which is one of the objectives of this research and is discussed in chapter 7 of this thesis.

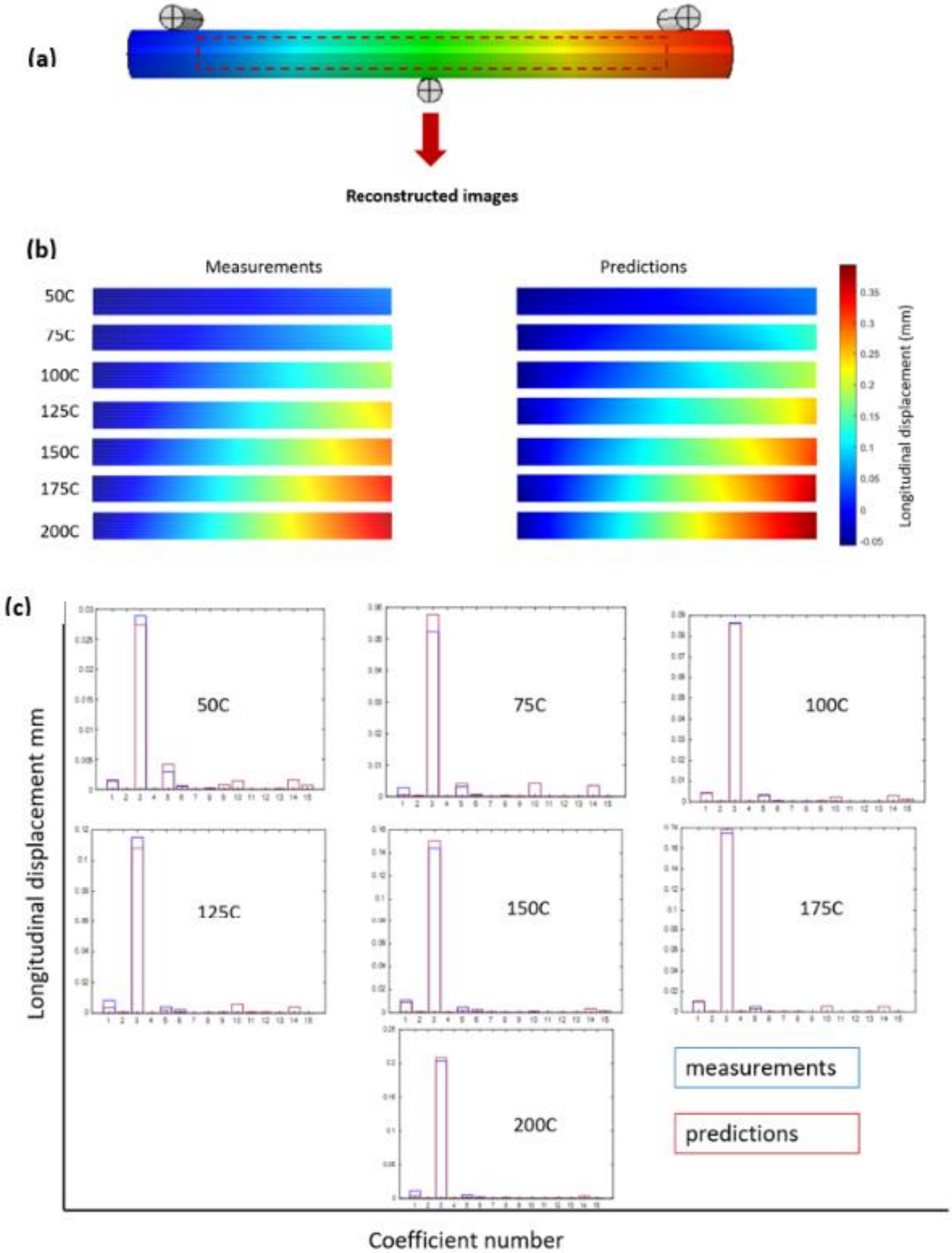

Figure 53: Full-field longitudinal displacement of the tube at a constant bending load of 400 Newtons and elevated temperature loads from 50°C to 200°C, (a) showing region of extracted data, (b) extracted displacement fields, and (c) the associated bar charts of the values of the Chebychev coefficients

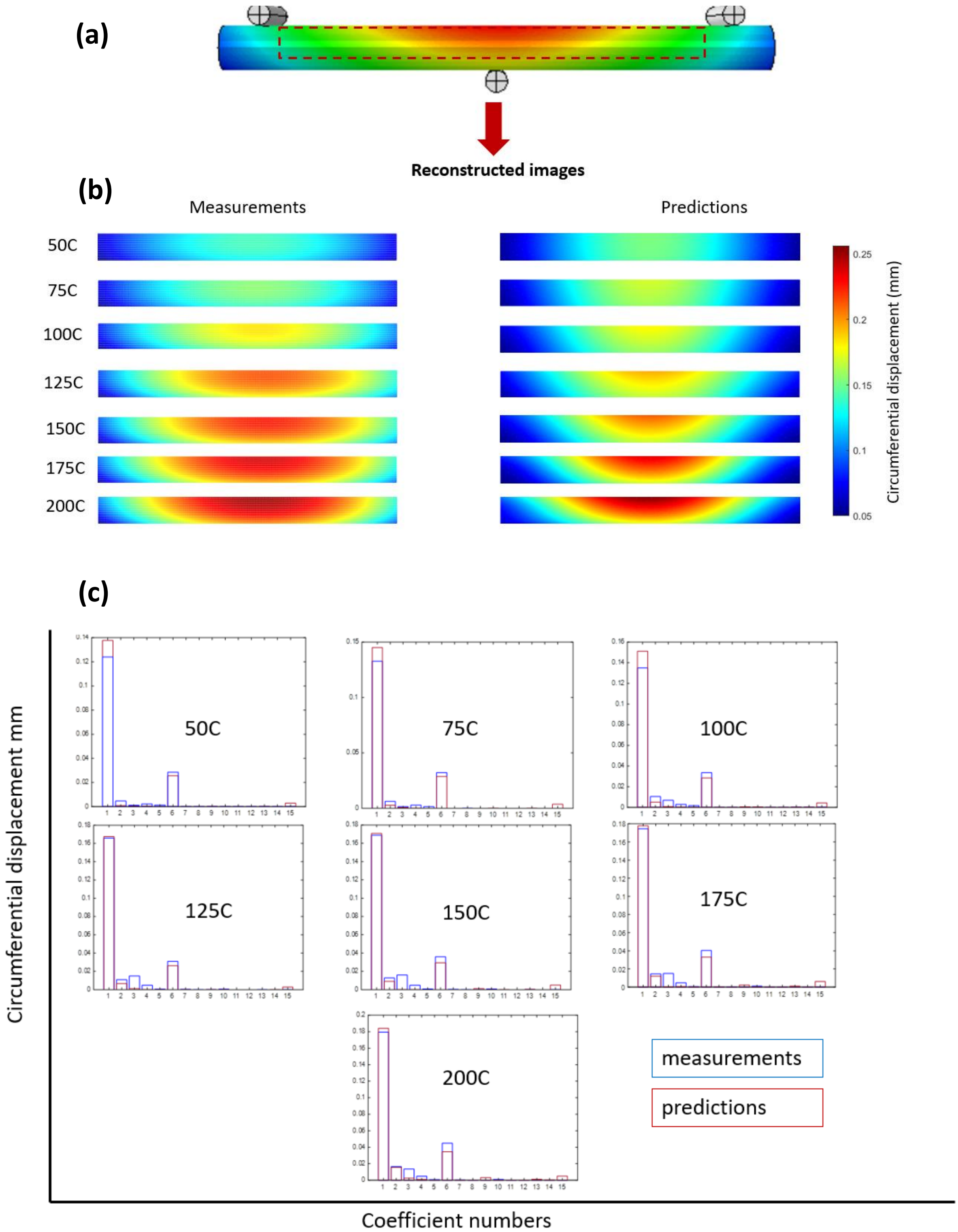

Figure 54: Full-field circumferential displacement of the tube at a constant bending load of 400 Newtons and elevated temperature loads from 50°C to 200°C, (a) showing region of extracted data, (b) extracted displacement fields, and (c) the associated bar charts of the values of the Chebychev coefficients

6.6. Conclusions

The load-deformation relationship of the measurements and simulations is described in this chapter with respect to the first principles. It was essential to understand the different physics behaviour occurring at the thermal, mechanical, and thermos-mechanical domains as a first step toward achieving a multi-physics validation as recommended by Oberkampf [36].

The observed load-deformation behaviour showed the specimen's thermal expansion and the mechanical bending or deflection, which corresponded to the expected physical behaviour and with the analytical equations 6.4 to 6.6 in this chapter. For the thermo-mechanical behaviour, the thermal load drives the longitudinal expansion of the tube, while the interaction of the thermal and mechanical loads was observed for the circumferential displacement. However, the mechanical bending was the significant physics occurring in the circumferential direction of the tube as expected. A good degree of linearity was observed in the displacements with respect to thermal and mechanical loads, and no yielding or fracture was reported in the experiment and computational model.

The next chapter of this thesis focus on the quantitative comparison and validation of the thermal, mechanical, and thermo-mechanical components.

Chapter 7

7. Quantitative Comparison and Validation of the Simulation Results with the Corresponding Measurement Data

7.1. Introduction

This chapter provides a detailed discussion of the results obtained from the experiment and finite element model for the thermal, mechanical, and thermomechanical physics domains with respect to validation. As previously defined in chapter two of this thesis, validation is described as the process of determining the degree to which a mathematical model is an accurate representation of the real world [5]. In the context of this thesis, "real world" refers to the physical system.

As a recap, the significance of the chapter is to meet the objectives of this research, which is to develop an extended approach for the validation of multi-physics computational models using quantitative data obtained from a validation experiment. Validation experiments are carefully designed, executed and analysed to determine how well a mathematical model and its embodiments in a computer code can simulate a well-characterised physical process [43] and play a crucial role in a validation assessment.

The first objective of this research was achieved by developing an enhanced process flowchart in figure 7 of chapter 3 for the validation of multi-physics models drawing on the application of full-field data from separate physics domains. To demonstrate the processes of the enhanced flowchart, three experiments representing the thermal, mechanical, and thermo-mechanical physics domains were designed, built and tested in chapter 4. The full-field displacement longitudinal and circumferential results generated from the experiments and the models are presented in chapter 6, with a discussion on the load-deformation relationship.

In this chapter, the last objective of the research is explored, which is to perform a quantitative validation assessment for the predictions from the computational models against the measurements from the experiments, and to demonstrate the process of merging the system loads and outcomes from the different physics domains (thermal and mechanical), to account for the outcome occurring in the multiple physics domain.

As previously mentioned in chapter 2 of this thesis, an essential element of a validation process and assessment include the quantification of the uncertainties associated with the measurement. Since the measurements obtained from the validation experiment serve as a standard against which the accuracy and reliability of the model output are assessed through comparison, it is essential to include the uncertainties associated with the measured data in the quantitative assessment. The measurement uncertainty associated with the thermal, mechanical and thermos-mechanical components has been determined in chapter 5 of this thesis and reported in this chapter.

The next section of this chapter details the sources of uncertainty in the results, followed by a quantitative comparison of the results from the thermal, mechanical, and thermo-mechanical components. The final section discusses the impact of the research approach on current state-of-the-art validation guidelines and conclusions drawn from the validation assessment.

7.2. Sources of errors and uncertainties in the measurement data

The sources of errors in the experimental and simulation data for the thermal, mechanical, and thermomechanical components can be divided into systematic errors arising from the measurement systems (e.g., the DIC system) and random errors due to the testing environment and boundary conditions. The error and uncertainty process flowchart developed as part of the extended validation process in figure 8 captures all the key sources of errors in the simulation and measurement response.

Since the measurement data obtained from the experiment serves as a standard against which the accuracy of the model output is assessed through comparison, it is essential to include the errors or uncertainties associated with the measured data as the first step toward validation. For simplicity and due to time constraints, this work only considered the errors associated with the measurement system of the response quantity, in this case, the DIC system (which is believed to be the significant source of error in the measurement data), and the error arising from the image decomposition (reconstruction error) were accounted for in the measurement results. The errors associated with other measurement systems in figure 8 of chapter 3, such as the thermal camera and load cell, would not directly influence the results obtained from the experiment but would impact the simulation outcome since it is being used as boundary conditions in the computational model.

In this work, the sources of errors in the measurement response quantity, and the displacement fields, were identified and quantified following a hierarchical approach and the CEN guide [12]. The longitudinal and circumferential displacements presented in chapter 6 of this thesis included the associated uncertainty for each physics domain. The sources of error would differ from one physics domain to another with increasing complexity and the presence of interactions of different physics domains. It has been recommended in [23] that in a robust validation experiment, all sources of significant errors that lead to uncertainty in the measurement response quantity must be available to determine the predictive capability of a corresponding computational model. In this thesis, an error is referred to as the difference between a measured value and the true or expected value of a measurand. In comparison, uncertainty is the expression of the quantified error via interval or confidence bounds.

In this thesis, the systematic errors for the experimental components, such as the error associated with the DIC measurement system, were determined from the calibrated experiment detailed in the CEN guide [12] for optical measurement systems, which is reported in chapter 5 of this thesis. The minimum measurement uncertainty for each physics domain determined from the calibration experiment is listed in tables 5, 6 and 7 for the thermal, mechanical, and thermomechanical physics domains, respectively.

The minimum measurement uncertainty [10], [101] and in the CEN guide [12], $U(S_E)$, is a squared-root combination of the uncertainty from the calibration experiment, U_{meas}^2 , for each system load and the uncertainty generated from the decomposition process, U_E^2, and associated with the reconstructed displacement data, as given in equation 6.2 in chapter 6.

As one progresses from one physics domain to multiple physics domains, the sources of uncertainty increase due to the interactions of the different physics components. In the case of the combined thermomechanical experiment, the sources of error associated with the measurement will increase due to the combined effect of the thermal and mechanical components. As such, the errors or uncertainty in the combined thermomechanical domain is a sum of the minimum measurement uncertainty from the thermal and mechanical physics domains. In other words, the uncertainty from the different physics domains can be superimposed to generate an approximation of the total measurement uncertainty present in the multi-physics domain. The negative effect of employing the combined uncertainty from different physics domains in a validation exercise is that it may lead to large uncertainty bounds causing an inaccurate model prediction to be deemed an accurate representation of the physical system. To mitigate this issue, it is recommended in this thesis that where there are no observable interactions between two or more physics domains, only the uncertainty quantified for the dominating physics domain should be employed in the validation assessment. For example, the longitudinal displacement results of the tube subjected to a combined thermal and bending load obtained from the thermomechanical experiment in figure 53 did not change in value compared to the results obtained when the tube was subjected to only thermal loads from the thermal physics domain. It is recommended that in such a case, only the measurement uncertainty associated with the dominating physics should be employed in the validation assessment.

Table 5: longitudinal and circumferential thermal reconstruction errors, correlation coefficients, minimum measurement uncertainties and the expanded measurement uncertainty for the thermal expansion experiment

Longitudinal displacement	Thermal load	Reconstruction error	Pearson correlation coefficient	Measurement system uncertainty	Expanded minimum measurement uncertainty
	50 °C	0.0015	0.99	0.0036	0.0078
	75 °C	0.0016	0.99	0.0036	0.0079
	100°C	0.0018	0.99	0.0041	0.0089
	125 °C	0.0018	0.99	0.0041	0.0089
	150 °C	0.0020	0.99	0.0061	0.013
	175 °C	0.0022	0.99	0.0061	0.013
	200°C	0.0024	0.99	0.0081	0.017
Circumferential displacement	Thermal load	Reconstruction error	Pearson correlation coefficient	Measurement system uncertainty	Expanded minimum measurement uncertainty
	50 °C	1.38×10^{-4}	0.99	1.38×10^{-4}	3.90×10^{-4}
	75 °C	2.60×10^{-4}	0.99	2.60×10^{-4}	7.35×10^{-4}
	100°C	4.17×10^{-4}	0.99	4.17×10^{-4}	1.18×10^{-3}
	125 °C	5.70×10^{-4}	0.99	5.70×10^{-4}	1.61×10^{-3}
	150 °C	7.35×10^{-4}	0.99	7.35×10^{-4}	2.07×10^{-3}
	175 °C	8.60×10^{-4}	0.99	8.60×10^{-4}	2.43×10^{-3}
	200°C	0.001	0.99	0.0013	2.60×10^{-3}

Table 6: Longitudinal and circumferential mechanical reconstruction errors, correlation coefficients, minimum measurement uncertainties and the expanded measurement uncertainty for the mechanical or three-point bending experiment at a bending load of 400 Newtons

Longitudinal displacement	Bending load	Reconstruction error	Pearson correlation coefficient	Minimum uncertainty	Expanded minimum measurement uncertainty
	400N	1.94×10^{-4}	0.99	1.94×10^{-4}	5.50×10^{-4}
Circumferential displacement	Bending load	Reconstruction error	Pearson correlation coefficient	Minimum uncertainty	Expanded minimum measurement uncertainty
	400N	4.77×10^{-4}	0.99	0.0061	0.012

Table 7: longitudinal and circumferential thermos-mechancial reconstruction errors, correlation coefficients and minimum measurement uncertainties at elevated temperatures and a constant bending load of 400 Newtons

Longitudinal displacement	Thermal load	Reconstruction error	Pearson correlation coefficient	Minimum measurement uncertainty	Expanded minimum measurement uncertainty
	50 °C	4.4e-06	1	0.0036	0.0072
	75 °C	4.7e-06	1	0.0036	0.0072
	100°C	6.1e-06	1	0.0041	0.0082
	125 °C	8.5e-06	1	0.0041	0.0082
	150 °C	1.0e-05	1	0.0061	0.012
	175 °C	1.23e-05	1	0.0061	0.012
	200°C	1.3e-05	1	0.0081	0.016
Circumferential displacement	Thermal load	Reconstruction error	Pearson correlation coefficient	Minimum measurement uncertainty	Expanded minimum measurement uncertainty
	50 °C	1.7 e-05	1	0.0041	0.0082
	75 °C	1.9e-05	1	0.0041	0.0082
	100°C	2.1e-05	1	0.0041	0.0082
	125 °C	2.4e-05	1	0.0061	0.012
	150 °C	2.6e-05	1	0.0061	0.012
	175 °C	2.9e-05	1	0.0061	0.012
	200°C	3.3e-05	1	0.0061	0.012

.

The relative minimum measurement uncertainty at 200ºC associated with the longitudinal displacement for the thermal and thermomechanical measurements at elevated temperatures was less than seven percent of the maximum displacement value with respect to figures 47 and 53**.** In comparison, the relative minimum measurement uncertainty for the circumferential mechanical displacement is approximately five percent with respect to figure 52. These values are small and would result in narrow confidence bounds in the scatter comparison plots presented in chapter 7 of this thesis.

In the combined thermomechanical experiment and simulation presented in this thesis, it was established that the dominating physics occurring in the longitudinal direction of the specimen at elevated temperatures and at a constant bending load was the thermal expansion or displacement, as seen in figure 53, which was comparable to the displacement obtained from the thermal experiment in figure 47. The longitudinal mechanical bending that resulted from the external load was negligible and made no significant change to the output, as the difference between the longitudinal displacement results from the thermal and thermo-mechanical domains was insignificant (approximately zero). This observation implies there was little or no interaction (no coupling) between the thermal and the mechanical longitudinal loads. In such a case, the sources of errors associated with the combined thermomechanical measurement include the squared root sum of the minimum measurement uncertainty evaluated from the thermal calibration experiment, the reconstruction error from the orthogonal image decomposition, and may include the variability in the repeat thermal tests.

In the circumferential displacement for the combined thermomechanical component, it was observed that the mechanical bending of the tube was the dominating physics, as shown in figure 52. However, the circumferential thermal expansion of the tube was also significant as it resulted in an approximately 28% increase of the maximum circumferential displacement, which can be determined from the difference between the maximum circumferential displacement of the mechanical and thermo-mechanical values in figures 52 and 54, respectively.

Therefore, combining the minimum measurement uncertainty associated with the mechanical and thermal components was reasonable to account for the total measurement uncertainty associated with the circumferential thermomechanical displacement. The total measurement uncertainty for the circumferential displacement is approximately thirteen percent of the maximum displacement. The uncertainty results for the different physics domains are presented in chapter six of this thesis.

Other sources of errors that could be included are listed in figure 8 in chapter 3 of this thesis, which includes the inherent variability of the test specimen and the errors associated with the measurement of the system loads, i.e., the thermal and mechanical bending loads. On the other hand, the errors associated with the measurement of the system loads or boundary conditions, i.e., temperature and the bending loads, can be included and obtained from the manufacturer's calibration certificates. For example, the uncertainty of the thermal camera for temperature measurement was ±2°C or ±2%. However, these uncertainties were not accounted for in the results presented in chapters 6 and 7, as there were negligible compared to the systematic uncertainties, which increase with increasing system loads, as shown in tables 5 to 7.

In summary, it was observed that the systematic uncertainty (measurement uncertainty) associated with the DIC measurement system increases as a function of increasing system loads (tables 5 to 7). This observation was also noticeable in the reconstruction error calculated from the image decomposition of the displacement field, which was obtained from the thermal, mechanical, and thermomechanical physics domains. The reconstruction error for the thermal and thermomechanical displacement fields increases with temperature increments. This could imply that at elevated temperatures, the shape of the displacement field becomes slightly more complex as the tube expands longitudinally and circumferentially. Therefore, this work has demonstrated that the uncertainty associated with a particular measurement data for a specified system load would differ when the system load is increased or changed. Therefore, it is essential to capture these differences by quantifying the errors for each system load independently, as performed in this work. This would aid in generating a robust and reliable uncertainty quantification analysis.

The next section of this chapter employs the measurement uncertainty quantified in chapter 5 and listed in tables 5 to 7 to assess the reliability of the measured data and to evaluate how close the simulations from the different physics domains represent the corresponding measurements.

7.3. Quantitative comparison of the simulation and measurement results

The longitudinal and circumferential simulation results to be validated from the thermal, mechanical, and thermo-mechanical components were compared against the corresponding measurement results to ascertain the reliability of the simulations. The goal of a validation assessment is to credibly establish whether the level of agreement between the prediction from a simulation and the measured data from a carefully designed experiment satisfies the specified requirements for the intended use of the model. Knowledge of the measurement uncertainty is essential to establish how well a model prediction simulates the corresponding physical system and aids a quantitative comparison.

According to the CEN guide, the shape descriptors representing the displacement fields for the identical region of interest obtained from the model being validated and the experiment performed to validate the model can be quantitatively compared by plotting the former as a function of the latter. For a perfect correlation, all the resultant shape descriptor data points from the simulation and measurement would lie perfectly on a straight line of a gradient of unity. However, this is often unusual in practice due to noise in the data, the presence of errors or the model is not a good representation of the reality of the physical experiment. The model is considered to be a good representation of the experiment if all the data points were within a confidence bound or area defined by the measurement uncertainty.

$$S_M = S_E \pm U(S_E) \tag{7.1}$$

where S_M and S_E are the shape descriptors representing the displacement fields from the model and experiment, respectively, and $U(S_E)$ is the uncertainty associated with the feature vector describing the displacement from the experiment, which also includes the experimental or calibration uncertainty defined by equation 6.2.

7.3.1. Comparison of the thermal component

For the thermal component, the shape descriptors representing the longitudinal and circumferential displacements from the model were plotted against the shape descriptors from the experiment in figures 55 and 56, employing the comparison approach recommended in the CEN guide. The red dotted lines indicate the area defined by equation 7.1 on the plot of figures 55 and 56. It is evident from the plots that the majority of the significant shape descriptors data points illustrated by the black circle fall on or within the acceptable confidence bounds, implying that the model is a good representation (not a perfect representation) of the physical reality. The data points that are scattered outside the uncertainty bounds in figure 56 may be due to noise as the circumferential displacements at a lower temperature is very small. Figure 57 shows the circumferential comparison plot at 200°C, and it can be observed that at this temperature, all the displacement falls inside the uncertainty bounds depicted by the red dotted lines. The area defined by the red dotted lines and illustrated in the comparison plots represents the expanded minimum measurement uncertainty obtained at 200°C in table 5.

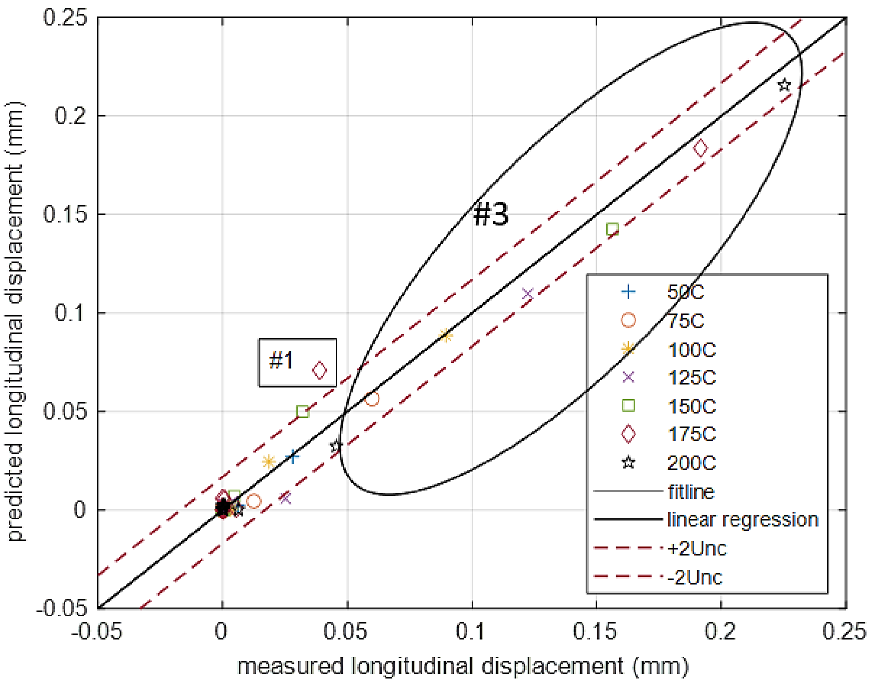

Figure 55: plot of the longitudinal thermal expansion showing the comparison between the predictions and the measurements at elevated temperatures from 50°C to 200°C at 25°C increments with the associated expanded minimum measurement uncertainty at 200°C depicted by the red dotted line

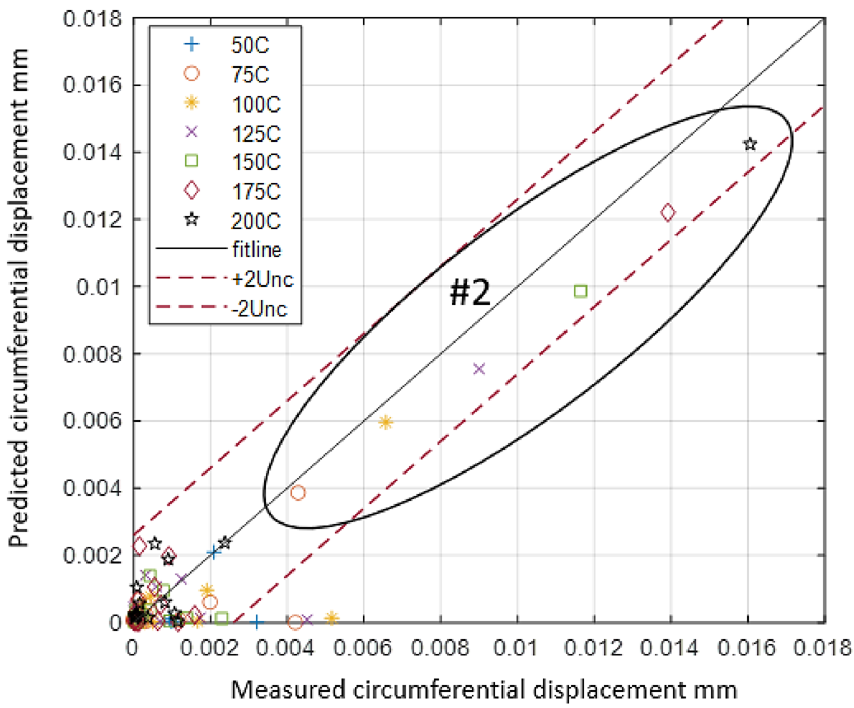

Figure 56: circumferential thermal expansion plot showing the comparison between the predictions and the measurements at elevated temperatures from 50ºC to 200ºC at 25ºC increments, with the associated expanded minimum measurement uncertainty at 200C depicted by the red dotted line in both plots

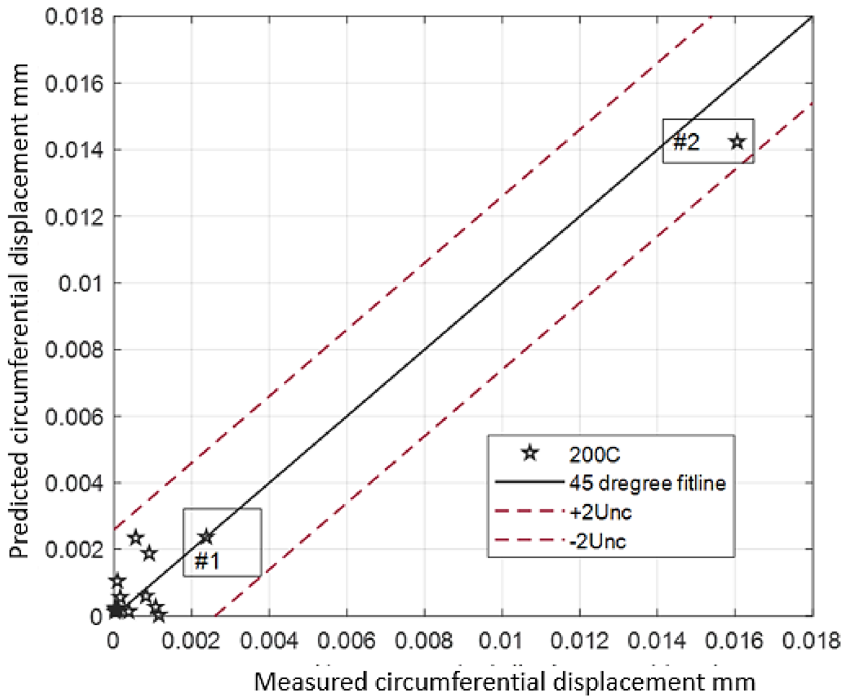

Figure 57: circumferential thermal expansion plot showing the comparison between the predictions and the measurements at temperatures of 200ºC, with the associated expanded minimum measurement uncertainty at 200C depicted by the red dotted line in both plots

For a more robust comparison, the minimum measurement uncertainty was calculated for each temperature load from 50^{o}C to 200^{o}C, as listed in table 5. As previously mentioned, the measurement or experimental uncertainty increases with increasing system loads. As such, it was reasonable to account for this change at specific validation points using error bar plots. The error bar plots in figure 58 represent the thermal expansion of the tube in the longitudinal direction. The significant shape descriptors, #1 and #3, in the feature vector obtained from the simulation and experiment, were plotted as a function of the elevated temperature loads (top plot in figure 58). As illustrated in the error bar plot, an overlap between the simulation and measurement displacement data points for the #3 shape descriptor was observed between temperature loads of 50^{o}C to 100^{o}C, indicating a perfect agreement. At temperature loads of 125^{o}C and 150^{o}C, the simulation data points were observed to be at the lower ends of the measurement uncertainty, implying that the relative difference between the simulation and the measurement data points were equal to or greater than the minimum measurement uncertainty. However, this was not a big difference and could be attributed to a decomposition error or bias. These differences change at 175^{o}C and 200^{o}C, as the simulation data points representing the #3 falls within the error bar indicating a good agreement. The bottom comparison plot, figure 58b, for the #3 shape descriptor, shows a good relationship between the simulation and the measurement with a RMSE of 0.0042. This value is approximately two percent of the maximum displacement value represented by the #3 shape descriptor, which also reinforces a good correlation between the simulation and the measurement. The #1 shape descriptor was not included in figure 58 due to its relatively small values compared to the measurement uncertainty determined for the thermal measurement. The key was to focus on significant displacement fields.

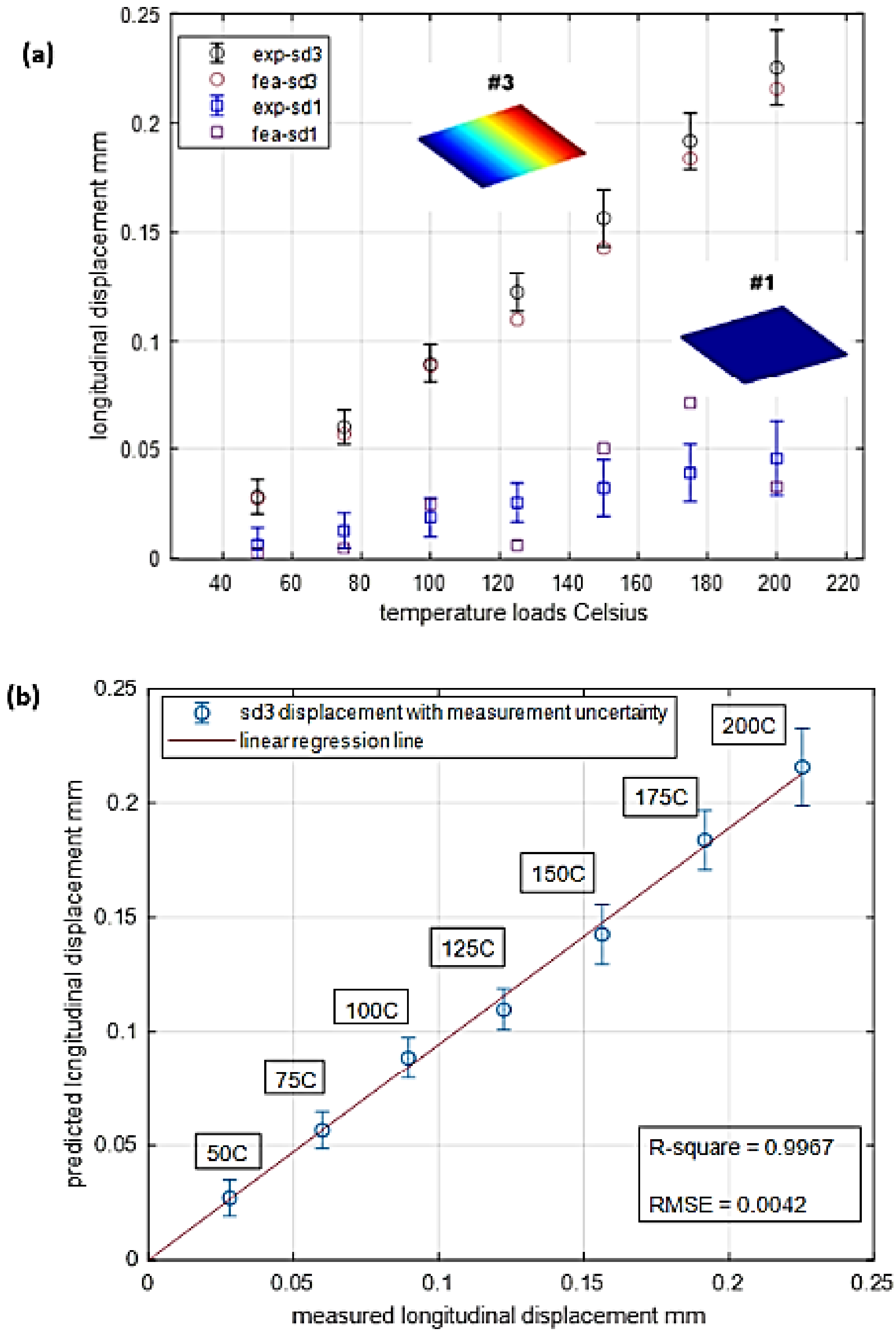

Figure 58: Errorbar plots of the longitudinal thermal expansion showing the measurement and predictions against increasing temperature loads from 50°C to 200°C at 25°C increments for the significant coefficients #1 and #3 (a), and (b) showing the comparison between the predictions and the measurements at elevated temperatures for the predominant shape descriptor #3 along with the linear regression fit

7.3.2. Comparison of the mechanical component

For the mechanical component, the shape descriptors representing the longitudinal and circumferential displacements from the model were plotted against the shape descriptors from the experiment in figure 59, employing the comparison approach recommended in the CEN guide. The comparison approach recommended in the CEN guide was acceptable for the validation of the mechanical component because it only involves a constant load, unlike the thermal component, which involves increasing system loads. As previously mentioned, increasing system loads would generate increasing systematic uncertainty that must be accounted for in the comparison plot. However, since the mechanical component, the three-point bending of the tube was performed with a constant bending load of 400 Newtons, the uncertainty quantified for this measurement setup was used to assess the reliability of the measurement and validation of the corresponding computational model. The mechanical measurement uncertainty is presented in table 6.

In the mechanical physics domain, a good agreement was observed between the predictions from the simulation and measured from the experiment for the longitudinal and circumferential displacement fields, as shown in figure 59. All the data points representing the simulation and measurement fall within the minimum measurement uncertainty bound depicted by the red dotted lines in figure 59. Therefore, it is reasonable to assume that 100% of the displacement data falls within the area defined by the minimum measurement uncertainty, and as such, the model is deemed a good representation of the physical reality. This outcome also implies that the error between the model prediction and the measurement is significantly lower than the minimum measurement uncertainty obtained for the mechanical physics domain.

The plot in figure 60 also illustrates a good correlation between the prediction and the measurement for both the longitudinal and circumferential displacement fields with R2 values of 0.96 and 0.99, respectively. The Root Mean Squared Error (RMSE) for the longitudinal and circumferential displacements at 400 Newtons bending loads are 0.0008 and 0.004, respectively. These values are relatively small compared to the maximum measured longitudinal and circumferential displacement and result in uncertainty of approximately less than 10 percent.

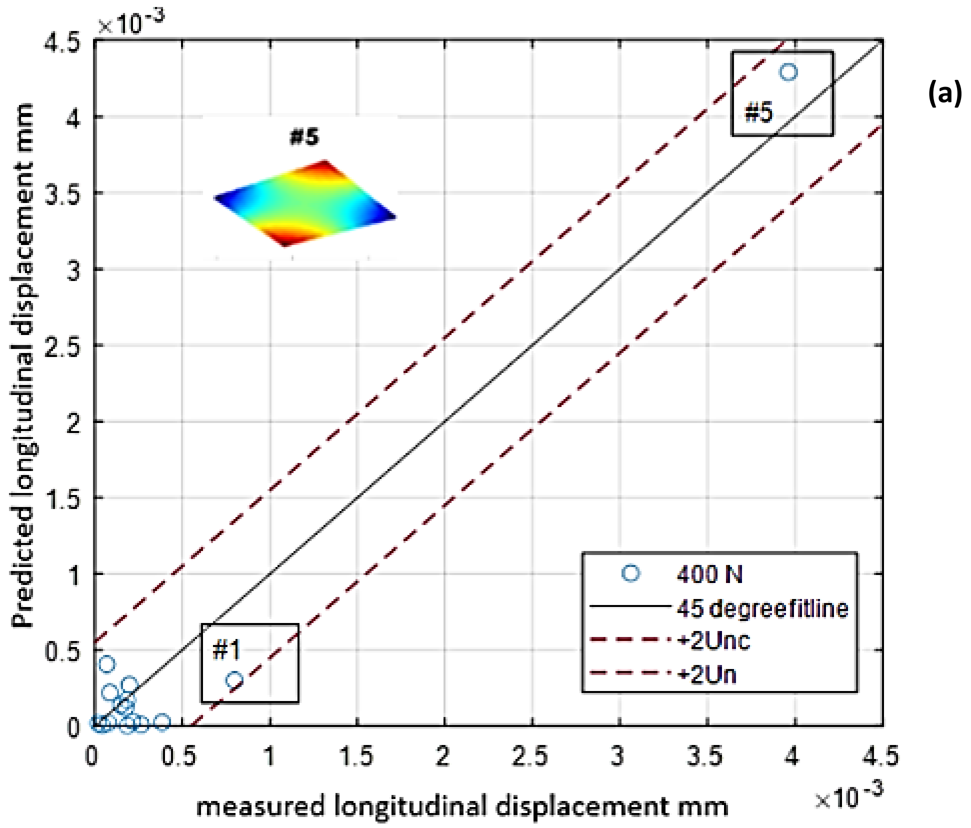

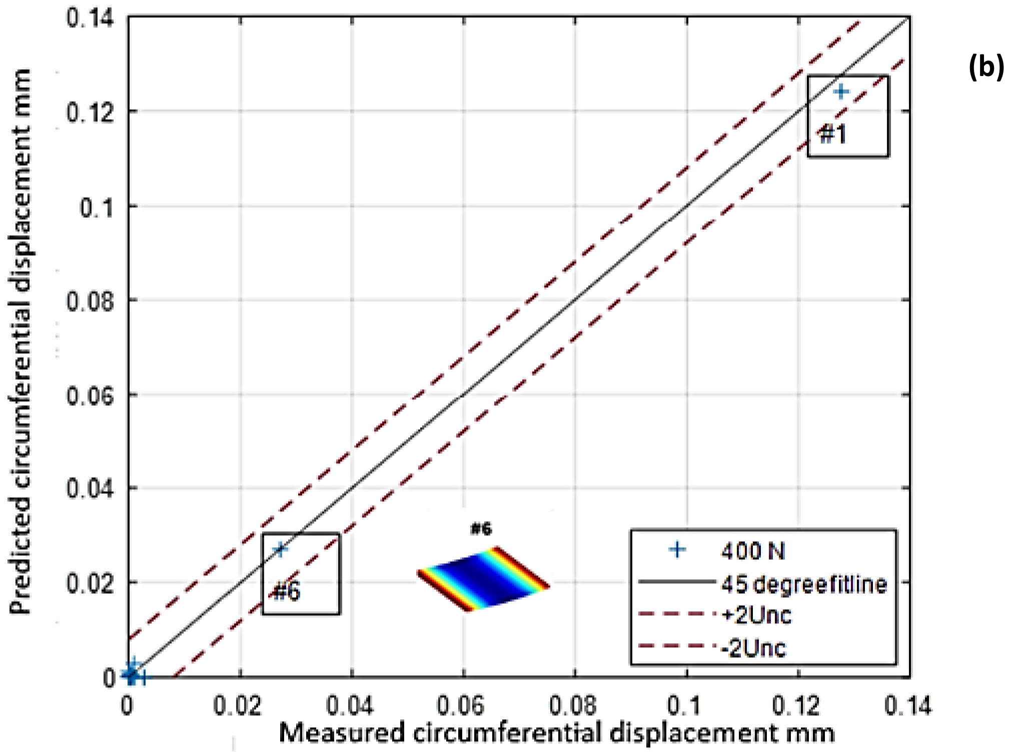

Figure 59: Comparison plots showing the measurements and the predictions, (a) the longitudinal and (b) the circumferential displacement of the tube subjected to a bending load of 400 Newtons with the associated confidence bounds depicted by the red dotted lines, which is a representation of the minimum measurement uncertainty

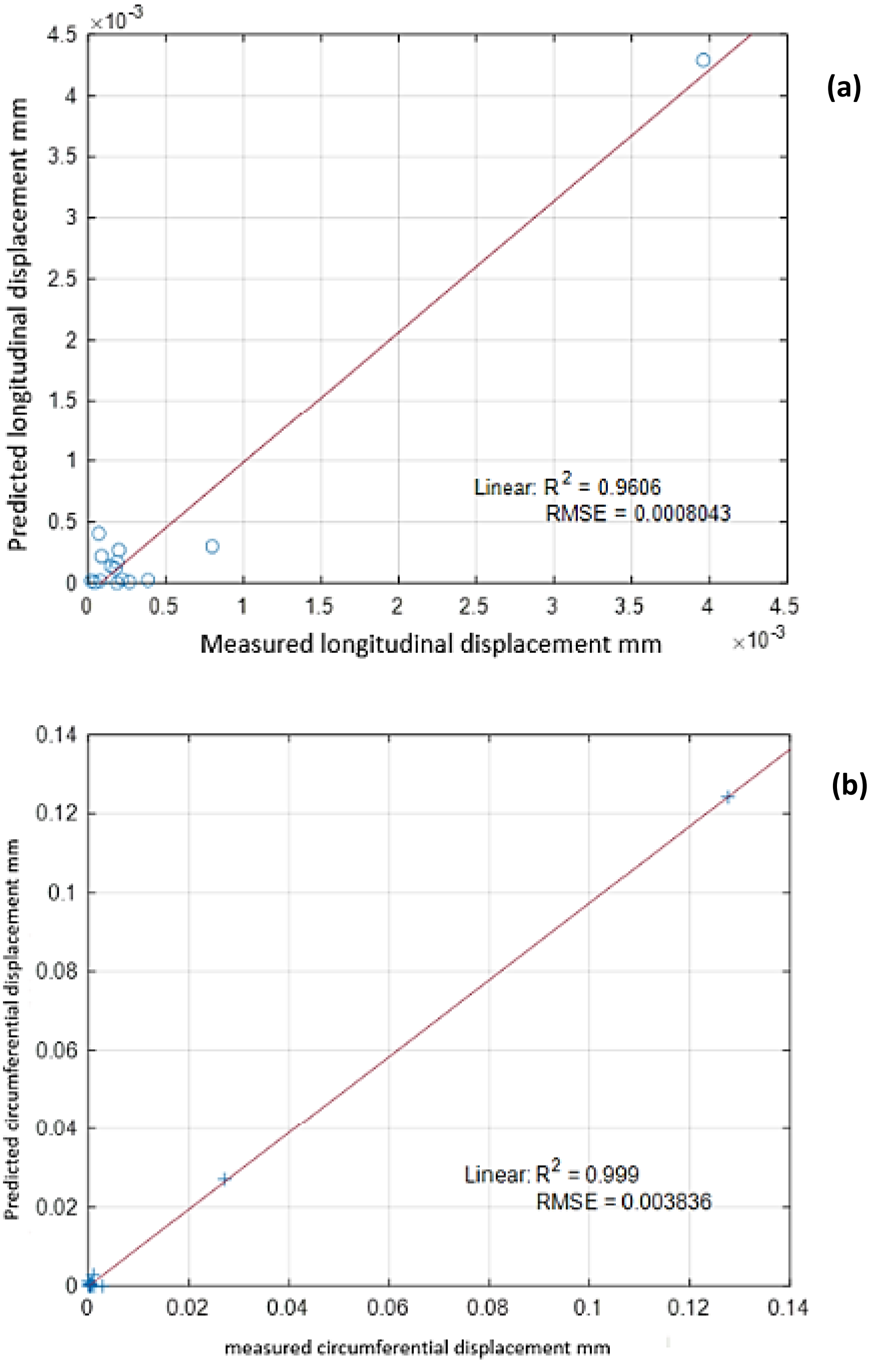

Figure 60: Comparison plots of the measurements and predictions showing (a) the longitudinal and (b) the circumferential displacement of the tube subjected to a bending load of 400 Newtons with the associated linear regression depicted by the red lines and the root mean squared error

7.3.3. Comparison of the thermo-mechanical component

The process taken to compare the predictions and the measurements for the thermal physics domain was employed in the thermomechanical physics domain. Firstly, the shape descriptor data points representing the simulation and the measurement from the combined thermomechanical experiment and the coupled physics model were plotted against each other in figures 61 and 62. The red dotted lines in the plots are representations of the value of the minimum measurement uncertainty obtained at the maximum temperature load of 200°C. A good agreement was observed for the longitudinal, and circumferential displacement fields as all the data points fall within the area defined by the minimum measurement uncertainty. The significant shape descriptor for the simulation and measurement in the longitudinal displacement plot of figure 61 is #3. In contrast, the significant shape descriptor for the simulation and the measurement in the circumferential displacement plot of figure 62 are #1 and #6.

For a more robust comparison, the minimum measurement uncertainty was calculated for each temperature load from 50°C to 200°C, as listed in table 5. As previously mentioned, the measurement or experimental uncertainty increases with increasing system loads. As such, it was reasonable to account for this change at specific validation points using error bar plots. The error bar plots in figure 63 represent the thermal expansion of the tube in the longitudinal direction. The significant shape descriptors, #1 and #3, in the feature vector obtained from the simulation and experiment, were plotted as a function of the elevated temperature loads (figure 63a). As illustrated in the error bar plot, an overlap between the simulation and measurement displacement data points for the #1 and #3 shape descriptors was observed for all temperature loads, indicating a perfect agreement. The comparison plot in figure 63b is for significant, the #3 shape descriptor for the prediction and the measured displacements. The comparison plot shows a good correlation (R^2 of 0.99 - R-squared (R^2) is a statistical measure that represents the proportion of the variance for a dependent variable that's explained by an independent variable or variables in a regression model) relationship between the simulation and the measurement with a RMSE of 0.015. This value is similar to the value of the minimum measurement uncertainty obtained at 200°C for the thermo-mechanical measurement setup and is approximately five percent of the maximum displacement value.

The plot of figure 63 also shows a high degree of linearity with respect to the thermal loads for the significant shape descriptors.

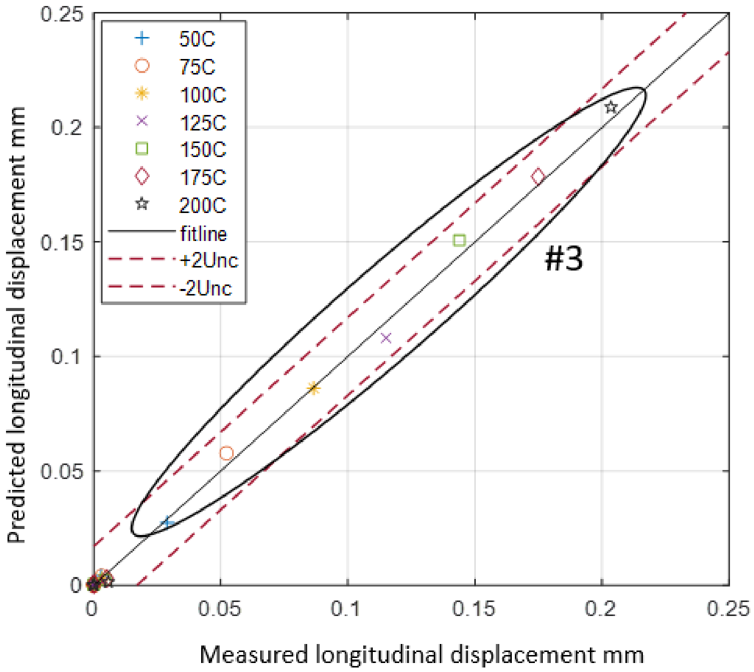

Figure 61: Comparison plots showing the longitudinal measurements and the predictions of the displacement of the tube subjected to a constant bending load of 400 Newtons and elevated temperature loads from 50ºC to 200ºC with the associated confidence bounds depicted by the red dotted lines, which is a representation of the measurement uncertainty at 200ºC

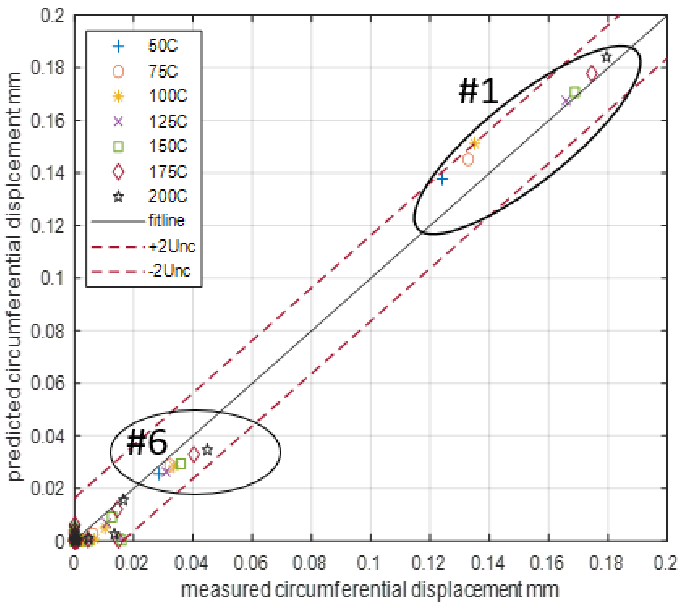

Figure 62: Comparison plots showing the circumferential measurements and the predictions of the displacement of the tube subjected to a constant bending load of 400 Newtons and elevated temperature loads from 50ºC to 200ºC with the associated confidence bounds depicted by the red dotted lines, which is a representation of the measurement uncertainty at 200ºC

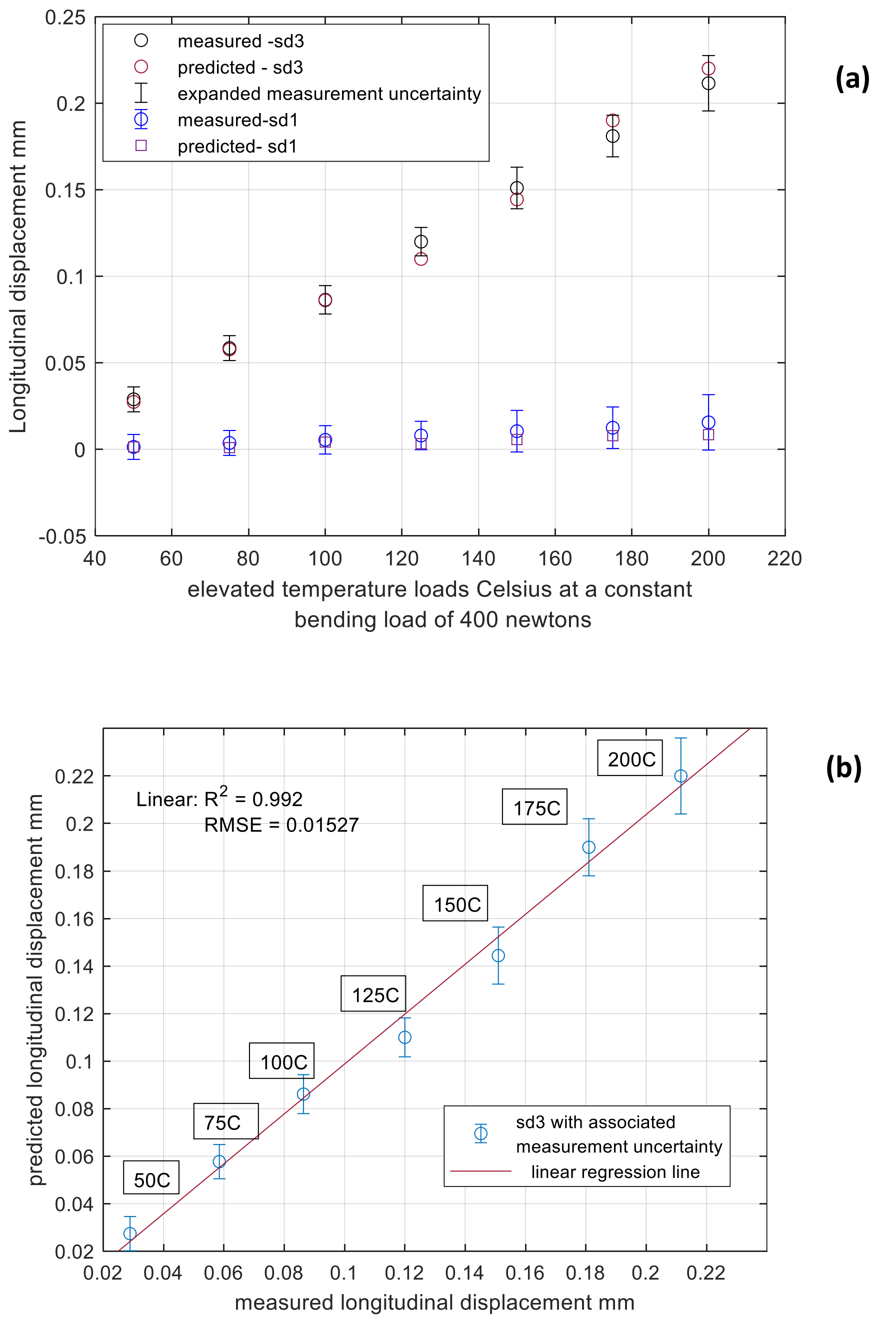

Figure 63: Errorbar plots of the longitudinal displacement showing the measurement and predictions against elevated temperature loads from 50°C to 200°C at 25°C increments and a constant bending load of 400 Newtons for the significant shape descriptors, #1 and #3 (a), and (b) showing the comparison between the predictions and the measurements at elevated temperatures for the predominant shape descriptor #3 along with the linear regression fit

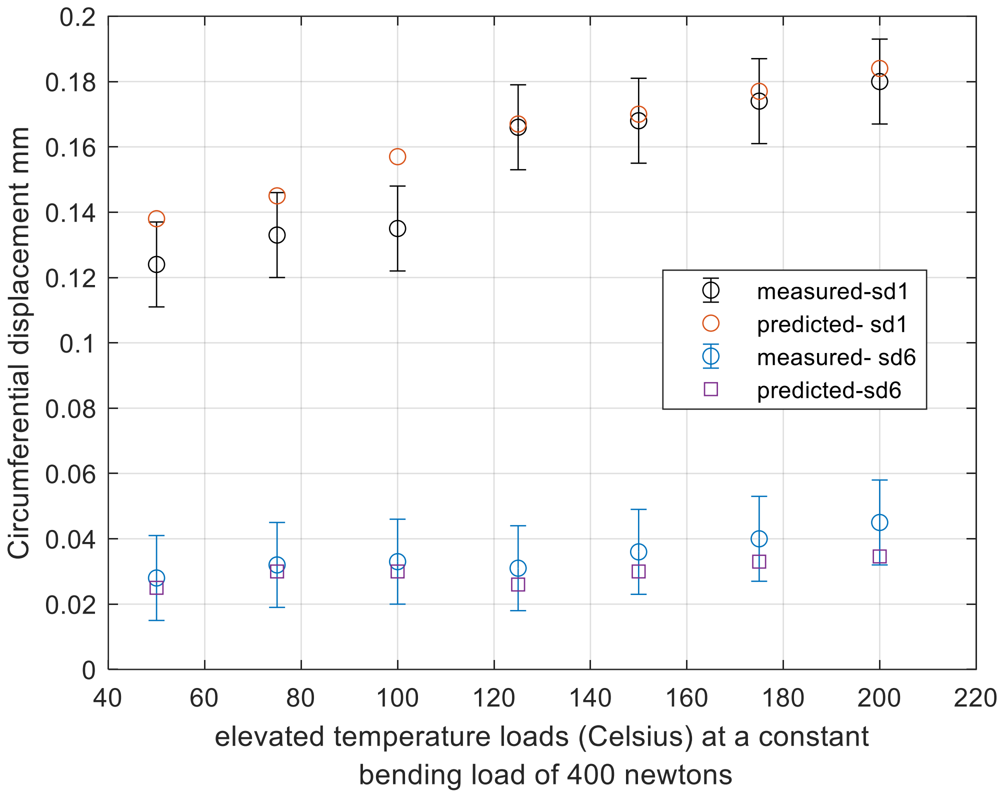

Figure 64: Errorbar plots of the circumferential displacement of the tube showing the measurement and predictions against elevated temperature loads from 50°C to 200°C at 25°C increments and a constant bending load of 400 Newtons for the significant shape descriptors, #1 and #6

Similarly, the error bar plot in figure 64, representing the circumferential displacement as a function of elevated thermal loads and constant bending force of 400 Newtons, shows a reasonable agreement. The significant shape descriptors were #1 and #6. Some discrepancies were observed between the simulation and the measurement at 100°C for the #1 shape descriptor. At this thermal loading point, the simulation data points representing #1 (average magnitude of the data) were outside the region defined by the error bars. This implies that the relative difference between the simulation and the measurement data points was higher than the minimum measurement uncertainty used for this analysis. The difference may result from a shift in the measurement boundary constraints or fluctuation in the model solution during analysis. It is possible that the model must have been more constrained compared to the physical experiment. If the latter were the case, it would have been expected that this behaviour would be noticeable for the other thermal loads. The discrepancy is likely related to the interaction between the thermal and mechanical loads at 100°C. At this temperature, the displacement generated due to the mechanical load is similar to the displacement generated due to the thermal load. However, at higher temperatures, a good agreement was observed. It is also worth noting that the shape descriptor #6, which describes the bending of the tube, was in good agreement, as illustrated in figure 64.

Further analyses were performed to achieve the last objective of this project, which was to mathematically combine the displacement data from the thermal and mechanical physics domain to account for the overall effect in the thermomechanical physics domain, by applying the superposition principle [113], [114], [146]. The superposition principle or property is heavily dependent on linearity. The results obtained from the thermal and mechanical physics domains show a high degree of linearity. Therefore, the average maximum displacement data occurring at the region of interest depicted by the black dotted boxes in figures 65 and 68 were superposed mathematically to account for the thermomechanical effect. The superposed thermal and mechanical circumferential and longitudinal displacement data were compared with the displacement results from the combined thermomechanical experiment, as illustrated in the plots of figures 66, 67, 69, and 70.

The error bar plot in figure 66 represents the superimposed (combined) thermal and mechanical circumferential displacement data and the combined thermomechanical displacement data from the experiment, along with measures of the difference between the different data sets. As observed in the plot, the superimposed thermal and mechanical circumferential displacement fields were similar in magnitude and followed a linear profile. The relative difference between superimposed and the combined thermomechanical displacement fields were approximately zero, indicating a good agreement was achieved between the data points. These results also increase confidence in the thermomechanical experimental design of the test rig to produce reliable deformation data within its design capacity. The error bar used in this analysis is a measure of the combined thermal and mechanical minimum measurement uncertainty determined from the calibration experiment, which is approximately 6% of the maximum displacement result in the plot.

Once a good agreement between the superimposed and the combined circumferential thermomechanical results was achieved, the outcome was employed to validate the corresponding results from the coupled thermomechanical model indicated by the black diamond marker in figure 67. Again, the results showed a high degree of linearity with respect to the thermal and mechanical loads. A good agreement was achieved between the superimposed and coupled physics results, as all of the data points from the model fall within the region represented by the error bars in the plot.

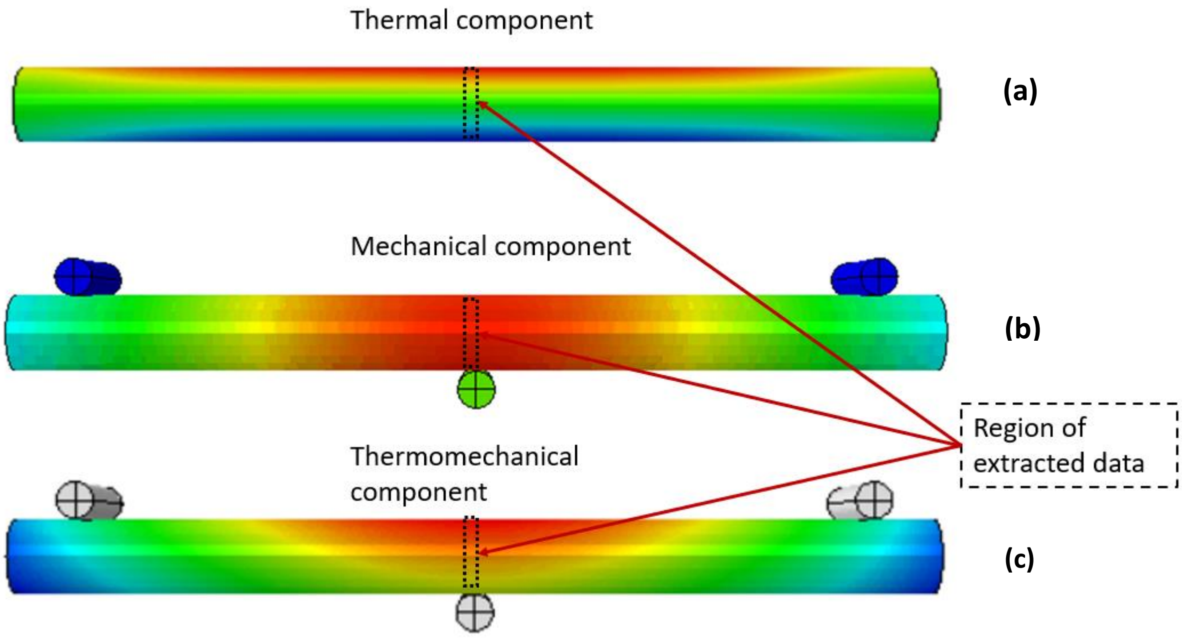

Figure 65: Illustration of the average maximum circumferential displacement extracted from the region of interest depicted by the black dotted boxes for the thermal (top), the mechanical (middle) and the thermomechanical (bottom) measurement physics domains

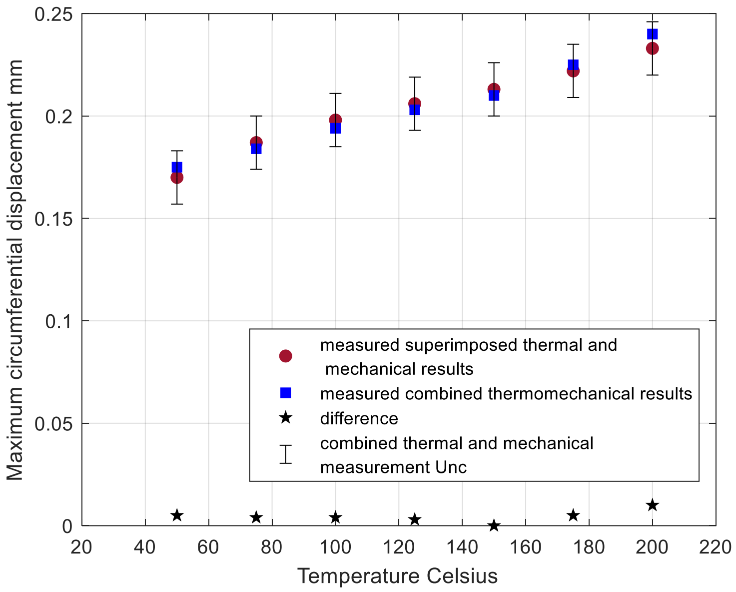

Figure 66: errorbar plot showing the average maximum circumferential displacement of the thermomechanical (blue square maker) and the average maximum superimposed thermal and mechanical displacement (red circle marker), with the associated error bars representing the combined expanded measurement uncertainty from the thermal and mechanical physics domains, at elevated temperatures and a constant bending load of 400 Newtons

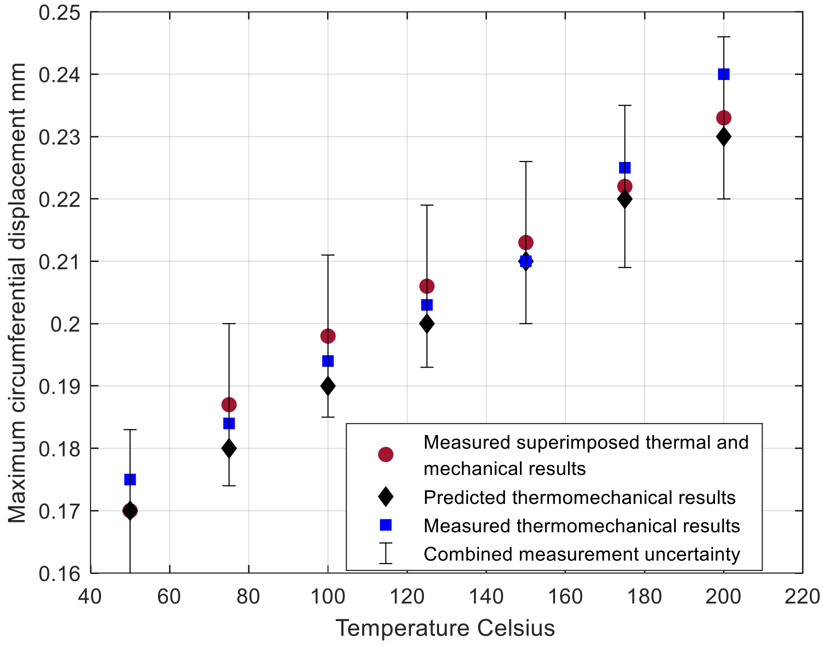

Figure 67: errorbar plot showing the average maximum circumferential displacement of the measured thermomechanical (blue square maker), the average maximum superimposed thermal and mechanical displacement (red circle marker), and the predicted (black diamond marker) thermomechanical,l with the associated error bars representing the combined expanded measurement uncertainty from the thermal and mechanical physics domains, at elevated temperatures and a constant bending load of 400 Newtons

The superposition method was repeated for the longitudinal displacement fields. The region of maximum displacement indicated by the black dotted boxes in figure 68 was averaged. The average value of the maximum displacement data points was used in this analysis. As illustrated in figure 69, a good agreement and correlation was observed between the superimposed displacement data from the thermal and mechanical physics domains and the combined thermomechanical longitudinal displacement from the experiment. The difference between the data sets is depicted by the black star marker in the plot, which is relatively close to zero and negligible. The outcome shows that the combined thermomechanical experiment successfully captured the key physics and boundary conditions from the separate physics domains. It is worth noting that it is not trivial to successfully capture the boundary conditions from separate effect tests or physics domains in a multi-physics experiment.

Once a good agreement was achieved between the superimposed thermomechanical longitudinal displacement fields and the combined thermomechanical displacement fields, the outcome was used to validate the coupled physics model illustrated in figure 70. The results showed a high degree of linearity with respect to increasing thermal loads. The agreement between the superimposed fields and the coupled physics reduces with increasing system load, i.e., the combined thermal and mechanical loads. However, it is worth pointing out here that only the minimum measurement uncertainty from quantified for the thermal physics domain was employed in this analysis, which resulted in a narrow uncertainty bound of approximately 3% of the maximum displacement value in the error bar plot. If other sources of error in figure 8 were quantified as part of the minimum measurement uncertainty, such as the error arising associated with the measured temperature data (±2%), this would increase the error bars and potentially cause the model to fall within the bands of the measurement uncertainty. This approach can be considered for future work.

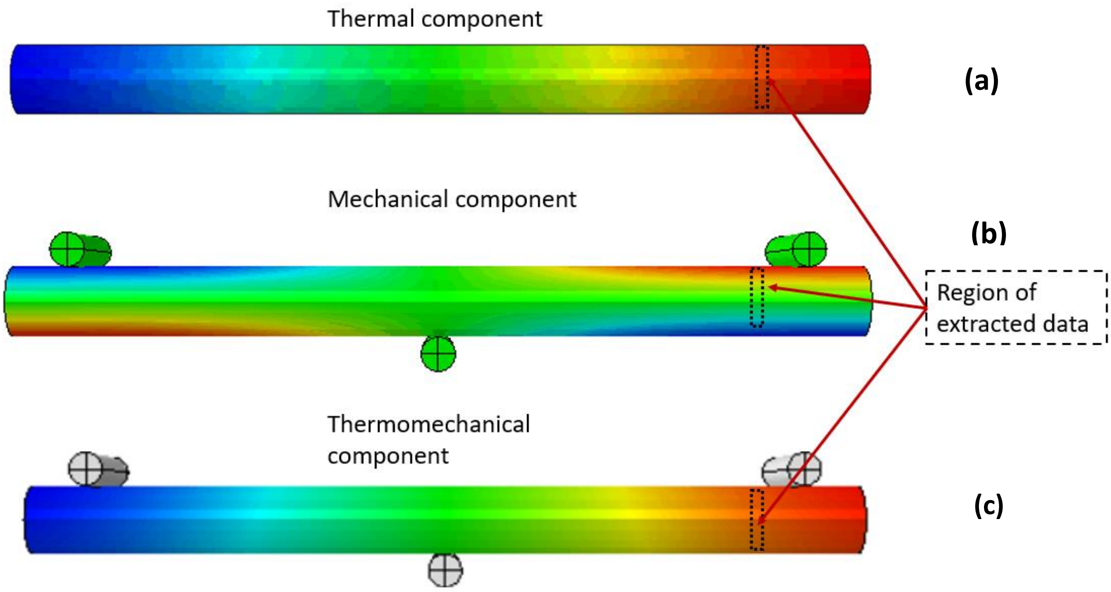

Figure 68: Illustration of the average maximum axial displacement extracted from the region of interest depicted by the black dotted boxes for the thermal (a), the mechanical (b) and the thermomechanical (c) measurement physics domains

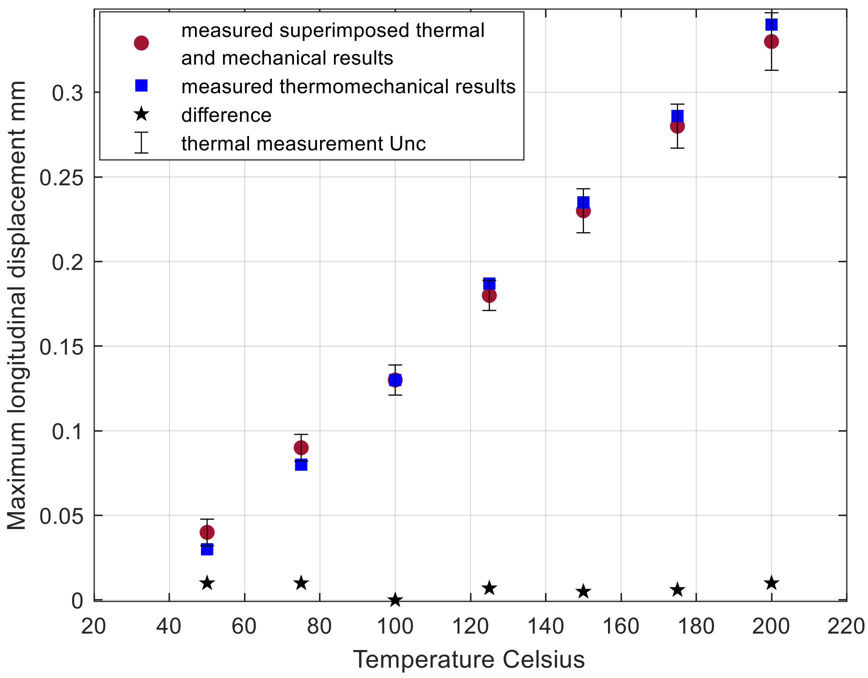

Figure 69: errorbar plot showing the average maximum longitudinal displacement of the measured thermomechanical (blue square maker) and the average maximum superimposed thermal and mechanical transverse displacement (red circle marker), with the associated error bars representing the expanded measurement uncertainty from the thermal physics domains, at elevated temperatures and a constant bending load of 400 newtons

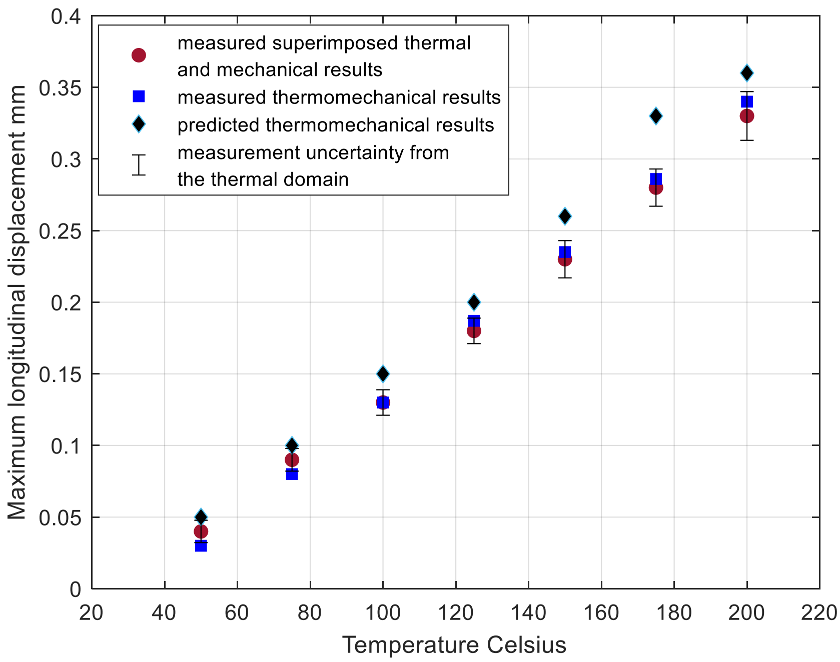

Figure 70: errorbar plot showing the average maximum longitudinal displacement of the measured thermomechanical (blue square maker) and the average maximum superimposed thermal and mechanical transverse displacement (red circle marker), the predicted thermomechanical results (black diamond marker), with the associated error bars representing the expanded measurement uncertainty from the thermal physics domains, at elevated temperatures and a constant bending load of 400 Newtons

7.4. Impact on current state-of-the-art validation guidelines

The validation approach for multi-physics systems demonstrated in this thesis started with the schematic flowchart of the ASME verification and validation guide [5], [6] with input from the CEN guide [12] to account for the full-field validation of deformation data obtained with the optical measurement systems. The challenge addressed by the work reported in this thesis was to expand the processes in the current state-of-the-art validation flowchart to account for multiple physics domains. As previously mentioned in the literature review section, it is difficult and costly to design experiments for full-scale multi-physics systems for the purpose of validation. Therefore, it is reasonable to use separate effect tests from single physics domains to provide an approximation of the corresponding multi-physics systems. The advantages of using separate effect test for the different phenomenon is that (1) it is cost-effective, (2) the test can be carefully designed to capture the physics of interest, which aids in identifying sources of errors in the experiment, and (3) it is easier to generate repeat measurements from single physics domains compared to multi-physics domains. By carefully designed, what is meant is that the experiment should include control factors in order to successfully capture the boundary conditions and constraints from the different occurring physics domains in the multi-physics domain. The challenge involved in using separate effects tests to approximate a full-scale multi-physics system includes integrating or combining the system response and measurement uncertainties from multiple separate effects tests, which has been successfully demonstrated in this project and could impact the current-state-of the-art.

The design approach applied for designing, building, and testing the thermomechanical rig can be applied in the engineering industries to design multi-physics tests for diverse engineering structures within the elastic domain. The key challenge that was overcome in this research was the successful replication of the different physics boundary conditions in the multi-physics experiment and models using the right control instrumentation detailed in chapter 4 of this thesis. For example, the thermal fields were successfully maintained in the thermomechanical test by the use of a thermally resistant material, Tufnol, as the loading pin, which has a low thermal conductivity, and as such, did not alter the temperature distribution of the specimen during bending load. This is an example of one of the control measures applied in the thermo-mechanical test to capture thermal and mechanical physics successfully. The data obtained from the combined thermomechanical physics experiment has been successfully assessed for reliability by comparing the output with analytical solutions. The thermomechanical rig designed and tested as part of this research produces reliable data and can be upscaled to address industrial, multi-physics experimental challenges, particularly within the nuclear industry. The experimental design and system loads can be applied to test an industrial nuclear fuel cladding. Also, the processes of the new extended flowchart can be followed to achieve validation of multi-physics engineering models.

7.5. Conclusions

The results obtained from the thermal, mechanical and combined thermomechanical physics domains show a high degree of linearity with respect to the system loads, which was factored into the experimental designs. The results from the computational models to be validated and the results from the experiments performed for validation were in good agreement and reliable, having measurement uncertainties less than 10% of the maximum displacement values obtained for each physics domain.

The results obtained from the superimposition process generated good agreement with the results from the coupled physics domain, indicating that the physics from the separate physics domains were successfully captured in the coupled physics domain. This outcome also validates the data obtained from the coupled or combined physics experiment, which is a major challenge that this research has successfully addressed.

Chapter 8

8. Conclusions

This thesis addresses the need for a validation approach for multi-physics computational models of engineering systems. An enhanced process in the new flowchart for multi-physics simulations depicted in figure 7 was successfully developed and tested as part of this research. The processes in the enhanced flowchart is an extension of the ASME verification and validation guide [5] and the flowchart from the CEN guide [12].

The processes or road map of the enhanced process flowchart has addressed ways of designing validation experiments for multi-physics systems following a hierarchical approach, which involves splitting the multi-physics system into single physics domains. Splitting the multi-physics system into lower levels of complexity is cost-effective and relatively straightforward to design reliable experiments. It has also allowed an approach to include multiple sources of uncertainties arising from different physics components or domains in a way that is different from the current verification and validation standards.

An industrial component described in chapter 4 has been used as an exemplar to successfully demonstrate the processes of the enhanced flowchart, which include the conception design, build and test of a novel combined thermal and mechanical rig and the corresponding development of the coupled temperature-displacement finite element model. It is believed that this is the first time that such a thermomechanical rig with its configuration (and system embodiments) has been successfully designed and tested. The new rig has enabled, for the first time, both thermal and mechanical bending loads to be applied simultaneously to test cases. The thermomechanical rig has the capacity to record full-field surface strains, displacements, and thermal maps quasi-real-time data at high temperatures. The rig is also connected to a Labview environment that enables real-time monitoring of the system loads. This is a significant advance in experimental methodology and an approach for designing multi-physics experiments.

The intended physics, boundary conditions and constraints from the thermal, mechanical, and combined thermomechanical experiments were successfully captured in the finite element models, as this is an essential factor when designing validation experiments. Good agreement was observed between the predictions and the measured displacement results for the different physics components, considering the narrow uncertainty bands associated with the measurement results. The results also show a high degree of linearity with respect to the system loads in the single physics and coupled physics domains, which was desirable when designing multi-physics experiments following a hierarchical approach.

As seen from the results of the calibration experiments, the systematic uncertainty increases with increasing system loads or increasing thermal loads. Therefore, for this research, the displacement results at increasing system loads (thermal loads) are presented with the associated error bars, which indicate the minimum measurement uncertainty for each system load, which were determined from the calibration experiment detailed in chapter five of this thesis. The presentation of the uncertainty associated with the measurements in this thesis is different from the process described in the CEN guide or European standard. In this work, only the minimum measurement uncertainty associated with the instrumentation (described in the CEN guide) has been used to assess the quality of the recorded data from each physics domain as the first step toward multi-physics validation. In other words, this work is an extension of the way measurement uncertainty is presented, particularly for multi-physics experiments.

This is also the first time the image decomposition technique has been successfully applied to decompose full-field response data of a test specimen subjected to multiple, simultaneous system loads (thermal and mechanical bending loads). Previously, image decomposition has been used to decompose response data obtained from a test specimen subjected to a single system load. The successful application of this technique to decompose data from multiple simultaneous system loads is an advancement of this tool in industrial applications.

The novel combined thermomechanical rig is equipped with controlled instrumentations that make it scalable for industrial applications. The rig's performance has been validated in the study of a laboratory specimen, the results of which compare well with simulated data and analytical solutions with errors within the total measurement uncertainty.

In conclusion, the aim and objectives of this project, which was to develop an approach for the validation of multi-physics system models using quantitative experimental data obtained from a carefully designed and tested validation experiment, were successfully achieved in this thesis. The processes of the extended flowchart were successfully demonstrated and produced reliable results.

8.1. Further work

This research serves as a first approach for the validation of multi-physics models using full-field measurement data from a designed validation experiment. The research method and experiment, in this case, can be optimised or extended to include the following:

- More physics domains, such as the effect of radiation which is vital for nuclear engineering components,
- Additional sources of uncertainty can be included in the validation assessment as depicted in the uncertainty flowchart in figure 8,
- This work can be optimised to account for non-linear behaviours.

References

[1] E. A. Patterson, R. J. Taylor, and M. Bankhead, “A framework for an integrated nuclear digital environment,” *Prog. Nucl. Energy*, vol. 87, pp. 97–103, 2016, doi: 10.1016/j.pnucene.2015.11.009.

[2] E. Patterson, “On the credibility of engineering models and meta-models,” *Journal of Strain Analysis for Engineering Design*, vol. 50, no. 4, pp. 218–220, 2015.

[3] L. W. Schruben, “Establishing the credibility of simulations,” *Simulation*, vol. 34, no. 3, pp. 101–105, 1980, doi: 10.1177/003754978003400310.

[4] AIAA, “Guide: Guide for the Verification and Validation of Computational Fluid Dynamics Simulations (AIAA G-077-1998(2002)),” in *Guide: Guide for the Verification and Validation of Computational Fluid Dynamics Simulations (AIAA G-077-1998(2002))*, American Institute of Aeronautics and Astronautics, Inc., 1998.

[5] ASME, “Guide for Verification and Validation in Computational Solid Mechanics,” *Am. Soc. Mech. Eng.*, 2006, doi: 10.1007/s00366-007-0072-z.

[6] ASME V&V 10.1-2012, “An Illustration of the Concepts of Verification and Validation in Computational Solid Mechanics,” 2012.

[7] P. J. K. GEORGE S. FISHMAN, “The statistics of discrete-event simulation by,” *Simulations*, vol. 10, pp. 185–195, 1967.

[8] R. L. Van Horn, “Validation of Simulation Results,” *Manage. Sci.*, vol. 17, no. 5, pp. 247–258, 1971.

[9] R. G. Sargent, “OVERVIEW OF VERIFICATION AND VALIDATION OF SIMULATION MODELS.,” 1987.

[10] C. Sebastian, E. Hack, and E. Patterson, “An approach to the validation of computational solid mechanics models for strain analysis,” *J. Strain Anal. Eng. Des.*, vol. 48, no. 1, pp. 36–47, 2012, doi: 10.1177/0309324712453409.

[11] VANESSA, “Inter-laboratory Study Protocol for the Validation of Computational Solid Mechanics Models Using Full-Field Optical Data,” 2013. http://www.engineeringvalidation.org/?VANESSA_home.

[12] CWA 16799:2014, “Validation of computational solid mechanics models,” *Com. Eur. Norm.*, no. CWA16799(2014), 2014.

[13] B. Collins *et al.*, “Stability and accuracy of 3D neutron transport simulations using the 2D/1D method in MPACT,” *J. Comput. Phys.*, vol. 326, pp. 612–628, 2016, doi: 10.1016/j.jcp.2016.08.022.

[14] R. Y. Lu, Z. Karoutas, and T. L. Sham, “CASL virtual reactor predictive simulation: Grid-to-Rod Fretting wear,” *JOM*, vol. 63, no. 8, pp. 53–58, 2011, doi: 10.1007/s11837-011-0139-6.

[15] V. S. Mahadevan *et al.*, “High-resolution coupled physics solvers for analysing fine-scale nuclear reactor design problems,” *Philos. Trans. R. Soc. A Math. Phys. Eng. Sci.*, vol. 372, no. 2021, 2014, doi: 10.1098/rsta.2013.0381.

[16] M. N. Dupont, M. D. Eklund, P. F. Caracappa, and W. Ji, “Development of critical experiments to provide validation data for multiphysics coupling codes,” *Ann. Nucl. Energy*, vol. 128, pp. 256–267, 2019, doi: 10.1016/j.anucene.2018.12.043.

[17] G. Massimino *et al.*, “Multiphysics modelling and experimental validation of an air-coupled array of PMUTs with residual stresses,” *J. Micromechanics Microengineering*, vol. 28, no. 5, 2018, doi: 10.1088/1361-6439/aaaf78.

[18] O. Balci, “Principles and techniques of simulation validation, verification, and testing,” *Simul. Conf. Proceedings, 1995. Winter*, pp. 147–152, 1995, doi: 10.1109/WSC.1995.478717.

[19] J. G. Marvin, “Perspective on computational fluid dynamics validation,” *AIAA J.*, vol. 33, no. 10, pp. 1778–1787, Oct. 1995, doi: 10.2514/3.12727.

[20] P. J. Roache, “Verification and Validation in Computational Science and Engineering,” in *Computing in Science Engineering*, 1998, pp. 8–9.

[21] W. L. Oberkampf and T. G. Trucano, *Verification and validation in computational fluid dynamics*, vol. 38, no. 3. 2002.

[22] W. L. Oberkampf, T. G. Trucano, and C. Hirsch, “Verification, validation, and predictive capability in computational engineering and physics,” *Appl. Mech. Rev.*, vol. 57, no. 5, p. 345, 2004, doi: 10.1115/1.1767847.

[23] C. J. Roy and W. L. Oberkampf, “A comprehensive framework for verification, validation, and uncertainty quantification in scientific computing,” *Comput. Methods Appl. Mech. Eng.*, vol. 200, no. 25–28, pp. 2131–2144, 2011, doi: 10.1016/j.cma.2011.03.016.

[24] O. Balci, “How to assess the acceptability and credibility of simulation results,” 1989, doi: 10.1145/76738.76746.

[25] E. A. Patterson and M. P. Whelan, “A framework to establish credibility of computational models in biology,” *Prog. Biophys. Mol. Biol.*, vol. 129, pp. 13–19, 2017, doi: 10.1016/j.pbiomolbio.2016.08.007.

[26] E. A. Patterson and M. P. Whelan, “On the validation of variable fidelity multi-physics simulations,” *J. Sound Vib.*, vol. 448, pp. 247–258, 2019, doi: 10.1016/j.jsv.2019.01.051.

[27] R. G. George B. Kleindorfer, Liam O’Neill, “Validation in Simulation: Various Positions in the Philosophy of Science,” *Manage. Sci.*, vol. 44, no. 8, pp. 1087–1099, 1998.

[28] R. Audi, *Epistemology: A contemporary introduction to the theory of knowledge*, Third ed. New York: Routledge, 2010.

[29] O. C. Zienkiewicz and R. L. Taylor, *The Finite Element Method Volume 1 : The Basis*, Fifith edi., vol. 1. Oxford: Butterworth-Heinemann, 2000.

[30] L. Gaul, M. Kögl, and M. Wagner, *Boundary Element Methods for Engineers and Scientists*, 1st ed. Berlin, Heidelberg: Springer, Berlin, Heidelberg, 2003.

[31] ONR, “Validation of Computer Codes and Calculation Methods,” 2016.

[32] W. L. Oberkampf and T. G. Trucano, “Verification and validation benchmarks,” *Nucl. Eng. Des.*, vol. 238, no. 3, pp. 716–743, 2008, doi: 10.1016/j.nucengdes.2007.02.032.

[33] S. L. Lin, S. J., Chan, D. C., Sindir, M. M., and Barson, “Development of CFD code evaluation criteria and a procedure for assessing predictive capability and performance,” in *10th Workshop for Computational Fluid Dynamic Applications in Rocket Propulsion*, 1992, pp. 109–121.

[34] R. R. Cosner, “CFD validation requirements for technology transitions,” in *Fluid Dynamics Conference*, 1995, pp. 95–2227, [Online]. Available: https://doi.org/10.2514/6.1995-2227.

[35] W. L. Oberkampf and T. G. Trucano, “Verification and validation in computational fluid dynamics,” *Prog. Aerosp. Sci.*, vol. 38, no. 3, pp. 209–272, 2002, doi: 10.1016/S0376-0421(02)00005-2.

[36] B. H. Thacker, S. W. Doebling, F. M. Hemez, M. C. Anderson, J. E. Pepin, and E. A. Rodriguez, “Concepts of Model Verification and Validation.” 2004, Accessed: Dec. 17, 2019. [Online]. Available: https://inis.iaea.org/search/search.aspx?orig_q=RN:36030870.

[37] D. M, *Philosophy and simulation: the emergence of synthetic reason*. London: Continuum International Pub- lishing Group, 2011.

[38] Christopher W. Johnson, “What are Emergent Properties and How Do They Affect the Engineering of Complex Systems?,” *Reliab. Eng. Syst. Saf.*, vol. 12, p. :1475–1481, 2006.

[39] C. Szabo and Y. M. Teo, “AN INTEGRATED APPROACH FOR THE VALIDATION OF EMERGENCE IN COMPONENT-BASED SIMULATION MODELS,” in *Proceedings of the 2012 Winter Simulation Conference 6(11), 951–952.*, 2012, pp. 2013–2015.

[40] J. S. Osmundson, T. V. Huynh, and G. O. Langford, “Emergent behavior in systems of systems,” in *18th Annual International Symposium of the International Council on Systems Engineering, INCOSE 2008*, 2008, vol. 4, pp. 2021–2031.

[41] A. Turbull, “Review of Nuclear Fuel Experimental Data,” 1995.

[42] E. A. Patterson *et al.*, “Validation of a structural model of an aircraft cockpit panel: An industrial case study,” *J. Strain Anal. Eng. Des.*, 2021, doi: 10.1177/03093247211059084.

[43] W. L. Oberkampf, “What Are Validation Experiments?,” *Exp. Tech.*, vol. 25, no. 3, pp. 35–40, 2001, doi: 10.1111/j.1747-1567.2001.tb00023.x.

[44] C. J. Oberkampf, W. L. and Roy, “Verification and Validation in Scientific Computing,” Cambridge: Cambridge University Press, 2010, pp. 409–468.

[45] B. Pan, K. Qian, H. Xie, and A. Asundi, “Two-dimensional digital image correlation for in-plane displacement and strain measurement: a review,” *Meas. Sci. Technol.*, vol. 20, no. 6, p. 062001, Jun. 2009, doi: 10.1088/0957-0233/20/6/062001.

[46] M. Sutton, W. Wolters, W. Peters, W. Ranson, and S. McNeill, “Determination of displacements using an improved digital correlation method,” *Image Vis. Comput.*, vol. 1, no. 3, pp. 133–139, 1983, doi: 10.1016/0262-8856(83)90064-1.

[47] M. Sutton, C. Mingqi, W. Peters, Y. Chao, and S. McNeill, “Application of an optimized digital correlation method to planar deformation analysis,” *Image Vis. Comput.*, vol. 4, no. 3, pp. 143–150, 1986, doi: 10.1016/0262-8856(86)90057-0.

[48] H. Schreier, J. J. Orteu, and M. A. Sutton, *Image correlation for shape, motion and deformation measurements: Basic concepts, theory and applications*. 2009.

[49] B. Pan and K. Li, “A fast digital image correlation method for deformation measurement,” *Opt. Lasers Eng.*, vol. 49, no. 7, pp. 841–847, Jul. 2011, doi: 10.1016/J.OPTLASENG.2011.02.023.

[50] J. D. Carroll, W. Abuzaid, J. Lambros, and H. Sehitoglu, “High resolution digital image correlation measurements of strain accumulation in fatigue crack growth,” *Int. J. Fatigue*, vol. 57, pp. 140–150, 2013, doi: 10.1016/j.ijfatigue.2012.06.010.

[51] S. H. Tung and C. H. Sui, “Application of digital-image-correlation techniques in analysing cracked cylindrical pipes,” *Sadhana - Acad. Proc. Eng. Sci.*, vol. 35, no. 5, pp. 557–567, 2010,

doi: 10.1007/s12046-010-0039-4.

[52] B. Pan, D. Wu, Z. Wang, and Y. Xia, “High-temperature digital image correlation method for full-field deformation measurement at 1200 °C,” *Meas. Sci. Technol.*, vol. 22, no. 1, 2011, doi: 10.1088/0957-0233/22/1/015701.

[53] R. B. Berke, C. M. Sebastian, R. Chona, E. A. Patterson, and J. Lambros, “High Temperature Vibratory Response of Hastelloy-X: Stereo-DIC Measurements and Image Decomposition Analysis,” *Exp. Mech.*, vol. 56, no. 2, pp. 231–243, 2016, doi: 10.1007/s11340-015-0092-3.

[54] A. C. Santos Silva, C. M. Sebastian, J. Lambros, and E. A. Patterson, “High temperature modal analysis of a non-uniformly heated rectangular plate: Experiments and simulations,” *J. Sound Vib.*, vol. 443, pp. 397–410, 2019, doi: 10.1016/j.jsv.2018.11.041.

[55] W. Wang, J. E. Mottershead, A. Patki, and E. A. Patterson, “Construction of shape features for the representation of full-field displacement/strain data,” *Appl. Mech. Mater.*, vol. 24–25, pp. 365–370, 2010, doi: 10.4028/www.scientific.net/AMM.24-25.365.

[56] W. Wang, J. E. Mottershead, C. M. Sebastian, and E. A. Patterson, “Shape features and finite element model updating from full-field strain data,” *Int. J. Solids Struct.*, vol. 48, no. 11–12, pp. 1644–1657, 2011, doi: 10.1016/j.ijsolstr.2011.02.010.

[57] A. S. Patki and E. A. Patterson, “Decomposing Strain Maps Using Fourier-Zernike Shape Descriptors,” *Exp. Mech.*, vol. 52, no. 8, pp. 1137–1149, 2012, doi: 10.1007/s11340-011-9570-4.

[58] R. L. Burguete *et al.*, “Analysis of displacement fields from a high-speed impact using shape descriptors,” *J. Strain Anal. Eng. Des.*, vol. 49, no. 4, pp. 212–223, 2014, doi: 10.1177/0309324713498074.

[59] C. Sebastian, E. Hack, and E. Patterson, “An approach to the validation of computational solid mechanics models for strain analysis,” *J. Strain Anal. Eng. Des.*, vol. 48, no. 1, pp. 36–47, 2013, doi: 10.1177/0309324712453409.

[60] W. L. Oberkampf, S. M. DeLand, B. M. Rutherford, K. V. Diegert, and K. F. Alvin, “Error and uncertainty in modeling and simulation,” *Reliab. Eng. Syst. Saf.*, vol. 75, no. 3, pp. 333–357, 2002, doi: 10.1016/S0951-8320(01)00120-X.

[61] E. . Hack, G. . Lampeas, and E. A. . Patterson, “An evaluation of a protocol for the validation of computational solid mechanics models,” *J. Strain Anal. Eng. Des.*, vol. 51, no. 1, pp. 5–13, 2016, doi: 10.1177/0309324715616017.

[62] S. R. C., *Uncertainty quantification: theory, implementation, and applications*. 2013.

[63] V. G. Weirs *et al.*, “Nuclear Energy – Knowledge Base for Advanced Modeling and Simulation (NE-KAMS) code verification and validation data standards and requirements : fluid dynamics,” no. September, 2011.

[64] B. H. Thacker, S. W. Doebling, F. M. Hemez, M. C. Anderson, J. E. Pepin, and E. a. Rodriguez, “Concepts of Model Verification and Validation,” *LA -14167*, vol. 36, no. 12, p. 41, 2004, doi: 10.2172/835920.

[65] R. Zhang and S. Mahadevan, “Bayesian methodology for reliability model acceptance,” *Reliab. Eng. Syst. Saf.*, vol. 80, no. 1, pp. 95–103, 2003, doi: 10.1016/S0951-8320(02)00269-7.

[66] M. C. Kennedy and A. O’Hagan, “Bayesian Calibration of Computer Models,” *J. R. Stat. Soc. Ser. B (Statistical Methodol.*, vol. 63, no. 3, pp. 425–464, 2001, doi: 10.1111/1467-9868.00294.

[67] C. Wang, H. Zhang, and M. Beer, "Computing tight bounds of structural reliability under imprecise probabilistic information," *Comput. Struct.*, vol. 208, pp. 92–104, 2018, doi: 10.1016/j.compstruc.2018.07.003.

[68] A. Saltelli, "Sensitivity analysis for importance assessment," *Risk Anal.*, vol. 22, no. 3, pp. 579–590, 2002, doi: 10.1111/0272-4332.00040.

[69] A. Saltelli, S. Tarantola, F. Campolongo, and M. Ratto, "Global Sensitivity Analysis for Importance Assessment," *Sensit. Anal. Pract.*, no. I, pp. 31–61, 2004, doi: 10.1002/0470870958.ch2.

[70] R. Bolado-Lavin and A. Badea, "Review of Sensitivity Analysis Methods and Experience for Geological Disposal of Radioactive waste and Spent Nuclear Fuel," *JRC Sci. Tech. Reports*, pp. 191–265, 2008.

[71] K. M. Hanson, "A framework for assessing uncertainties in simulation predictions," *Phys. D Nonlinear Phenom.*, vol. 133, no. 1, pp. 179–188, 1999, doi: 10.1016/S0167-2789(99)00090-1.

[72] W. Chen, L. Baghdasaryan, T. Buranathiti, and J. Cao, "Model Validation via Uncertainty Propagation and Data Transformations," *AIAA J.*, vol. 42, no. 7, pp. 1406–1415, Jul. 2008, doi: 10.2514/1.491.

[73] R. Flage, T. Aven, and C. L. Berner, "A comparison between a probability bounds analysis and a subjective probability approach to express epistemic uncertainties in a risk assessment context – a simple illustrative example," *Reliab. Eng. Syst. Saf.*, vol. 169, no. December 2016, pp. 1–10, 2017, doi: 10.1016/j.ress.2017.07.016.

[74] A. Urbina and S. Mahadevan, "Uncertainty quantification in hierarchical development of computational models," 2009, doi: 10.2514/6.2009-2282.

[75] M. N. Avramova and K. N. Ivanov, "Verification, validation and uncertainty quantification in multi-physics modeling for nuclear reactor design and safety analysis," *Prog. Nucl. Energy*, vol. 52, no. 7, pp. 601–614, 2010, doi: 10.1016/j.pnucene.2010.03.009.

[76] K. Ivanov and M. Avramova, "Challenges in coupled thermal-hydraulics and neutronics simulations for LWR safety analysis," *Ann. Nucl. Energy*, vol. 34, no. 6, pp. 501–513, 2007, doi: 10.1016/j.anucene.2007.02.016.

[77] X. Chen, B. Ng, Y. Sun, and C. Tong, "A flexible uncertainty quantification method for linearly coupled multi-physics systems," *J. Comput. Phys.*, vol. 248, pp. 383–401, 2013, doi: 10.1016/j.jcp.2013.04.009.

[78] B. R. G. Ghanem, A. Member, and P. D. Spanos, "SPECTRAL STOCHASTIC FINITE-ELEMENT FORMULATION FOR RELIABILITY ANALYSIS," *J. Eng. Mech.*, vol. 117, no. 10, pp. 2351–2372, 1991, [Online]. Available: https://doi.org/10.1061/(ASCE)0733-9399(1991)117:10(2351).

[79] O. P. L. M. O.M. Knio, "Uncertainty propagation in CFD using polynomial chaos decomposition," *Fluid Dyn. Res.*, vol. 38, no. 9, pp. 616–640, 2006, doi: https://doi.org/10.1016/j.fluiddyn.2005.12.003.

[80] and T. M. W. P. G. Constantine, E. T. Phipps, "Efficient uncertainty propagation for network multiphysics systems," *Int. J. Numer. Meth. Engng*, vol. 99, pp. 183–202, 2014, doi: 10.1002/nme.4667.

[81] K. Zeng, J. Hou, K. Ivanov, and M. A. Jessee, "Uncertainty Quantification and Propagation of Multiphysics Simulation of the Pressurized Water Reactor Core," *Nucl. Technol.*, vol. 205, no. 12, pp. 1618–1637, 2019, doi: 10.1080/00295450.2019.1580533.

[82] M. Avramova, A. Abarca, J. Hou, and K. Ivanov, “Innovations in Multi-Physics Methods Development, Validation, and Uncertainty Quantification,” *J. Nucl. Eng.*, vol. 2, no. 1, pp. 44–56, 2021, doi: 10.3390/jne2010005.

[83] A. Saltelli, S. Tarantola, F. Campolongo, and M. Ratto, *Sensitivity analysis in practice: a guide to assessing scientific models*. Chischester: John Willey & Sons, 2004.

[84] J. C. Helton, J. D. Johnson, C. J. Sallaberry, and C. B. Storlie, “Survey of sampling-based methods for uncertainty and sensitivity analysis,” *Reliab. Eng. Syst. Saf.*, vol. 91, no. 10–11, pp. 1175–1209, 2006, doi: 10.1016/j.ress.2005.11.017.

[85] J. C. Lam and S. C. M. Hui, “Sensitivity analysis of energy performance of office buildings,” *Build. Environ.*, vol. 31, no. 1, pp. 27–39, 1996, doi: 10.1016/0360-1323(95)00031-3.

[86] M. D. Morris, “Factorial sampling plans for preliminary computational experiments,” *Technometrics*, vol. 33, no. 2, pp. 161–174, 1991, doi: 10.1080/00401706.1991.10484804.

[87] C. M. A.-C. D. C. M. R. H. Myers, *Response Surface Methodology: Process and Product Optimization Using Designed Experiments*, 4th Editio. John Wiley and Sons, 2016.

[88] F. Campolongo, A. Saltelli, and S. Tarantola, “Sensitivity Anaysis as an Ingredient of Modeling,” *Stat. Sci.*, vol. 15, no. 4, pp. 377–395, 2000.

[89] V. G. Weirs *et al.*, “Sensitivity analysis techniques applied to a system of hyperbolic conservation laws,” *Reliab. Eng. Syst. Saf.*, vol. 107, pp. 157–170, 2012, doi: 10.1016/j.ress.2011.12.008.

[90] ISO, “Evaluation of measurement data — Guide to the expression of uncertainty in measurement,” 2008. [Online]. Available: http://www.bipm.org/en/publications/guides/gum.html.

[91] B. N. Taylor and C. E. Kuyatt, “Guidelines for Evaluating and Expressing the Uncertainty of NIST Measurement Results,” Gaithersburg, MD 20899-0001, 1994. [Online]. Available: https://www.nist.gov/pml/nist-technical-note-1297.

[92] H. Haddadi and S. Belhabib, “Use of rigid-body motion for the investigation and estimation of the measurement errors related to digital image correlation technique,” *Opt. Lasers Eng.*, 2008, doi: 10.1016/j.optlaseng.2007.05.008.

[93] G. F. Bomarito, J. D. Hochhalter, T. J. Ruggles, and A. H. Cannon, “Increasing accuracy and precision of digital image correlation through pattern optimization,” *Opt. Lasers Eng.*, vol. 91, no. October 2016, pp. 73–85, 2017, doi: 10.1016/j.optlaseng.2016.11.005.

[94] M. Bornert *et al.*, “Shortcut in DIC error assessment induced by image interpolation used for subpixel shifting,” *Opt. Lasers Eng.*, vol. 91, pp. 124–133, 2017, doi: 10.1016/j.optlaseng.2016.11.014.

[95] M. A. Sutton, J. H. Yan, V. Tiwari, H. W. Schreier, and J. J. Orteu, “The effect of out-of-plane motion on 2D and 3D digital image correlation measurements,” *Opt. Lasers Eng.*, vol. 46, no. 10, pp. 746–757, 2008, doi: 10.1016/j.optlaseng.2008.05.005.

[96] T. Siebert, “High-speed digital image correlation: error estimations and applications,” *Opt. Eng.*, vol. 46, no. 5, p. 051004, 2007, doi: 10.1117/1.2741217.

[97] E. A. Patterson *et al.*, “Calibration and evaluation of optical systems for full-field strain measurement,” *Opt. Lasers Eng.*, vol. 45, no. 5, pp. 550–564, 2007, doi: 10.1016/j.optlaseng.2006.08.012.

[98] Joint Committee for Guides in Metrology (JCGM/WG 2), "International Vocabulary of Metrology – Basic and General Concepts and Associated Terms (VIM)," 2006.

[99] T. Siebert, E. Hack, G. Lampeas, E. A. Patterson, and K. Splitthof, "Uncertainty Quantification for DIC Displacement Measurements in Industrial Environments," *Exp. Tech.*, vol. 45, no. 5, pp. 685–694, 2021, doi: 10.1007/s40799-021-00447-3.

[100] E. A. Patterson *et al.*, "Calibration and evaluation of optical systems for full-field strain measurement," *Opt. Lasers Eng.*, vol. 45, no. 5, pp. 550–564, May 2007, doi: 10.1016/J.OPTLASENG.2006.08.012.

[101] E. Hack, X. Lin, E. A. Patterson, and C. M. Sebastian, "A reference material for establishing uncertainties in full-field displacement measurements," *Meas. Sci. Technol.*, vol. 26, no. 7, 2015, doi: 10.1088/0957-0233/26/7/075004.

[102] W. L. Oberkampf and M. F. Barone, "Measures of agreement between computation and experiment: Validation metrics," *J. Comput. Phys.*, vol. 217, no. 1, pp. 5–36, 2006, doi: 10.1016/j.jcp.2006.03.037.

[103] Y. Liu, W. Chen, P. Arendt, and H. Z. Huang, "Toward a better understanding of model validation metrics," *J. Mech. Des.*, vol. 133, no. 7, pp. 1–13, 2011, doi: 10.1115/1.4004223.

[104] K. A. Maupin, L. P. Swiler, and N. W. Porter, "Validation Metrics for Deterministic and Probabilistic Data," *J. Verif. Valid. Uncertain. Quantif.*, vol. 3, no. 3, Jan. 2019, doi: 10.1115/1.4042443.

[105] D. C. Montgomery and G. C. Runger, *Applied Statistics and Probability for Engineers*. 2011.

[106] X. Jiang, R. Yang, S. Barbat, and P. Weerappuli, "Bayesian Probabilistic PCA Approach for Model Validation of Dynamic Systems," *SAE Int. Mater. Manuf.*, vol. 2, no. 1, pp. 555–563, 2017.

[107] S. Nakajima, M. Sugiyama, and D. Babacan, "On Bayesian PCA: Automatic Dimensionality Selection and Analytic Solution," in *Proceedings of the 28th International Conference on Machine Learning (ICML-11)*, 2011, pp. 497–504.

[108] C.-J. Kat and P. S. Els, "Validation metric based on relative error," *Math. Comput. Model. Dyn. Syst.*, vol. 18, no. 5, pp. 487–520, 2012, doi: 10.1080/13873954.2012.663392.

[109] F. Liu, M. J. Bayarri, J. O. Berger, R. Paulo, and J. Sacks, "A Bayesian analysis of the thermal challenge problem," *Comput. Methods Appl. Mech. Eng.*, vol. 197, no. 29–32, pp. 2457–2466, 2008, doi: 10.1016/j.cma.2007.05.032.

[110] D. Higdon, C. Nakhleh, J. Gattiker, and B. Williams, "A Bayesian calibration approach to the thermal problem," *Comput. Methods Appl. Mech. Eng.*, vol. 197, no. 29–32, pp. 2431–2441, 2008, doi: 10.1016/j.cma.2007.05.031.

[111] K. Dvurecenska, S. Graham, E. Patelli, and E. A. Patterson, "A probabilistic metric for the validation of computational models," *R. Soc. Open Sci.*, vol. 5, no. 11, 2018, doi: 10.1098/rsos.180687.

[112] H. L. F. Von Helmholtz, "Some laws concerning the distribution of electric currents in volume conductors with applications to experiments on animal electricity," *Proc. IEEE*, vol. 92, no. 5, pp. 868–870, 2004, doi: 10.1109/JPROC.2004.826598.

[113] R. C. Bishop, *Metaphysical and Epistemological Issues in Complex Systems*, vol. 10. Elsevier B.V., 2011.

[114] B. Aamodt and P. G. Bergan, “On the principle of superposition for stress intensity factors,” *Eng. Fract. Mech.*, vol. 8, no. 2, pp. 437–440, 1976, doi: 10.1016/0013-7944(76)90023-0.

[115] J. Jäger, “A New Principle in Contact Mechanics,” *J. Tribol.*, vol. 120, no. 4, pp. 677–684, 1998, doi: 10.1115/1.2833765.

[116] J. K. Kim and S. B. Cho, “A superposition approach to the stress fields for various blunt V-notches,” *Fatigue Fract. Eng. Mater. Struct.*, vol. 36, no. 2, pp. 139–153, 2013, doi: 10.1111/j.1460-2695.2012.01706.x.

[117] C. Jiang, H. Jiang, Z. Zhu, J. Zhang, S. Guo, and Y. Xiong, “Application of time-temperature-stress superposition principle on the accelerated physical aging test of polycarbonate,” *Polymer Engineering and Science*, vol. 55, no. 10. pp. 2215–2221, 2015, doi: 10.1002/pen.24106.

[118] L. M. Aŕevalo Aguilar, C. Robledo-Śanchez, M. L. Arroyo Carrasco, and M. M. Ḿendez Otero, “The principle of superposition for waves: The amplitude and phase modulation phenomena,” *Appl. Math. Inf. Sci.*, vol. 6, no. 2, pp. 307–315, 2012.

[119] G. Rengaraj, U. Prathwiraj, and U. Sinha, “On measuring the deviation from the superposition principle in interference experiments,” *AIP Conf. Proc.*, vol. 2109, 2019, doi: 10.1063/1.5110125.

[120] E. O. Oshogbunu, Y. C. Wang, and T. Stallard, “A new method for calculating hot-spot stress in gap DKK CHS joints under arbitrary loading,” *Eng. Struct.*, vol. 210, no. February, p. 110366, 2020, doi: 10.1016/j.engstruct.2020.110366.

[121] E. O. Oshogbunu, Y. C. Wang, and T. Stallard, “Reliability and applications of a new design method for calculating hot-spot stress in CHS double K-joints under arbitrary combined loading,” *Structures*, vol. 29, no. November 2020, pp. 1610–1626, 2021, doi: 10.1016/j.istruc.2020.11.057.

[122] J. H. Kim, M. H. Lee, B. K. Choi, and Y. H. Jeong, “Deformation behavior of Zircaloy-4 cladding under cyclic pressurization,” *J. Nucl. Sci. Technol.*, vol. 44, no. 10, 2007, doi: 10.3327/jnst.44.1275.

[123] G. Pastore, L. Luzzi, V. Di Marcello, and P. Van Uffelen, “Physics-based modelling of fission gas swelling and release in UO 2 applied to integral fuel rod analysis,” *Nucl. Eng. Des.*, vol. 256, pp. 75–86, 2013, doi: 10.1016/j.nucengdes.2012.12.002.

[124] D. Post and J. D. Wood, “Determination of thermal strains by moiré interferometry,” *Exp. Mech.*, vol. 29, no. 3, pp. 318–322, 1989, doi: 10.1007/BF02321415.

[125] M. Anwander, B. G. Zagar, B. Weiss, and H. Weiss, “Noncontacting strain measurements at high temperatures by the digital laser speckle technique,” *Exp. Mech.*, vol. 40, no. 1, pp. 98–105, 2000, doi: 10.1007/BF02327556.

[126] M. A. Sutton, “Digital Image Correlation for Shape and Deformation Measurements - Springer Handbook of Experimental Solid Mechanics,” W. N. Sharpe, Ed. Boston, MA: Springer US, 2008, pp. 565–600.

[127] Y. Q. Wang, M. A. Sutton, H. A. Bruck, and H. W. Schreier, “Quantitative Error Assessment in Pattern Matching: Effects of Intensity Pattern Noise, Interpolation, Strain and Image Contrast on Motion Measurements,” *Strain*, vol. 45, no. 2, pp. 160–178, Apr. 2009, doi: 10.1111/j.1475-1305.2008.00592.x.

[128] K. R. Siebert T, Becker T, Spiltthof K, Neumann I, “Error Estimations in Digital Image

Correlation Technique,” *Appl. Mech. Mater.*, vol. 7–8, pp. 265–270, 2007, [Online]. Available: https://doi.org/10.4028/www.scientific.net/amm.7-8.265.

[129] P. Reu, “Speckles and their relationship to the digital camera,” *Exp. Tech.*, vol. 38, no. 4, pp. 1–2, 2014, doi: 10.1111/ext.12105.

[130] P. Reu, “All about speckles: Aliasing,” *Exp. Tech.*, vol. 38, no. 5, pp. 1–3, 2014, doi: 10.1111/ext.12111.

[131] P. Reu, “All about speckles: Speckle size measurement,” *Exp. Tech.*, vol. 38, no. 6, pp. 1–2, 2014, doi: 10.1111/ext.12110.

[132] P. Reu, “All about speckles: Contrast,” *Exp. Tech.*, vol. 39, no. 1, pp. 1–2, 2015, doi: 10.1111/ext.12126.

[133] D. Lecompte *et al.*, “Quality assessment of speckle patterns for digital image correlation,” *Opt. Lasers Eng.*, vol. 44, no. 11, pp. 1132–1145, 2006, doi: 10.1016/j.optlaseng.2005.10.004.

[134] D. G. Hardy, “High temperature expansion and rupture behaviour of zircaloy tubing,” in *Topical meeting on water reactor safety*, 1973, p. pp 254-273, Accessed: Aug. 16, 2017. [Online]. Available: https://inis.iaea.org/search/search.aspx?orig_q=RN:41041036.

[135] K. Barrett, S. Bragg-Sitton, and D. Galicki, “Advanced LWR Nuclear Fuel Cladding System Development Trade-off Study,” *Idaho 83415 INL/EXT-12-27090*, no. September, pp. 1–34, 2012, doi: 10.2172/1057698.

[136] IAEA, “Review of Fuel Failures in Water Cooled Reactors,” *IAEA Nucl. Energy Ser.*, no. NF-T-2.1, pp. 1–171, 2010.

[137] G. Lampeas, V. Pasialis, X. Lin, and E. A. Patterson, “Simulation Modelling Practice and Theory On the validation of solid mechanics models using optical measurements and data decomposition,” *Simul. Model. Pract. Theory*, vol. 52, pp. 92–107, 2015, doi: 10.1016/j.simpat.2014.12.006.

[138] C. J. Carmody, G. Burriesci, I. C. Howard, and E. A. Patterson, “An approach to the simulation of fluid-structure interaction in the aortic valve,” *J. Biomech.*, vol. 39, no. 1, pp. 158–169, 2006, doi: 10.1016/j.jbiomech.2004.10.038.

[139] L. Felipe-Sesé, P. Siegmann, F. A. Díaz, and E. A. Patterson, “Integrating fringe projection and digital image correlation for high-quality measurements of shape changes,” *Opt. Eng.*, vol. 53, no. 4, p. 044106, 2014, doi: 10.1117/1.oe.53.4.044106.

[140] L. Guo, S. Yang, and H. Jiao, “Behavior of thin-walled circular hollow section tubes subjected to bending,” *Thin-Walled Struct.*, vol. 73, pp. 281–289, Dec. 2013, doi: 10.1016/J.TWS.2013.08.014.

[141] D. D. Scărlătescu, A. Modrea, and M. D. Stanciu, “Three-point Bend Test to Determine the Mechanical Behavior of the Tubes Used in Water Supply Networks,” *Procedia Manuf.*, vol. 32, pp. 179–186, 2019, doi: 10.1016/j.promfg.2019.02.200.

[142] ASTM, “Standard Test Methods for Bend Testing of Material for Ductility 1,” 1998. doi: 10.1520/E0290-14.

[143] L. Xu and M. Ma, “Study of the characteristics of train-induced dynamic SIFs of tunnel lining cracks based on the modal superposition approach,” *Eng. Fract. Mech.*, vol. 233, no. April, p. 107069, 2020, doi: 10.1016/j.engfracmech.2020.107069.

[144] S. Keller and B. Klusemann, “Application of stress intensity factor superposition in residual

stress fields considering crack closure," *Eng. Fract. Mech.*, vol. 243, no. September 2020, p. 107415, 2021, doi: 10.1016/j.engfracmech.2020.107415.

[145] C. Sebastian and E. A. Patterson, "Calibration of a digital image correlation system," *Exp. Tech.*, vol. 39, no. 1, pp. 21–29, 2015, doi: 10.1111/ext.12005.

[146] P. Lava, S. Cooreman, S. Coppieters, M. De Strycker, and D. Debruyne, "Assessment of measuring errors in DIC using deformation fields generated by plastic FEA," *Opt. Lasers Eng.*, vol. 47, no. 7, pp. 747–753, 2009, doi: 10.1016/j.optlaseng.2009.03.007.

[147] Christian WJR and Patterson EA, "Euclid." p. Ver 1.01, 2018, [Online]. Available: http://www.experimentalstress.com/software.htm.

[148] G. Lampeas, V. Pasialis, X. Lin, and E. A. Patterson, "On the validation of solid mechanics models using optical measurements and data decomposition," *Simulation Modelling Practice and Theory*, vol. 52. pp. 92–107, 2015, doi: 10.1016/j.simpat.2014.12.006.

[149] W. S. Lee, C. F. Lin, T. H. Chen, and W. Z. Luo, "High temperature deformation and fracture behaviour of 316L stainless steel under high strain rate loading," *J. Nucl. Mater.*, vol. 420, no. 1–3, pp. 226–234, 2012, doi: 10.1016/j.jnucmat.2011.10.005.

[150] B. Pan, D. Wu, and Y. Xia, "High-temperature deformation field measurement by combining transient aerodynamic heating simulation system and reliability-guided digital image correlation," *Opt. Lasers Eng.*, vol. 48, no. 9, pp. 841–848, 2010, doi: 10.1016/j.optlaseng.2010.04.007.

[151] S. N. Monteiroa, Frederico Muylaert Margemb, V. S. Candidoa, and A. B.-H. da S. Figueiredoa, "High Temperature Plastic Instability and Dynamic Strain Aging in the Tensile Behavior of Stainless Steel," *Mater. Res.*, vol. 20, no. 2, pp. 506–511, 2017, doi: DOI: http://dx.doi.org/10.1590/1980-5373-MR-2016-0854.

[152] G. Auletta and S.-Y. Wang, "Superposition Principle," in *Quantum Mechanics for Thinkers*, 2020, pp. 31–52.

Appendix A

MATLAB SCRIPT NOT INCLUDED